High Transverse Momentum Dijet Cross Section Measurements in Photoproduction at HERA

Dissertation

zur Erlangung des Doktorgrades
des Fachbereichs Physik
der Universität Hamburg

vorgelegt von

Aziz Dossanov

aus Karaganda

Hamburg
2013

Gutachterin/Gutachter der Dissertation:	Dr. Günter Grindhammer Dr. habil. Thomas Schörner-Sadenius
Gutachterin/Gutachter der Disputation:	Dr. Günter Grindhammer Prof. Dr. Johannes Haller
Datum der Disputation:	29.04.2013
Vorsitzende/Vorsitzender des Prüfungsausschusses:	Dr. Georg Steinbrück
Vorsitzende/Vorsitzender des Promotionsausschusses:	Prof. Dr. Peter Hauschildt
Dekanin/Dekan der MIN Fakultät:	Prof. Dr. Heinrich Graener
Leiterin/Leiter des Department Physik:	Prof. Dr. Daniela Pfannkuche

Abstract

The measurement of high transverse momentum differential dijet cross sections in photoproduction at HERA in the γp center-of-mass energy $101 < \mathrm{W}_{\gamma p} < 302$ GeV is presented in this thesis. The data have been recorded with the H1 detector at the HERA collider in e^+p mode during the year 2006, collecting an integrated luminosity of 92.4 pb^{-1}. The results correspond to a kinematic range of photon virtualities $\mathrm{Q}^2 < 4.0$ GeV^2 and inelasticities $0.1 < \mathrm{y} < 0.9$. Jets are defined using the inclusive $k_\perp$ algorithm, and a minimum transverse momentum of the two leading jets, $\mathrm{P}_{\mathrm{T,1st,2nd}} > 15.0$ GeV and pseudorapidities in the range of $-0.5 < \eta_{\mathrm{1st,2nd}} < 2.5$ are required. In order to suppress background and be able to compare the cross sections with reliable and safe pQCD NLO predictions an invariant mass of the two leading jets $\mathrm{M}_{12} > 40.0$ GeV is required. Single differential dijet cross sections are measured, including cross sections in the direct and resolved photon enhanced regions. In order to study the contribution of partons interacting in the hard process, which are sensitive to the jet pseudorapidities, three different topologies of jets pseudorapidities are investigated. Single differential cross sections as a function of proton momentum fraction, taken by the interacting parton, x_P, the fraction of photon momentum, x_γ, the angle between the incoming and outgoing partons in the hard scatter, $|\cos\theta^*|$ are presented. Additionally, the cross sections as a function of the invariant mass of dijets, M_{12}, $\overline{\eta} = (\eta_{1st} + \eta_{2nd})/2$, $\overline{\mathrm{P}}_\mathrm{T} = (\mathrm{P}_{\mathrm{T,1st}} + \mathrm{P}_{\mathrm{T,2nd}})/2$ and $\mathrm{P}_{\mathrm{T,1st}}$ are also presented. The data are compared to predictions from the Pythia event generator, based on the LO matrix elements and parton showers, and to the NLO QCD calculations corrected for hadronization effects.

Kurzfassung

Die Messungen von Wirkungsquerschnitten mit zwei Jets mit hohen Transversalimpulsen in der Photoproduktion bei HERA in dem γp-Schwerpunktsystem von $101 < \mathrm{W}_{\gamma p} < 302$ GeV werden in dieser Dissertation präsentiert. Die Daten wurden mit dem H1 Detektor während der HERA II e^+p Datennahme im Jahre 2006 aufgezeichnet. Der untersuchte Datensatz entspricht einer integrierten Luminosität von 92.4 pb^{-1}. Der kinematische Bereich der Analyse ist definiert durch die Photonvirtualität $\mathrm{Q}^2 < 4.0$ GeV^2 und Inelastitztät $0.1 < \mathrm{y} < 0.9$. Die Jets werden mittels des inklusiven $k_\perp$ Algorithmus definiert und müssen folgende Bedinungen erfüllen: die minimalen Transversalimpulse der beiden führenden Jets, $\mathrm{P}_{\mathrm{T,1st,2nd}} > 15.0$ GeV und deren Pseudorapiditäten $-0.5 < \eta_{\mathrm{1st,2nd}} < 2.5$. Um den Untergrund zu unterdrücken und die Wirkungsquerschnitte mit zuverlässigen und sicheren NLO QCD Voraussagen vergleichen zu können, wurde für die invariante Masse von den zwei führenden Jets, $\mathrm{M}_{12} > 40.0$ GeV verlangt. Differenzielle Dijet-Wirkungsquerschnitte wurden gemessen, auch für die beiden Bereiche in deren entweder direkte oder aufgelöste Photon-Wechselwirkungen dominieren. Um die Beiträge der beteiligten Partonen am harten Prozess , die von der Jetpseudorapdität abhängig sind, untersuchen zu können, werden Wirkungskuerschnitte für drei verschiedene Topologien der Jetpseudorapiditäten gemessen. Einzeldifferenzielle Wirkungsquerschnitte als Funktion des Proton-Impulsanteils, des wechselwirkenden Partons, x_P, des Photon-Impulsanteils, x_γ, der Winkel zwischen den einlaufenden und auslaufenden Partonen in der harten Streuung, $|\cos\theta^*|$, der invarianten Masse der zwei Jets, M_{12}, $\overline{\eta} = (\eta_{1st} + \eta_{2nd})/2$, $\overline{\mathrm{P}}_\mathrm{T} = (\mathrm{P}_{\mathrm{T,1st}} + \mathrm{P}_{\mathrm{T,2nd}})/2$ und $\mathrm{P}_{\mathrm{T,1st}}$ werden präsentiert. Die Daten werden sowohl mit dem Pythia Ereignissgenerator, basierend auf den Matrixelementen der führenden Ordnung und Partonshowern, als auch mit Rechnungen in nächstführender Ordnung QCD, korrigiert für Hadronisierungseffekte, verglichen.

CONTENTS

LIST OF FIGURES

CHAPTER 1

INTRODUCTION

The widely accepted theory which describes the interaction of elementary particles with each other by means of fundamental forces, electromagnetic, weak and strong, is the Standard Model (SM) theory. Experiments over many years have shown that protons and neutrons, which are building up the nuclei of atoms, are not elementary particles, but consist of quarks and gluons. The force that holds quarks together is the strong interaction, which is described within the quantum field theory, Quantum Chromodynamics (QCD).

The HERA accelerator was the first and the only lepton-hadron collider, which allowed a detailed study on the structure of the proton at high energies. The energies of the accelerated proton and electron beams were 920 GeV and 27.6 GeV, respectively. Due to the photon, radiated from the incoming electron, it is also possible to investigate the photon structure and its interaction processes. A QCD process, where a quasi-real photon ($Q^2 \sim 0$ GeV), radiated by an incoming electron, interacts with a proton, producing a hard scattering in the initial state and high transverse momentum hadronic jets in the final state, can be referred to as hard photoproduction. In this regime a photon can undergo direct scattering, similar to Deep-Inelastic Scattering (DIS), or it can fluctuate into a hadronic state, where a parton from the photon interacts with a parton in the proton. In the latter case one speaks of a resolved photon interaction, and the photon can be imagined as a hadronic object, characterized by a Parton Density Function (PDF), which can also be investigated along with the proton PDF.

This analysis presents a study of photoproduction interactions with two jets with high transverse energies in the final state. The analyzed sample used in this work was recorded during the 2006 e^+p period and corresponds to an integrated luminosity of 92.4 pb^{-1}. Single differential cross sections have been measured and are compared to QCD predictions in Leading Order (LO) and Next-to-Leading Order (NLO), in order to test the theory for photoproduction processes.

Chapter 2 highlights the theoretical understanding of ep and γp interactions. Additionally, a jet finding algorithm is presented in the last section of this chapter. In chapter 3 the H1 detector is discussed, with the emphasis on the detector compo-

nents which are of importance for this measurement. The 4th chapter provides descriptions of the basic features of MC event generators and their QCD based models used in the analysis. Chapter 5 describes the requirements on the data as well as the method to check the efficiencies of the subtriggers used. Chapter 6 reveals the steps prior to the determination of the cross sections. The purities and stabilities of the different measurements are obtained, and the detector and hadronization correction factors are determined. In chapter 7, the final results are discussed and presented in form of single differential cross sections. Chapter 8 gives a short summary of the analysis.

CHAPTER 2

THEORETICAL OVERVIEW

2.1 The Standard Model

The experimentally well-tested theory of particle physics which is based on a small number of fundamental constituents of nature and their interactions with each other is referred to as the Standard Model (SM) [Gla61, Wei67, Sal68]. It describes the forces (strong, electromagnetic and weak[1]), which govern the interaction of these fundamental particles. The fundamental particles can be classified into three basic types: *quarks*, *leptons* and the *gauge bosons*. Quarks and leptons represent a class of particles called *fermions* (particles with spin-$\frac{1}{2}$) and are grouped into three generations with identical quantum numbers but different masses. According to the SM, quarks have color and electroweak charges, leptons have only electroweak charge. Each fermion has a corresponding antiparticle [Fey88], this notion was first based on theoretical rather than experimental evidence. In 1929, Paul Dirac set out to find a wave equation that would describe the electron. He started from the generic form describing evolution of wave function:

$$i\frac{\partial}{\partial \mathrm{t}}\Psi = \hat{\mathrm{H}}\Psi. \tag{2.1}$$

Finding solution for particles at rest, Dirac finds two positive energy solutions that correspond to two spin states of spin-$\frac{1}{2}$ electrons and two symmetrical negative-energy solutions, which could be interpreted as positive-energy antiparticles.

It was experimentally proved that different types of quarks exist and they labeled as up (u), down (d), charm (c), strange (s), top (t) and bottom (b). The quarks with spin aligned opposite to the direction of motion are in left handed doublets: $\binom{u}{d}_{\mathrm{L}}$, $\binom{c}{s}_{\mathrm{L}}$, $\binom{t}{b}_{\mathrm{L}}$, and the ones with spin aligned along the direction of motion are right handed singlets: u_{R}, d_{R}, c_{R}, s_{R}, t_{R}, b_{R}. Quarks have color, charge and weak isospin, they interact with matter strongly, electromagnetically and weakly. Quarks have never been observed as free particles and exist only in bound states giving

[1] Gravitational force plays a negligible role in atomic and subatomic processes because of their weakness compared to SM scales.

	Quarks			Leptons		
Generation	**Flavor**	**Q**	**M(GeV)**	**Flavor**	**Q**	**M(GeV)**
1st	u (up)	$\frac{2}{3}$	$2.55^{+0.75}_{-1.05} \times 10^{-3}$	e (electron)	-1	5.1×10^{-4}
	d (down)	$-\frac{1}{3}$	$5.04^{+0.96}_{-1.54} \times 10^{-3}$	ν_e ($e-$neutrino)	0	$< 1 \times 10^{-8}$
2nd	c (charm)	$\frac{2}{3}$	$1.27^{+0.07}_{-0.11} \times 10^{-3}$	μ (muon)	-1	0.105
	s (strange)	$-\frac{1}{3}$	$104^{+26}_{-34} \times 10^{-3}$	ν_μ ($\mu-$neutrino)	0	$< 2 \times 10^{-4}$
3rd	t (top)	$\frac{2}{3}$	171.2 ± 2.1	τ (tau)	-1	1.776
	b (bottom)	$-\frac{1}{3}$	$4.20^{+0.17}_{-0.07}$	ν_τ ($\tau-$neutrino)	0	$< 2 \times 10^{-2}$

Table 2.1: The properties of the fundamental fermions (quarks and leptons, spin $= \frac{1}{2}$) of the SM [Group08].

rise to the *color confinement* phenomenon. In these bound states quarks clump together into groups called *hadrons*. Hadrons made out of three quarks (qqq) are called *baryons* and combinations consisting of quark-antiquark pairs ($q\bar{q}$) are called *mesons*.

The electron (e), the muon (μ), and the tau (τ) belong to the leptons. They all have the same electric charge $-e$, but differ in their masses. Each of them is associated with a neutral particle, the *neutrino*: ν_e, ν_μ, ν_τ. In the SM the neutrinos have zero mass, however various recent measurements indicate that their mass is not zero but probably very small. Neutrinos, due to the absence of electric charge, interact with matter only via the weak interactions. Leptons are also grouped into left-handed doublets and right-handed singlets: $\binom{e}{\nu_e}_{\mathrm{L}}$, $\binom{\mu}{\nu_\mu}_{\mathrm{L}}$, $\binom{\tau}{\nu_\tau}_{\mathrm{L}}$ and e_{R}, μ_{R}, τ_{R}. There are no right-handed neutrinos in the SM and under weak interactions the right-handed and left-handed leptons transform differently which is known as parity violation. The electron is the only stable lepton and together with the u and d quarks it makes up almost all matter.

The properties of quarks and leptons are displayed in table 2.1. The antiparticles of the aforementioned fermions are not included in the table, they have the same mass values (M) but, except of neutrinos of different flavors, the opposite electric charge (Q).

The gauge bosons have spin 1 and are understood as the carriers of the force they are associated with (see table 2.2). The *gluon* (g) is the carrier of the strong force, acting between quarks. This includes binding quarks together inside more complex objects like protons and neutrons, and it is also responsible for keeping protons and neutrons together inside the atomic nuclei. Gluons couple to quarks and as they themselves carry color also to gluons. In contrast to gluons, photons do not carry electric charge. The *photon* (γ) mediates the electromagnetic force between electrically charged particles (quarks and the charged leptons). It also regulates the

Force	Force Carriers	Coupling	Relative Strength	Mass (GeV)	Spin
Strong	g (gluon)	quarks & gluons	1	0	1
Electromagnetic	γ (photon)	quarks, $W^{\pm}$ & charged leptons	1.4×10^{-2}	$< 3 \times 10^{-36}$	1
Weak	$W^{\pm}$, Z^0	quarks & leptons	2.2×10^{-6}	80, 91	1
Gravitational	graviton	massive particles	10^{-38}	0	2

Table 2.2: The fundamental forces and force carriers. The forth fundamental force Gravity is shown separately as it is not yet within the SM [Group08].

orbit of electrons in atoms and governs chemical processes. $W^{\pm}$ and Z^0 bosons are the carriers of the weak force and are responsible for radioactive decays. The weak force couples to quarks and also to leptons. Within the SM the electromagnetic and weak theories are unified to the Electroweak theory [Gla61, Wei67, Sal68].

The SM explains the interactions among quarks, leptons and bosons but does not include the explanation of the genesis of mass of the fundamental particles. In 1964 a Scottish physicist Peter W. Higgs [Hig64], and also independently from him other scientists, proposed a mechanism how the fundamental particles could acquire their mass. According to this theory all space is permeated by a scalar field, called *Higgs* field, which has some similarities to the electromagnetic field. Elementary particles traveling through this field couple to it to get their masses. As every field the Higgs field should have an associated particle called the Higgs boson. It is massive scalar particle with no intrinsic spin or electrical charge. Unlike all the other bosons the Higgs particle does not mediate a force.

2.2 Electron-Proton Scattering

In 1911, the Rutherford's experiment observing the scattering of α particles from gold nuclei was a turning point for nuclear physics and became the first milestone in understanding the subatomic structure of matter. An analogous technique, the scattering of leptons on a hadronic target, is by now considered to be a well-proven method to study the internal structure of hadrons. For instance, as hadronic target one takes a proton or a heavier nucleus and an electron[2] or even neutrino as the probing candidate.

If only the electron and the target particle (e.g. proton) appear in the final state, i.e. $ep \rightarrow ep$ than the process is called *elastic*. In case of an *inelastic* interaction more hadronic particles are produced in the final state. If the momentum transfer to the proton or nucleus is much larger than the proton mass, m_p, the process is called Deep-Inelastic Scattering (DIS). In this case the initial state proton loses its identity completely and the outcome is a high multiplicity Hadronic Final State (HFS) (see

[2]Throughout this thesis, the term *electron* refers to either electron, e^- or positron, e^+. All the following statements are valid for both particles, if not specified extra.

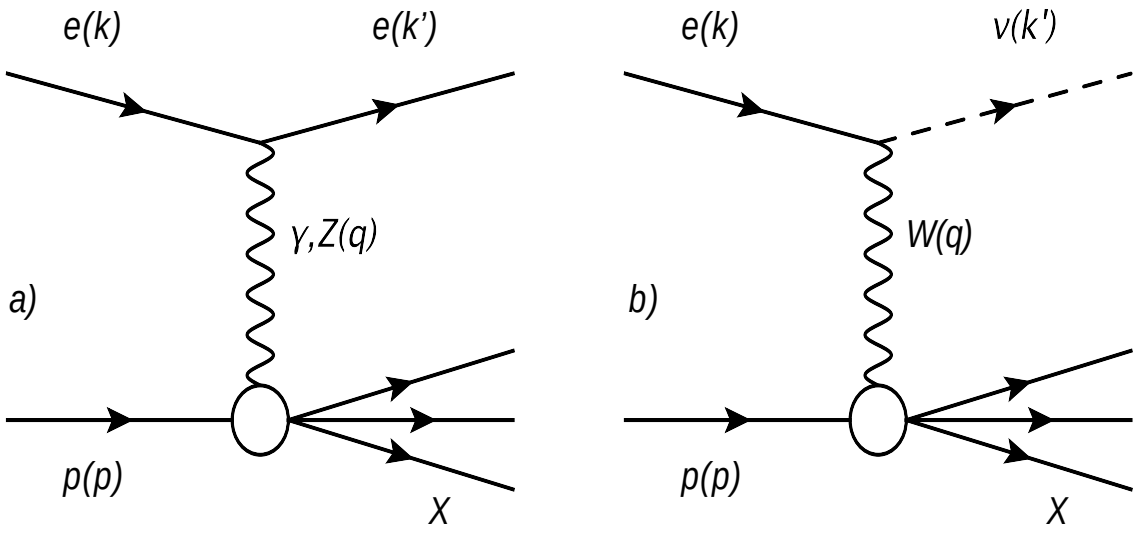

Figure 2.1: The kinematic variables of ep scattering at HERA for a) NC and b) CC interaction.

section 5.3). The study of such processes makes it possible to reveal the internal structure of the hadron in the initial state, which in the case of HERA physics is the proton.

2.2.1 Kinematics of ep Scattering

The schematical interpretation of boson exchange in lowest order perturbation theory is shown in figure 2.1 for the processes $ep \rightarrow eX$ and $ep \rightarrow \nu X$. An incoming electron with 4-momentum k scatters from a proton with 4-momentum p. The interaction is mediated via the exchange of either a virtual photon γ or Z^0 boson, figure 2.1a, or a $W^{\pm}$ boson, figure 2.1b. This boson carries a momentum transfer of the incident electron q. The processes mediated by $W^{\pm}$ boson are referred to as Charged Current (CC) interactions, and the exchange of Z^0 or γ are associated to Neutral Current (NC) processes. The 4-momentum of the outgoing electron, scattered at a polar angle θ_e, is k'. With X one denotes the complete system of reaction products – a high multiplicity HFS.

Several invariant variables can be used to describe the reaction. The center-of-mass energy is given by equation 2.2.

$$\sqrt{s} = \sqrt{(k+p)^2}. \tag{2.2}$$

At HERA, the masses of e and p can be neglected, then the center-of-mass energy can be defined as $\sqrt{s} \approx 4\mathrm{E}_p\mathrm{E}_e$ yielding $\sqrt{s} \approx 319$ GeV, where E_p (920 GeV) and E_e (27.6 GeV) are the respective fixed energies of the incident proton and electron

beams. The negative squared 4-momentum transfer of the electron to the proton, denoted Q^2, is always positive and is given by equation 2.3. It also specifies the virtuality of the exchanged boson. At low Q^2, due to the high masses of the Z^0 and $W^{\pm}$ bosons, the interaction rate of these processes with respect to γ exchange is greatly suppressed.

$$Q^2 = -q^2 = -(k - k')^2. \tag{2.3}$$

At the fixed center-of-mass energy $\sqrt{s}$ it is sufficient to have only two variables to describe the kinematics of the reaction $ep \to eX$. One possible choice is Q^2 together with the Bjorken scaling variable x_{Bj}. The Bjorken scaling variable is given by equation 2.4

$$x_{Bj} = \frac{Q^2}{2p \cdot q} \tag{2.4}$$

In the infinite momentum frame of the proton or in other words, when the struck parton[3], which participates in the hard[4] scattering, flies collinear to the direction of the proton trajectory, x_{Bj} represents the fraction of the proton's 4-momentum carried by the interacting parton.

Another possible choice is Q^2 and the inelasticity y, where y is defined as:

$$y = \frac{P \cdot q}{p \cdot k}. \tag{2.5}$$

In the proton rest frame the variable y may be interpreted as the fraction of energy transfered from the electron to the proton; $y = \frac{E_\gamma}{E_e}$. Both x_{Bj} and y take values between zero and unity.

The invariant mass of the γp system, W, is defined in equation 2.6

$$W^2 = (q + p)^2. \tag{2.6}$$

If one neglects the masses of the particles, the aforementioned quantities may be related to each other by equations 2.7 and 2.8

$$Q^2 = s \cdot x \cdot y, \tag{2.7}$$

$$W^2 = Q^2 \cdot (\frac{1 - x}{x}). \tag{2.8}$$

For negligibly small values of $Q^2 \sim 0$ the exchanged photon is "on-mass shell" and the ep scattering can be simplified by considering the electron as a radiator of quasi-real photons and the subsequent scattering of the photon from the proton. This

[3]According to the parton model proposed by Richard Feynman [Fey69] in 1969, a hadron is composed of a number of point-like constituents called "partons". The partons carry only a fraction $\xi_{p,i}$ of the longitudinal 4-momentum of the proton, such that $\sum_i \xi_{p,i} = 1$ [Fey72]. Further on, the word parton will be collectively referred to quarks, anti-quarks and gluons, if not stated otherwise.

[4]See section 2.3.1 for the explanation of the hard scattering process.

kinematic domain is termed as a photoproduction process or $\gamma^* p$ scattering (see section 2.3).

In interactions of elementary particles, events for which $Q^2 > 1$ GeV^2 are classified as DIS and those for which $Q^2 < 1$ GeV^2 are classified as photoproduction, i.e. the production of hadrons by the inelastic scattering of real photons on a nucleon target.

Reconstruction of Kinematic Variables

Reconstruction of kinematic variables can be managed by means of scattered lepton and HFS information of the event. Particles are measured using the energy deposits in the calorimeters together with low momentum tracks identified in the tracking detectors (see chapter 3). There are different methods exist in order to derive the event kinematics. The choice of the reconstruction method affects the acceptance scale and radiative corrections as well as the precision of the reconstruction of the kinematic variables. As this analysis is basically deals with the photoproduction regime, there is no information on the scattered lepton available. That means that the reconstruction method should not be based on the scattered electron quantities and is pure hadronic, that also defines the name for the method used in the analysis – hadron-method, also known as Jacquet-Blondel method [BJ79]. More information on the reconstruction methods, related to the scattered electron, is available elsewhere, i.e. [Kog10, Shu11, Rau02].

Hadron-Method This method uses the four-momentum conservation principle and is based on the kinematic quantities Σ and transverse momentum $P_{T,h}$ as well as an inclusive hadronic angle γ_h, the latter can be interpreted, within a Quark Parton Model (QPM) (2.2.2), as a scattering angle of parton. They are defined as:

$$\Sigma = \sum_i \left(E_i - P_{z,i}\right), \quad P_{T,h} = \sqrt{\sum_i \left(P_{x,i}\right)^2 + \sum_i \left(P_{y,i}\right)^2}, \quad \tan\frac{\gamma_h}{2} = \frac{\Sigma}{P_{T,h}}, \tag{2.9}$$

where E_i stands for the energy of the i-th particle. $P_{z,i}$ is the longitudinal and $P_{x,i}$ and $P_{y,i}$ are the transversal components of the particle's impulse in the H1-laboratory system (see section 3.2). The summation is run over all the HFS particles except of the scattered electron. These quantities define the kinematic variables:

$$y_h = \frac{\Sigma}{2 \cdot E_e}, \tag{2.10}$$

$$Q_h^2 = \frac{P_{T,h}^2}{1 - y_h}, \tag{2.11}$$

$$x_h = \frac{Q_h^2}{s \cdot y_h}. \tag{2.12}$$

2.2.2 The ep Cross Section

The double differential cross section in x and Q^2 for NC $e^{\pm}p$ scattering is given by equation 2.13 [DCS04]

$$\frac{d^2\sigma(e^{\pm}p)}{dxdQ^2} = \frac{2\pi\alpha^2}{xQ^4}\left[Y_+F_2(x,Q^2) \mp Y_-xF_3(x,Q^2) - y^2F_L(x,Q^2)\right], \tag{2.13}$$

where α is the fine structure constant and $Y_\pm$ is a *helicity*[5] factor:

$$Y_\pm = 1 \pm (1-y)^2. \tag{2.14}$$

The dimensionless structure functions F_L, F_3 and F_2, dependent on x and Q^2, parametrize the structure of the proton as it is probed by the photon. The longitudinal structure function F_L is defined as $F_L = F_2 - 2xF_1$ and quantifies the contribution to the cross section from the exchange of longitudinally polarized virtual photons. It is kinematically suppressed compared to F_2 and becomes significant only at high y. The F_3 structure function describes parity violation and includes effects from Z^0 exchange and γZ interference which is in case of $Q^2 \ll M_Z^2$ of negligible importance. Now, for the regime when Q^2 is relatively low the equation 2.13 can be simplified into equation 2.15

$$\frac{d^2\sigma(e^{\pm}p)}{dxdQ^2} = \frac{2\pi\alpha^2}{xQ^4}\left[Y_+F_2(x,Q^2) - y^2F_L(x,Q^2)\right]. \tag{2.15}$$

In this kinematic region and for y not close to 1, F_2 provides the dominant contribution to the cross section by means of the transversely polarized virtual photons. At Leading Order (LO) F_2 can be viewed as a linear combination of the proton's quark and anti-quark momentum distributions 2.16:

$$F_2(x,Q^2) = \sum_i e_i^2\left[xq_i(x,Q^2) + x\bar{q}_i(x,Q^2)\right], \tag{2.16}$$

where the sum runs over the quark flavors, and e_i is the electrical charge of quark flavor i and $q_i(x,Q^2)$ are the so-called Parton Density Functions (PDFs), which have the meaning of a probability density of finding quark or antiquark i with a proton's momentum fraction x at a given scale of Q^2.

In the naïve parton model of the proton (Quark Parton Model (QPM)), where hadrons are described such as if they were made only out of massless point-like partons, F_2 has no dependence on Q^2 but only on x and one speaks of *scaling* of F_2 [Bjo69][6]. Scaling was predicted by J. Bjorken and was first seen by the SLAC-MIT experiment [B^+69a, B^+69b]. Figure 2.2 shows observed scaling behavior of W_2 ($\sim F_2$) for the experiment where high energetic electrons scatter off a nuclear target.

The theory of strong interactions – perturbative QCD is a non-Abelian gauge theory of quarks and gluons, invariant under $SU(3)$ color transformations. Within this theory emission of gluons from quarks and also from gluons is included in calculations of cross sections, in particular into the PDFs. The main feature of the parton

[5] Helicity is the projection of the spin onto the direction of momentum of the particle.

[6] In 1969 Bjorken proposed that in the "deep inelastic region" $Q^2 \to \infty$, $\nu = \frac{Q^2}{2M_p x} \to \infty$, the structure function scale only as a function of x, $\nu W_2(Q^2,\nu) \to F_2(x)$.

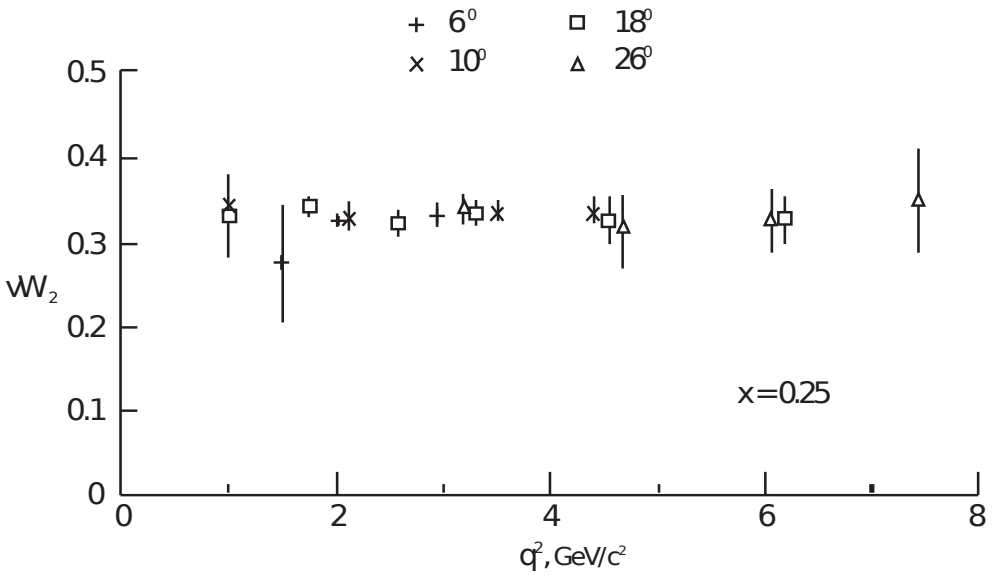

Figure 2.2: The scaling phenomenon. At a fixed Bjorken value of x = 0.25 F_2 does not depend on Q^2 [FK72].

model remains in QCD, but the proton is seen as a source of gluons emitted from constituent quarks. The radiation of gluons from quarks reduce the original momentum fraction of the scattering quark. Additionally gluon splitting may lead to $q\bar{q}$ and gg pairs. At low x values the quark densities in the proton are expected to increase with Q^2 and vice versa they decrease with Q^2 at high x. This behavior is known as Bjorken scaling violation and can be seen in figure 2.3. Here, the structure function F_2 was measured at HERA with high precision. Since the *factorization theorem* allows to link the structure function F_2 and the parton density functions, than for a given choice of factorization scheme and scale, the proton PDFs are considered to be universal. Hence, the data from figure 2.3 reflect a very important measurement for other experiments.

Although, QCD does not predict the x-dependence of the PDFs, their Q^2 evolution can be calculated by means of the DGLAP [Dok77, GL72, AP77, Dok72] evolution equations 2.17 and 2.18. These are integro-differential equations which, using the PDFs of quarks and gluons at some given starting scale, predict the PDFs, and consequently the structure functions, at a new scale:

$$\frac{\partial q_i(\mathrm{x},\mathrm{Q}^2)}{\partial \log \mathrm{Q}^2} = \frac{\alpha_s}{2\pi}\int_{\mathrm{x}}^{1}\frac{d\mathrm{y}}{\mathrm{y}}\left[q_i(\mathrm{y},\mathrm{Q}^2)\mathrm{P}_{qq}\left(\frac{\mathrm{x}}{\mathrm{y}}\right)+g(\mathrm{y},\mathrm{Q}^2)\mathrm{P}_{qg}\left(\frac{\mathrm{x}}{\mathrm{y}}\right)\right], \tag{2.17}$$

$$\frac{\partial g(\mathrm{x},\mathrm{Q}^2)}{\partial \log \mathrm{Q}^2} = \frac{\alpha_s}{2\pi}\int_{\mathrm{x}}^{1}\frac{d\mathrm{y}}{\mathrm{y}}\left[q_i(\mathrm{y},\mathrm{Q}^2)\mathrm{P}_{gq}\left(\frac{\mathrm{x}}{\mathrm{y}}\right)+g(\mathrm{y},\mathrm{Q}^2)\mathrm{P}_{gg}\left(\frac{\mathrm{x}}{\mathrm{y}}\right)\right], \tag{2.18}$$

where $q_i(\mathrm{y},\mathrm{Q}^2)$ and $g(\mathrm{y},\mathrm{Q}^2)$ denote the quark and gluon density function, respectively. The functions P_{qq}, P_{qg}, P_{gq} and P_{gg} are the Altarelli-Parisi *splitting functions*

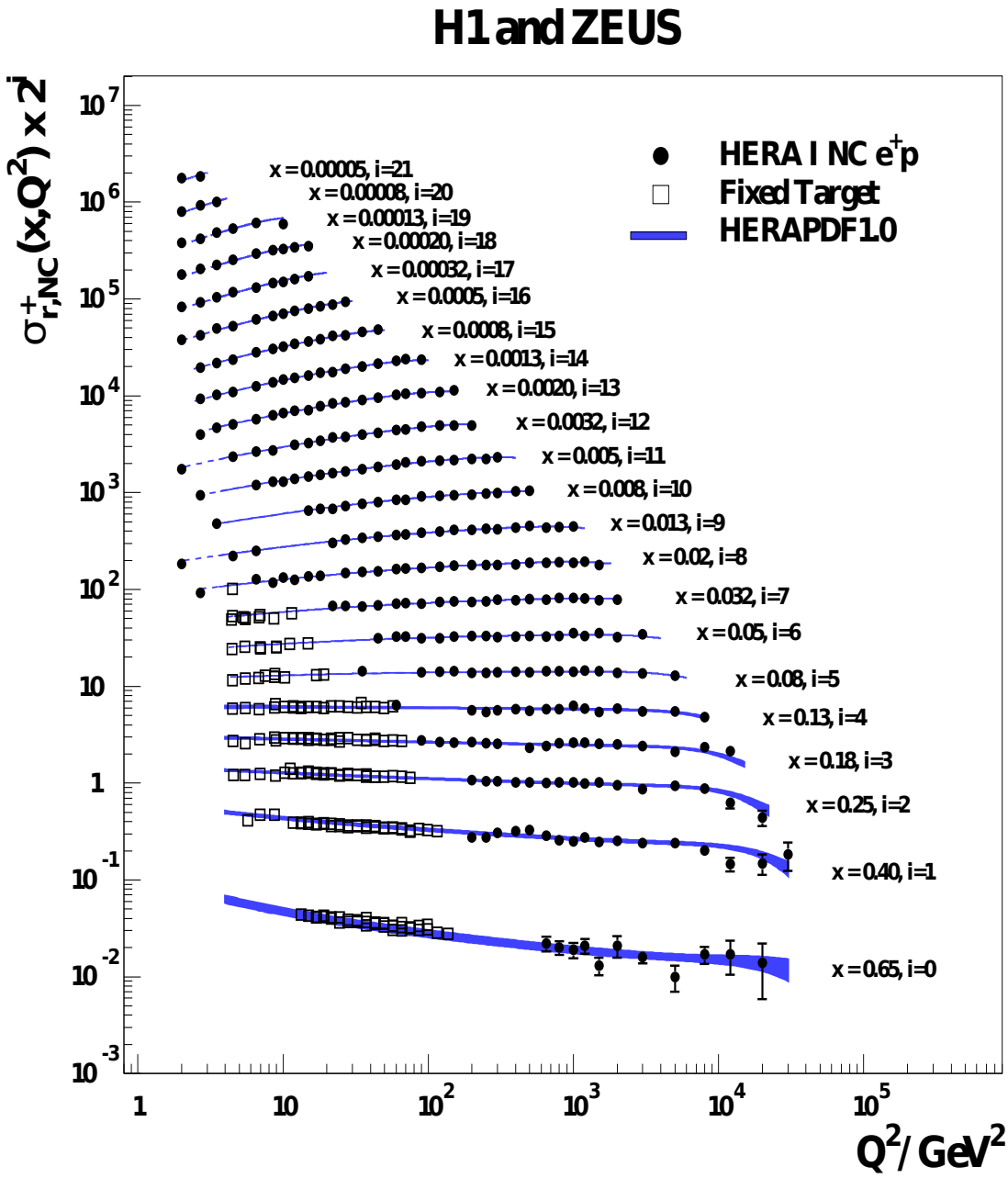

Figure 2.3: Measurement of H1 and ZEUS combined structure function data from e^+p NC DIS scattering as function of Q^2 for various values of x. The *scaling violation* is clearly observed. The blue bands correspond to NLO DGLAP calculations using the HERAPDF1.0 [HZ10]. The open boxes are from fixed target experiment (for more details refer to [Kog10], page 18).

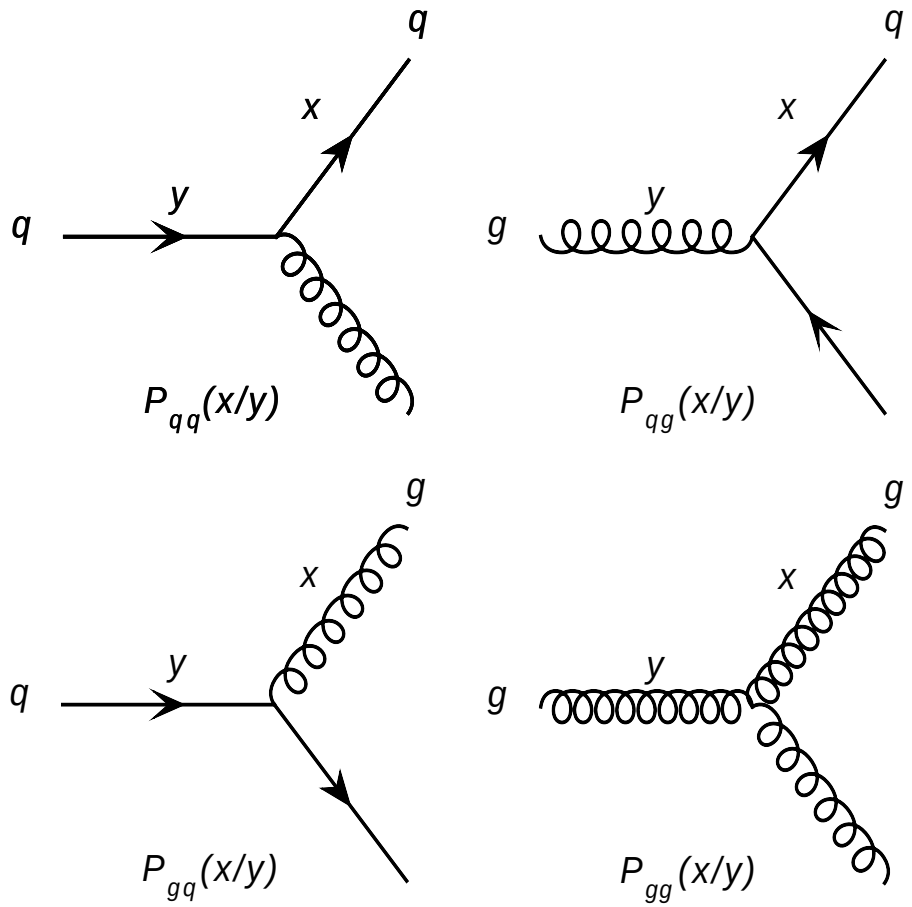

Figure 2.4: The Feynman diagrams for the Altarelli-Parisi splitting functions used in the DGLAP evolution equations.

with the momentum fraction $\left(\frac{x}{y}\right)$. The function $P_{lm}(\frac{x}{y})$ expresses the probability that parton m, produced from the splitting of parton l with momentum fraction y, carries a fraction x of the l's momentum. Figure 2.4 depicts the LO Feynman diagrams of the processes represented by each of the four splitting functions.

2.3 γp Physics

The negative squared momentum transfer, Q^2 can be interpreted as the size scale for the interaction. The region $Q^2 \gtrsim 1$ GeV^2, where the virtual photon probes the structure of the proton, is the one for DIS. In the region where $Q^2 \sim 0$ GeV^2 the photon behaves as if it is quasi-real, although it will not have enough resolving power to probe the proton's structure. This domain is called *photoproduction* or γp scattering. It provides the dominant contribution to the HERA event rate because of the photon propagator in the inclusive NC DIS cross section, which gives rise to a factor $1/Q^4$. Although the regions of almost-vanishing and of high Q^2 provide scientists with different physical phenomena, it is of great importance to find out how γp scattering is related to the one of ep.

2.3.1 Photoproduction

As the study of this work involves only the photoproduction domain, the further discussion will be concentrated purely on this topic, if not otherwise specified. The γp scattering occurs at the exchange of a quasi-real photon with $Q^2 < 1$ GeV^2. In the kinematic limit as $Q^2 \to 0$ the photons are massless and transversely polarized bosons[7] which are struck collinearly to the beam line with electron's longitudinal momentum fraction y, so that we effectively have a γp collisions. Here, y can be interpreted in a same manner as inelasticity in case of DIS processes. The variable y is directly related to the center of mass energy $W_{\gamma p}$ of the photon proton system:

$$W^2_{\gamma p} = (q + p)^2 = y \cdot s - Q^2 \approx y \cdot s, \tag{2.19}$$

where q and p are the photon's and proton's four-momenta, respectively. If the masses of proton and electron can be neglected, the approximation in equation 2.19 turns into an equality.

By means of the Equivalent Photon Approximation (EPA) [BGMS75] the relation between γp and ep cross sections can be factored into two parts in the form of equation 2.20.

$$\frac{d^2\sigma(ep)}{dy dQ^2} = f^e_\gamma(y, Q^2)\sigma^{\gamma p}(y, Q^2), \tag{2.20}$$

where $f^e_\gamma(y, Q^2)$ is the *photon flux* and can be interpreted as a probability to find a photon from the electron with an energy $E_\gamma = yE_e$. Using the Weizsäcker-Williams Approximation (WWA) [vW34, Wil35, FMNR93], the photon flux with energy fraction y and photon virtuality Q^2_{min} up to Q^2_{max} given by:

$$f^e_\gamma(y, Q^2) = \frac{\alpha}{2\pi}\left[\frac{1 + (1 - y)^2}{y} \ln\left(\frac{Q^2_{max}}{Q^2_{min}}\right) - 2m^2_e y\left(\frac{1}{Q^2_{min}} - \frac{1}{Q^2_{max}}\right)\right], \tag{2.21}$$

such that $f^e_\gamma(y, Q^2)dy$ defines the number of photons radiated in the fractional energy range y and y+dy with virtuality between Q^2_{min} and Q^2_{max}. In equation 2.21 α is the fine structure constant, $Q^2_{min} = \frac{m^2_e y}{1-y} \approx 10^{-7}$ GeV^2 is the smallest photon virtuality generated by electrons [Erd97] for a given inelasticity y, where m_e is the electron mass. This condition together with current conservation allows the factorization approach described in equation 2.20. The value of Q^2_{max} is determined from the experimental setup by:

$$Q^2_{max} = -\left(k - k'\right)^2 = 2E_e E'_e\left(1 + \cos\theta'_e\right), \tag{2.22}$$

where E_e is the energy of the incident electron, E'_e and θ'_e are the energy and polar angle of the scattered electron.

[7] $\sigma_L \to 0$ and $\sigma_T \to \sigma^{\gamma p}_{tot}$.

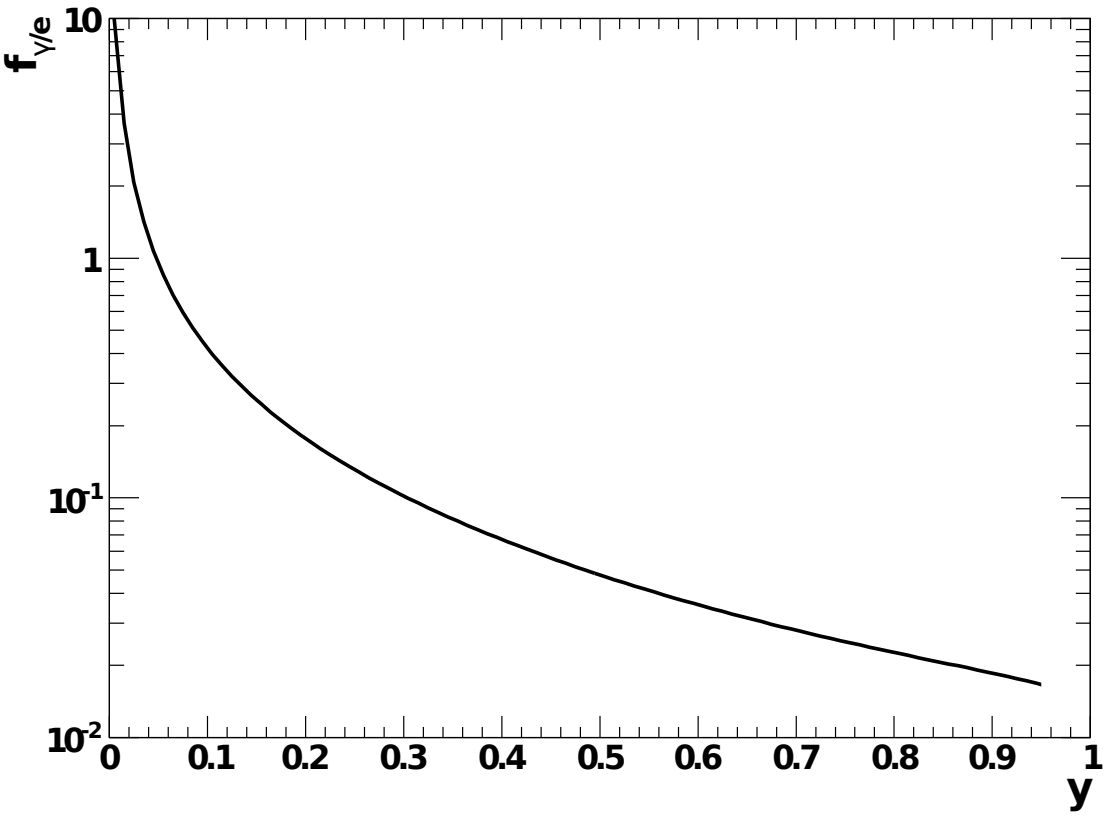

Figure 2.5: The energy spectrum of quasi-real photons, emitted by electrons, is shown as a function of the scaled photon energy y= $\frac{E_\gamma}{E_e}$ for a maximum virtuality $Q^2_{max} = 4.0$ GeV^2. Simulation is inspired from [Erd97].

Figure 2.5 shows the energy spectrum of quasi-real photons, emitted by electrons for $Q^2_{max} = 4.0$ GeV^2. In the region for energies $y > 0.2$ the number of photons decreases by a factor of 10, but rises significantly at small photon energies $y < 0.2$.

At HERA three types of photoproduction processes can be distinguished: elastic, diffractive processes and non-diffractive processes. They can be further divided into "soft" and "hard" processes depending on the transverse energy produced in the HFS. The soft processes can be photon dissociation, double dissociation or elastic vector meson production [H195a]. Hard scattering processes that produce particles with high transverse momentum and jets were observed in non-diffractive processes [H192], in resolved processes, where the quarks and gluons of the proton are used to probe the structure of the quasi-real photons and in direct processes, where the structure of the proton is probed. Figure 2.6 reflects the diagrams for these processes.

As was mentioned above the photoproduction processes prevail the NC DIS cross section with a $1/Q^4$ rise from the photon propagator. The total cross section will than be dominated by the exchange of very low virtuality photons. With the decreasing photon virtuality we can no longer consider Q^2 as a hard scale of the interaction and the perturbative methods still have to remain applicable. One requires some alternative hard scale, for instance the invariant mass of the γp system, $W^2 = (q + P)^2$, or, more useful, the observation of jets with a significant transverse

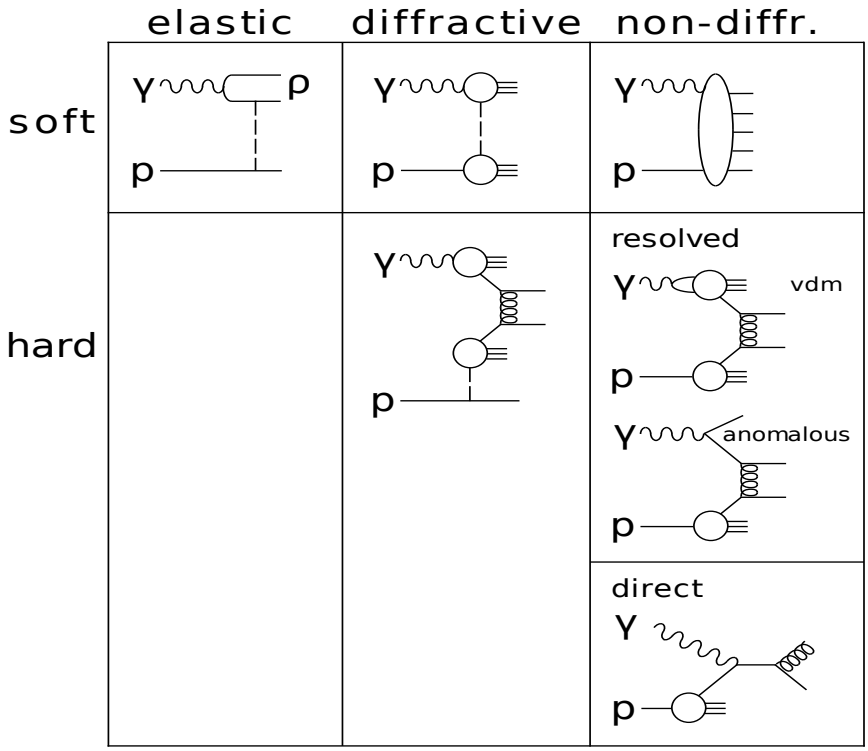

Figure 2.6: Different photoproduction processes studied at HERA. This figure is taken from [Erd97], p.38.

momentum E_T, or in case of massless scheme, jets P_T. At HERA due to the large center-of-mass energy $\sqrt{s_{\gamma p}}$ of the photon-proton system "hard" photoproduction processes are expected to be seen.

2.3.2 γp Interactions

By means of factorization of the $e^{\pm}p$ cross section (see equation 2.20) the interactions between photons and protons can be studied. At HERA the γp interactions can be probed at high energies, which allow reliable perturbative calculations in contrast to interactions with "soft" final state particles. However, those were the low energy fixed target experiments [BSYP78] with a relatively low P_T of final state particles where one saw similar interaction scenarios as it was observed at the collisions of two hadrons.

Figure 2.7 shows the states the photon can fluctuate into. It can participate in the scattering as a bare photon, which is also referred to as a *direct* photoproduction or as a resolved photon, which is referred to as a *resolved* photoproduction. It can happen that the interacting photon does not form a stable bound state but fluctuates into a $q\bar{q}$ pair. In this hadronic pair, one of the quarks instantly interacts in a hard scattering. This is known as an *anomalous* contribution to the resolved part. The label 'VDM' is synonymous with a resolved photon interaction, where the $q\bar{q}$ pair of the photon may form a bound state before scattering from a parton struck by the proton.

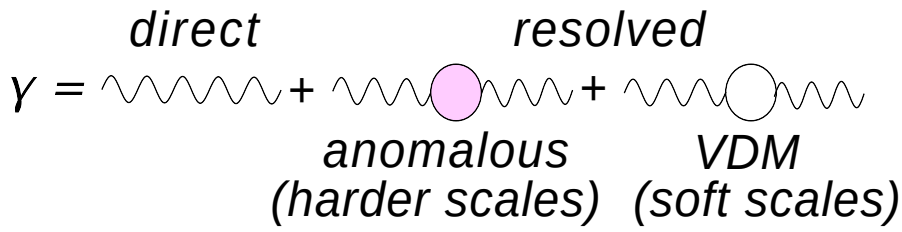

Figure 2.7: Shown are the states the photon can fluctuate into. Besides, when it is in a bare or direct state - the *direct* photoproduction process, it can fluctuate into $q\bar{q}$ pairs without forming a "hadronic" bound state - *anomalous*, or it forms a vector meson (VDM). The two latter states are related to the *resolved* photoproduction process.

Vector Meson Dominance Model (VDM)

The photon can be regarded, to a very good approximation, as a superposition of a "bare" photon and a "hadronic" photon. The physical photon fluctuates back and forth between the "bare" and "hadronic" states allowing these time dependent transitions to occur. Such transitions are called *vacuum polarization fluctuations* ([BSYP78], p.276). This notion is quantitatively described by the Vector Meson Dominance Model (VDM) [Sak60, GMZ61]. In this model, the hadronic photon is represented by a superposition of the three vector mesons $\rho(770)$, $\omega(782)$ and $\phi(1020)$ with the quantum numbers of the photon, spin 1, negative parity and negative charge conjugation ($\mathrm{J^{PC}} = 1^{--}$).

The typical interaction time, t_i is smaller than the typical fluctuation time, t_f between "bare" and "hadronic" photon states. This assumption allows the $q\bar{q}$ pair originating from the interacting photon to form a bound state. In the target rest-frame, t_f is approximately ($\hbar = 1$) [BSYP78]:

$$t_f \approx \frac{2\mathrm{E}_\gamma}{\mathrm{m}_V^2 - q^2}, \tag{2.23}$$

where m_V is the mass of the vector meson and E_γ and q^2 is the photon's energy and negative 4-momentum squared, respectively. The time t_i is defined by the time the photon needs to traverse the target, e.g. the diameter of the proton ($\mathrm{c} = 1$):

$$t_i \approx 2\mathrm{r}_p. \tag{2.24}$$

Hence, VDM plays a role in the interaction only if:

$$\mathrm{E}_\gamma \gg \left(\mathrm{m}_V^2 - q^2\right) \mathrm{r}_p \ . \tag{2.25}$$

The VDM is purely phenomenological, although it correctly describes the $\gamma - target$ collisions which mostly have the signatures of "soft" particle interactions.

2.3.3 Direct Photoproduction of Dijets

Interaction processes in which the quasi-real photon couples directly to a parton from the proton are generally termed as direct photoproduction processes. Figure 2.8 shows two important LO direct dijet photoproduction processes.

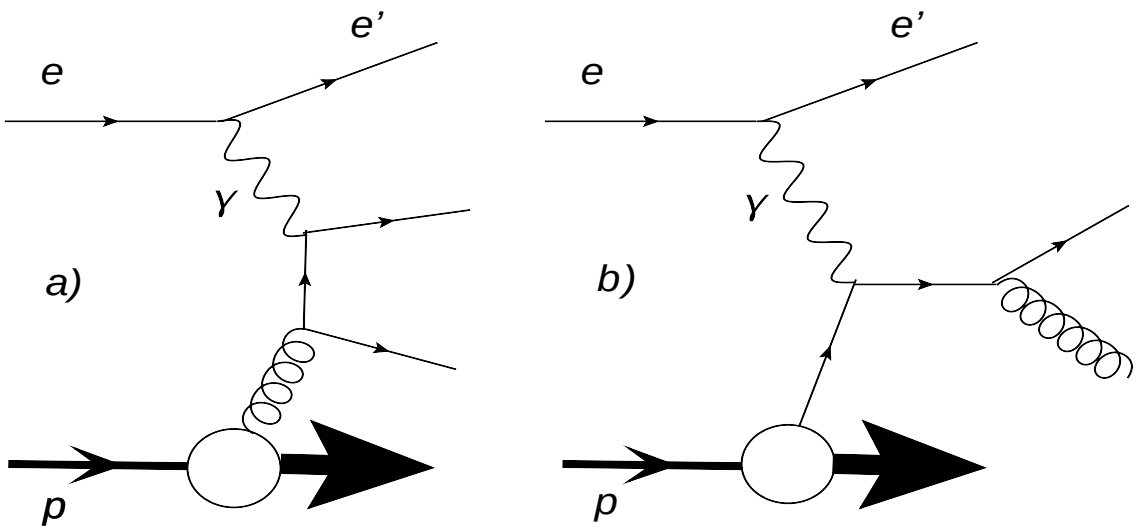

Figure 2.8: Two dominant LO direct processes for dijet production are: a) *Boson-Gluon Fusion (BGF)* and b) *QCD Compton (QCDC) scattering*.

The Boson-Gluon Fusion (BGF) process is sensitive to the gluon from the proton, producing light $q\bar{q}$ as well as heavy $c\bar{c}$ or $b\bar{b}$ pairs, which fragment into particles, which of the energies high enough to emerge as two jets. Generally, photoproduction processes are more sensitive to the gluon content of the proton than the ones from the DIS, although DIS at low Q^2 ($\lesssim 1000$ GeV^2) is dominated by BGF. Another LO contribution is the QCD Compton (QCDC) scattering process whereby the photon interacts directly with a quark from the proton, emitting a gluon and a quark in the final state.

For the photoproduction of jets Q^2 is not an appropriate hard scale for the perturbative calculations, however, like in hadron-hadron collisions the transverse energy of the partons (or jets[8]) provides a suitable hard scale. At lower P_T scales the BGF contributes more, whilst at higher P_T scales the QCDC is the dominant process. This is governed by the relative probabilities of interactions with gluons and quarks in the proton at low and high P_T scales. Lets introduce a quantity x_P, which defines the fraction of the protons momentum carried by the struck parton in the hard interaction in terms of the outgoing partonic transverse energies and pseudorapidities:

$$x_P = \sum_i \frac{E_{T,i} e^{+\eta_i}}{2E_P}, \tag{2.26}$$

[8]See section 2.5 for the jet definition.

where, for the case of dijet events, the sum runs over the two outgoing partons from the hard interaction. $E_{T,i}$ denotes the transverse energy (equivalent to the momentum, $P_{T,i}$, for massless partons) of the i^{th} outgoing parton with its pseudorapidity η_i.

In reality one has no information on the $E_{T,i}$ and η_i of the outgoing partons, but one can make use of the well established observation that reconstructed bundles of particles, i.e. jets, provide precise information about the underlying partons. Therefore one obtains a good correlation of x_P in equation 2.26 with the observable quantity x_P^{obs}:

$$x_P^{obs} = \frac{E_{T,1st} e^{+\eta_{1st}} + E_{T,2nd} e^{+\eta_{2nd}}}{2E_P}, \tag{2.27}$$

where the summation is done over the jet quantities. The quantity $E_{T,1st}$ corresponds to the energy of the jet with the highest transverse energy (also termed the leading jet, $E_{T,leading}$ or the jet with the maximum transverse energy, $E_{T,Max}$) and $E_{T,2nd}$ corresponds to the energy of the jet with the second highest transverse energy, sub-leading jet. The pseudorapidities η_{1st} and η_{2nd} of the jets refer to the leading and sub-leading jet, respectively.

For a given configurations of pseudorapidities using the equation 2.26 one can derive that at low scales of the transverse momentum the value of x_P would be relatively low which reflects a higher gluon density in the proton. At the higher scales of the transverse momentum one has to consider the interactions with high-x_P values. For the latter case it is more probable that the interaction happens with a valence quark, which tends to carry most of the protons momentum, thereby making the QCDC process dominant at high P_T scales.

2.3.4 Resolved Photoproduction

The processes where the photon acts as a source of partons which themselves participate in the hard scattering are called resolved photoproduction. These are the processes where photon under certain conditions is assumed to be able to fluctuate into a virtual cloud of partons or into a virtual meson state - $q\bar{q}$ or $l\bar{l}$ states, with the same quantum numbers as the photon, obeying the Heisenberg uncertainty relation.

Figure 2.9 shows examples of the LO resolved photoproduction processes for the production of dijets.

Analogy to Hadron-Hadron Interaction

It is worth to mention that one handles resolved photoproduction processes analogously to hadron-hadron interactions. Although, the QPM photon structure function F_2^γ has three features that are different from hadronic structure functions [Erd97]:

- The quark charges e_q contribute to the fourth power, compared with quadratic contributions in hadronic structure functions.

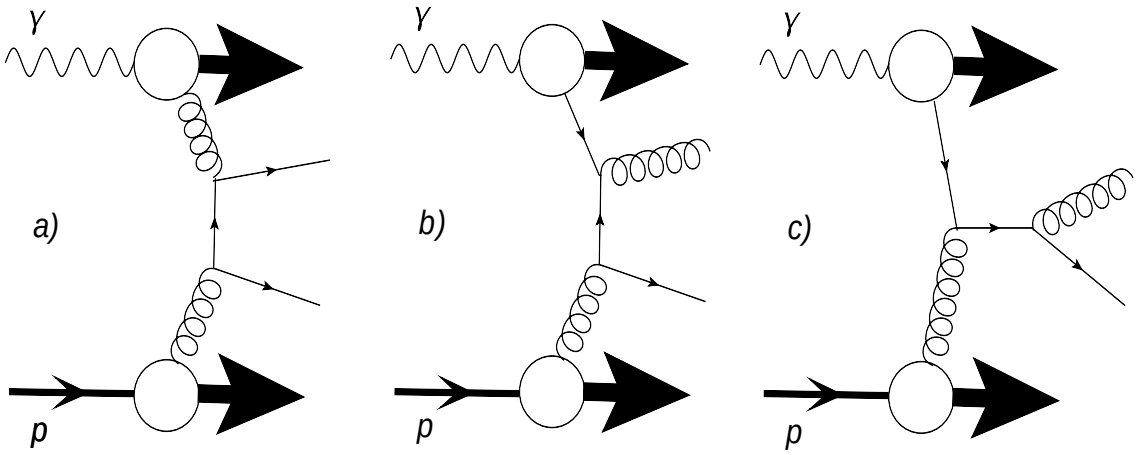

Figure 2.9: Examples of LO resolved photoproduction processes for dijets: a) *Gluon-Gluon Fusion*, b) and c) *Flavor Excitation* from the photon.

- The photon structure function increases with increasing energy fraction x_γ (2.30) of the quark from the photon.
- The structure function of the quasi-real photon depends directly on the scale μ^2 at which it is probed by a highly virtual photon. In hadronic structure functions, μ^2 only enters via the QCD evolution equations.

QCD corrections to the simple QPM photon structure function can be calculated, e.g., from the DGLAP evolution equations. In these evolution equations the first term [Erd97] on the right hand side is an inhomogeneous and peculiar to the photon: it reflects the contribution of quarks from the pointlike coupling of the photon to a quark−anti-quark pair [H198a]. It is non-trivial that these QCD corrections preserve the $\ln \mu^2$ dependence of the QPM photon structure function (analogous to the first term on the right side in equation 2.21) [Wit77]. The leading order perturbative QCD prediction for the quark density in the photon is given by:

$$f_{q/\gamma}(x_\gamma) = e_q^2 \frac{\alpha}{\pi} \left(x_\gamma^2 + (1 + x_\gamma)^2\right) \ln \frac{\mu^2}{\Lambda^2_{\mathrm{QCD}}}, \tag{2.28}$$

where μ is the scale at which the photon is probed in the parton−parton collision and Λ_{QCD} is an asymptotic scale parameter below which the calculations cannot be explored perturbatively using the renormalization group. The increase of the parton density with increasing scale $\left(f_{q/\gamma} \sim \ln \frac{\mu^2}{\Lambda_{\mathrm{QCD}}}\right)$ is clearly different from the behavior of the parton den-

sity distributions of hadrons and is referred to as anomalous hadronic structure of the photon [H198a].

The corresponding expression for the photon structure function which accounts for the pointlike/anomalous photon contribution is:

$$\mathrm{F}_2^{\gamma}(\mathrm{x}_{\gamma}, \mu^2) = 3 \sum_{n_f} e_q^4 \frac{\alpha}{\pi} \mathrm{x}_{\gamma} \left(\mathrm{x}_{\gamma}^2 + (1 + \mathrm{x}_{\gamma})^2 \right) \ln \frac{\mu^2}{\Lambda_{\mathrm{QCD}}^2}. \tag{2.29}$$

The deep inelastic electron-photon scattering experiments can, in principle, directly measure the photon structure function F_2^{γ}, which could give a precise determination of the QCD parameter Λ_{QCD} [Erd97].

Since one speaks of two processes, the direct and resolved photoproduction, it is of great importance to find a discriminating parameter in order to distinguish both processes from each other. For this purposes a variable x_{γ} was used; it describes the fraction of the photon's 4-momentum which is carried by the parton which participates in the hard interaction on the photon side:

$$\mathrm{x}_{\gamma} = \sum_i \frac{\mathrm{E}_{\mathrm{T},i} e^{-\eta_i}}{2\mathrm{E}_{\gamma}} = \sum_i \frac{\mathrm{E}_{\mathrm{T},i} e^{-\eta_i}}{2\mathrm{yE}_e}, \tag{2.30}$$

where, for the dijet case, the summation is again done over the outgoing partons from the hard interaction. $\mathrm{E}_{\mathrm{T},i}$ and η_i are the transverse energy and pseudorapidity of the i^{th} outgoing parton. From equation 2.30 it is clear that x_{γ} is analogous to x_{P} in equation 2.26. Again, as studies have shown, the observable quantity, $\mathrm{x}_{\gamma}^{\mathrm{obs}}$, extracted from information from the HFS jets, is, in general, a good approximation of x_{γ}. Thus, the two leading jets are taken for the calculation of $\mathrm{x}_{\gamma}^{\mathrm{obs}}$:

$$\mathrm{x}_{\gamma}^{\mathrm{obs}} = \frac{\mathrm{E}_{\mathrm{T,1st}} e^{-\eta_{\mathrm{1st}}} + \mathrm{E}_{\mathrm{T,2nd}} e^{-\eta_{\mathrm{2nd}}}}{2\mathrm{yE}_e}. \tag{2.31}$$

As already said, one can use $\mathrm{x}_{\gamma}^{\mathrm{obs}}$ as an observable to separate to some extension the two classes of photoproduction interactions. In direct photoproduction the momentum fraction is purely carried by the virtual photon and such $\mathrm{x}_{\gamma} = 1$, whilst in resolved photoproduction the fraction is taken as a part from the photon and thus $\mathrm{x}_{\gamma} < 1$. There are two points to consider: first, high energy photoproduction of dijets tend to be dominated by direct photoproduction and second, both $\mathrm{x}_{\mathrm{P}}^{\mathrm{obs}}$ and $\mathrm{x}_{\gamma}^{\mathrm{obs}}$ are within the range of $[0, 1]$.

This simple QPM picture is modified due to QCD and non-perturbative corrections, i.e. parton showers in the initial and final state and the fragmentation of partons into jets. Thus, $\mathrm{x}_{\gamma}^{\mathrm{obs}}$ becomes smeared and a precise separation of direct and resolved dijet events is not possible as for the direct process the $\mathrm{x}_{\gamma}^{\mathrm{obs}} \leqslant 1$.

Nevertheless, studies have shown that dijet event samples can be separated into direct and resolved enhanced samples just by means of a cut on $\mathrm{x}_{\gamma}^{\mathrm{obs}}$. For example,

events where $x_\gamma^{obs} > 0.8$ are classified as direct photoproduction events and those which have $x_\gamma^{obs} \leqslant 0.8$ are classified as resolved photoproduction events.

2.4 Dijets Cross Section in Photoproduction

The factorization theorem (2.2.2) of perturbative QCD allows to obtain the γp dijet cross section as a convolution of the partonic cross sections with the renormalized parton density functions of the proton $f_{i/p}$ and the photon $f_{j/\gamma}$.

The cross section is usually divided into a sum of two components, the direct part $\sigma_{\gamma p}^{direct}$ and the resolved part $\sigma_{\gamma p}^{resolved}$. This is valid only in LO and depends on a photon factorization scale μ_γ [Car02]. These two components can be expressed as:

$$\sigma_{\gamma p}^{direct} = \sum_i \int d\xi_p f_{i/p}(\xi_p, \mu_p) \hat{\sigma}_{i\gamma}(\hat{s}, \mu_\gamma, \mu_p, \alpha_s(\mu_r), \mu_r), \tag{2.32}$$

$$\sigma_{\gamma p}^{resolved} = \sum_{j,i} \int d\xi_\gamma f_{j/\gamma}(\xi_\gamma, \mu_\gamma) d\xi_p f_{i/p}(\xi_p, \mu_p) \hat{\sigma}_{ij}(\hat{s}, \mu_\gamma, \mu_p, \alpha_s(\mu_r), \mu_r), \tag{2.33}$$

where $\hat{s} = \xi_p \xi_\gamma y s$ is the squared center-of-mass energy of the hard subprocess and $\sqrt{s}$ is the total center-of-mass energy in the ep-system. μ_p is the proton factorization scale. The total cross section on the left hand side of equation 2.20 is obtained by integrating over y, ξ_p and ξ_γ. The partonic cross sections $\hat{\sigma}_{i\gamma}$ and $\hat{\sigma}_{ij}$ contain a further integration over an internal degree of freedom, e.g. the transverse energy, P_T or $\cos\theta^*$, the scattering angle in the center-of-mass system of the partonic two body reaction[9]:

$$|\cos\theta^*| = \left| \tanh\left(\frac{\eta_1 - \eta_2}{2} \right) \right|. \tag{2.34}$$

2.4.1 The Parton Scattering Angle

In QCD theory the cross sections of elastic parton-parton scattering processes are predicted. The parton scattering angle $\cos\theta^*$ in the parton center-of-mass system, for given initial-state parton energies E_1 and E_2, is calculated (Figure 2.10). For massless partons the Lorentz invariant Mandelstam variables $\hat{s}$, $\hat{t}$, $\hat{u}$ are directly related to the parton energies and the scattering angle:

$$\hat{s} = 4E_1E_2, \tag{2.35}$$

$$\hat{t} = -\frac{\hat{s}}{2}(1 - \cos\theta^*), \tag{2.36}$$

$$\hat{u} = -\frac{\hat{s}}{2}(1 + \cos\theta^*). \tag{2.37}$$

[9] See equation 2.39 for the definition of η.

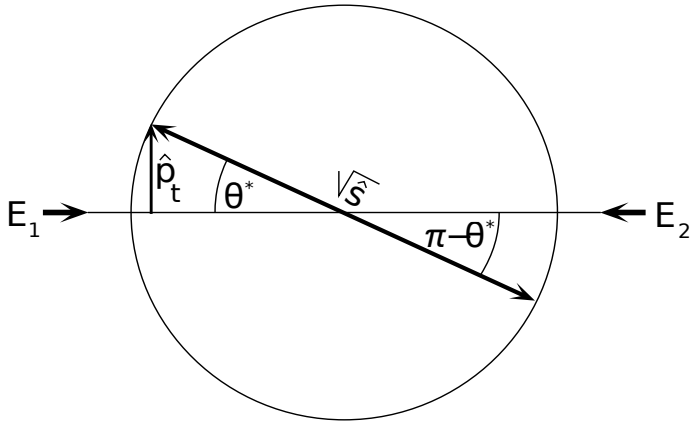

Figure 2.10: An elastic parton scattering process is shown in the parton-parton center-of-mass system. $\sqrt{s}$ is the center-of-mass energy, $\hat{p}_t$ is the transverse momentum of the scattered partons and θ^* is the scattering angle. This figure is taken from [Erd97].

The sum of all of the Mandelstam variables is equal to zero ($\hat{s} + \hat{t} + \hat{u} = 0$) which means that only two of them are independent of each other. For instance, for a given parton center-of-mass energy $\sqrt{\hat{s}}$, the cross sections vary only with the parton scattering angle θ^*.

Figure 2.11 shows the distributions of $\cos\theta^*$ in the parton-parton center-of-mass system for different LO matrix elements [Erd97]. In the scattering region of $\theta^* = 90°$, the difference between matrix elements reaches three orders of magnitude. The dominant parton cross section is from the resolved $gg \to gg$ process. Most of the matrix elements diverge at $\cos\theta^* = 1(-1)$, which corresponds to small-angle forward (backward) scattering.

In practice, experiments are not able to distinguish the forward and backward parton scattering, that is why only the absolute value of $\cos\theta^*$ is appropriate. Figure 2.12 shows the shapes of the matrix elements of different resolved and direct processes as a function of $|\cos\theta^*|$. One observes the similar rise of the resolved photon processes, although, they are predicted to rise more steeply than the direct photon processes. Large $|\cos\theta^*|$ region corresponds to small θ^*, which is roughly corresponds to small E_T.

2.5 Jet Definition

In the hard interaction of photoproduction hadronization processes and color confinement convert the colored partons into colorless particles − hadrons. The collimated bundle/spray of these particles are collectively called jets. Jets are the footprints of partons; studies and experiments have shown that observed jet dynamics correlates well with underlying parton dynamics.

In order to compare the partonic cross sections predicted by perturbative QCD with the measured experimental distributions (observables) one requires event properties to have a close correspondence between partonic and hadronic final states, so-called

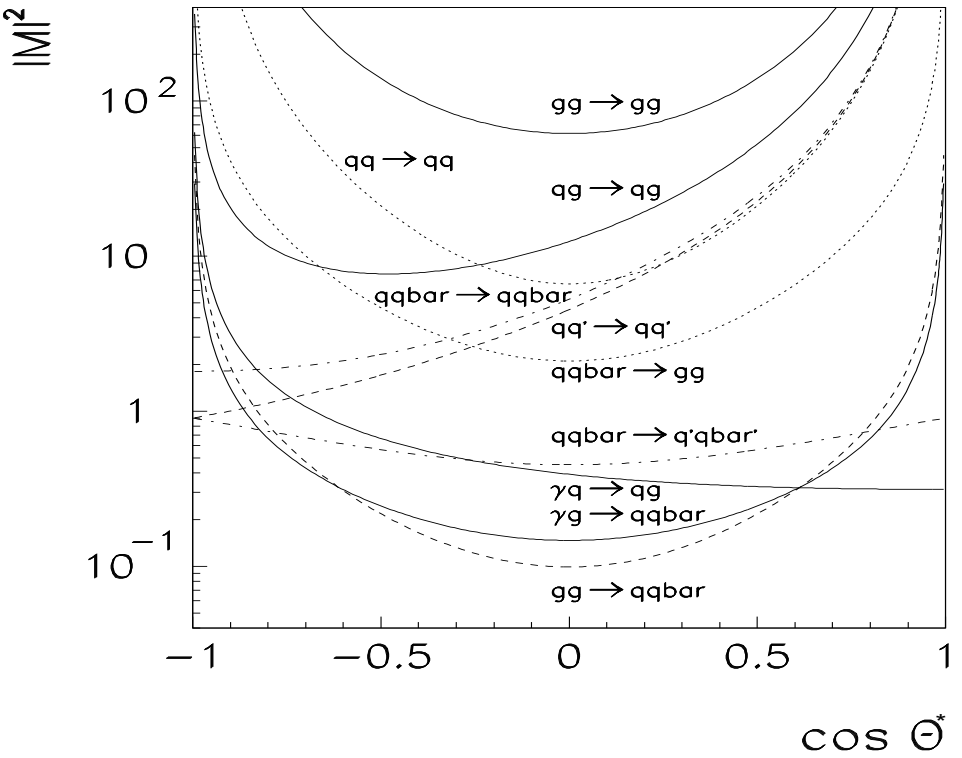

Figure 2.11: Parton scattering angle θ^* in the parton-parton center-of-mass system for different LO QCD matrix elements [Erd97].

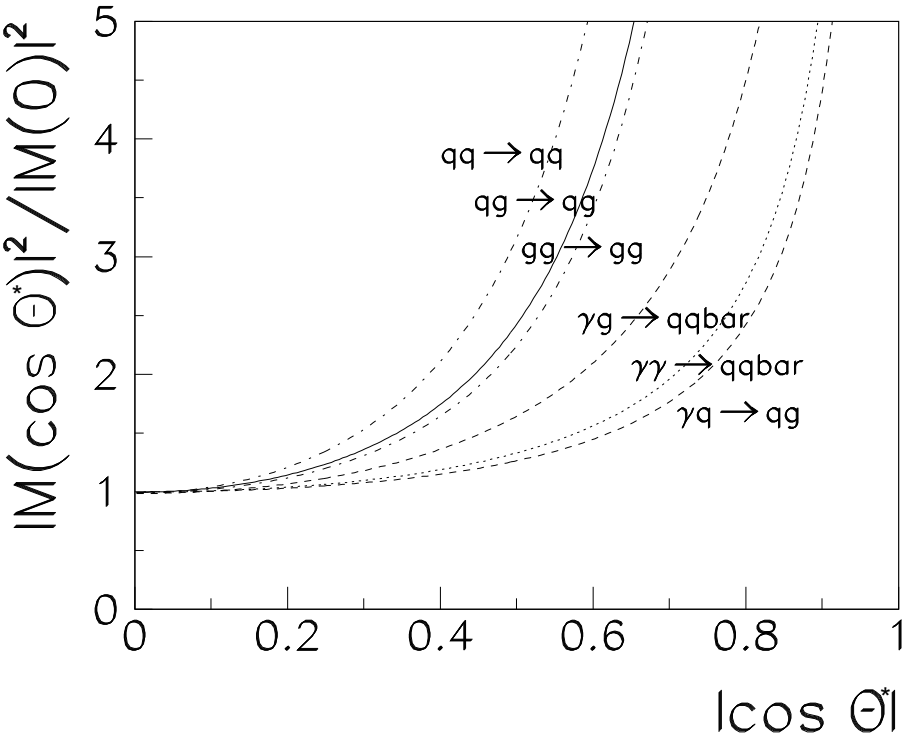

Figure 2.12: The shapes of the parton angular θ^* distributions for different parton scattering processes. For the resolved γ interactions the matrix elements rise more steeply than for the direct γ processes [Erd97].

"jet observables". Showering and hadronization of the primary partons as well as color confinement processes are long distance processes which should weakly effect this correspondence. Of course, the effect is strongly correlated with the exact definition of how the jet observables are calculated. This is accomplished by means of the so-called *jet finder* algorithms which are present on the market and they are subject to take care of several criteria outlined below:

- Infrared divergencies, or the emission of soft or collinear gluons.
- Technically calculable for all levels.
- Small hadronization corrections.
- Invariance under longitudinal boost.

Thus, it is of great importance that a jet finding algorithm is defined in such a way that the resulting jets are infrared safe [Sey95].

In order for an algorithm to be considered infrared safe the configuration of N and $N+1$ input particles of a jet has to be identical under two limits. First, the infrared safety demands that the observable must not change if one or more partons with zero momentum are present in the final state or if they are omitted completely. It means the energies of the $(N+1)^{th}$ momenta tend to be zero. Second, the treatment of a final state with two collinear particles and the treatment of the state where these particles are replaced by one of them must be identical and it must not have any influence on the observable.

At *detector level*[10], particles are reconstructed from signals in the detector and then used as an input for the jet algorithm. At *hadron level* the input for the jet algorithm are the stable particles generated by the MC event generator (see chapter 4). It is vital that the same behavior is seen on detector, hadron and parton levels, yielding small detector and hadronization corrections.

And finally a jet algorithm is invariant under longitudinal boost if the variables used during the jet reconstruction procedure are longitudinally invariant. Examples of such variables are the pseudorapidities (if jets/partons are massless), invariant mass or the transverse energies of jets.

2.5.1 The $k_\perp$ Algorithm

A jet finding algorithm used in this work is the $k_\perp$ algorithm also known as longitudinally invariant algorithm [CDSW93] and it is used in the inclusive mode [ES93]. This algorithm satisfies the requirements listed in section 2.5. It is implemented within the H1 software code which first begins with a list of objects[11] and iteratively combines pairs of objects depending on their transverse energy $\mathrm{E_T} = \mathrm{E}\sin\theta$ and closeness parameter R_{ij} until a stopping condition is reached:

[10] Detector level and hadron level refer to the event after and before it has passed through the detector, respectively. See also section 6.2.

[11] The word object is generally referred to the input objects and can represent partons, stable particles, calorimeter clusters or even protojets from previous iterations of combination steps of the algorithm.

1. A list of all objects and an empty list of jets is ready for the iteration procedure.
2. For every pair of objects in the final state a distance d_{ij} is calculated such that:
$$d_{ij} = \min(\mathrm{E}_{\mathrm{T},i}^2, \mathrm{E}_{\mathrm{T},j}^2) \cdot R_{ij}^2, \tag{2.38}$$
where $R_{ij}^2 = \Delta\eta_{ij}^2 + \Delta\phi_{ij}^2$ is the closeness parameter between object i and j also known as distance in the $\eta - \phi$ plane, $\Delta\eta_{ij} = \eta_i - \eta_j$, $\Delta\phi_{ij} = \phi_i - \phi_j$. The pseudorapidity is defined as:
$$\eta = -\ln\tan\left(\frac{\theta}{2}\right), \tag{2.39}$$
where θ refers to the particle's polar angle.
3. For each object i, the distance to the beam is calculated:
$$d_i = \mathrm{E}_{\mathrm{T},i}^2 \cdot R_0^2, \tag{2.40}$$
where R_0 is a free parameter of the algorithm and chosen to be 1.
4. Find the minimum d_{min} of all d_{ij} and d_i. If d_i is the smallest number, the object is considered complete and removed from the list of objects and placed into the list of jets. If d_{ij} is the smallest number then both objects i and j are merged into a single "pseudoobject". In both cases the list of objects is updated, i.e. objects i and j are removed.
5. The steps $2 - 4$ are repeated until the list of objects is exhausted.
6. The result of the iteration procedure is a list of complete objects ordered in $\mathrm{E_T}$ ($\mathrm{P_T}$ for massless objects) which are assigned to a single jet.

Objects are merged in this work according to the Snowmass convention using the $\mathrm{P_T}$-recombination scheme [Ber92]:

$$\mathrm{E}_{\mathrm{T},ij} = \mathrm{E}_{\mathrm{T},i} + \mathrm{E}_{\mathrm{T},j}, \tag{2.41}$$

$$\eta ij = \frac{\eta_i \mathrm{E}_{\mathrm{T},i} + \eta_j \mathrm{E}_{\mathrm{T},j}}{\mathrm{E}_{\mathrm{T},i} + \mathrm{E}_{\mathrm{T},j}}, \tag{2.42}$$

$$\phi ij = \frac{\phi_i \mathrm{E}_{\mathrm{T},i} + \phi_j \mathrm{E}_{\mathrm{T},j}}{\mathrm{E}_{\mathrm{T},i} + \mathrm{E}_{\mathrm{T},j}}. \tag{2.43}$$

For the massless jets the rapidity and pseudo rapidity are equivalent, as are the transverse energy, $\mathrm{E_{T,jet}}$ and transverse momentum, $\mathrm{P_{T,jet}}$.

It is worth to mention that the recombination scheme is not unique. Other schemes are the covariant E-scheme, where the 4-momenta of objects i and j added, the $\mathrm{P_T^2}$-scheme, the $\mathrm{E_T}$-scheme or the $\mathrm{E_T^2}$-scheme.

The choice of the $\mathrm{P_T}$-recombination scheme was motivated by the fact that the same recombination scheme is used in the NLO calculations.

CHAPTER 3

HERA AND THE H1 DETECTOR

3.1 The HERA Accelerator

The HERA [W+81] accelerator was the first lepton-hadron collider in the world. Its operation started in 1992 and finished at the end of June 2007. It is the largest component of the various accelerators (figure 3.1), with a ring circumference of 6.3 km, and it is located at the Deutsches Elektronen-Synchrotron (DESY) laboratory in Hamburg, Germany. It is a unique facility to study the scattering of electrons[1] and protons accelerated to energies of 27.5 GeV and 920 GeV, respectively.

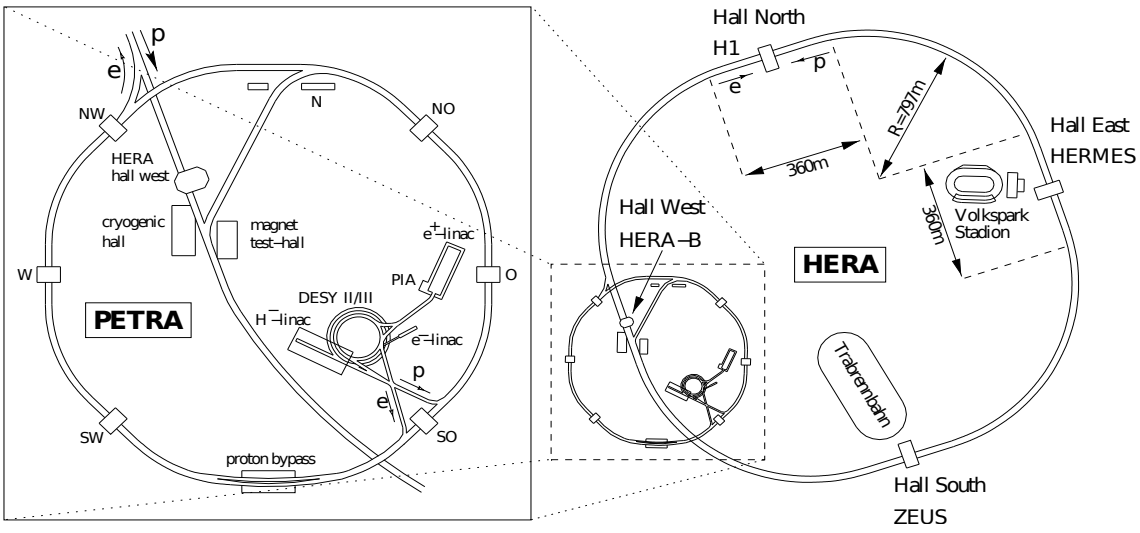

Figure 3.1: Overview of the HERA storage rings with the two main experiments H1 and ZEUS and the two fixed target experiments HERMES and HERA-B. A zoomed view of the pre-accelerators is presented on the left side.

[1] At the Hadron-Elektron-Ring-Anlage (HERA) electrons or positrons were used during different periods of time. Throughout this thesis both are generally referred to as electrons, if not otherwise stated.

The HERA beams were brought into collision at two interaction points, in the hall North − the realm of the H1 experiment, and in the hall South, where the ZEUS experiment was based. The fixed target experiment, HERMES, was in the East hall. This experiment used the longitudinally polarized electron beams on a gas target to study the spin structure of the nucleons. The West hall was used by the HERA-B experiment which was focused to measure CP violation in decays of B mesons.

In the linear accelerators (LINAC I/II) electrons were preaccelerated to 450 MeV. Afterwards they were injected into the DESY II storage ring, accelerated to 7.5 GeV and further transfered into the Positron-Elektron-Ring-Anlage (PETRA), where they were accelerated to 14 GeV. Finally, after transfer of the beam to HERA, the electron beam was further accelerated to an energy of 27.5 GeV. The storage ring used for the electron beam was equipped with warm (non-superconducting) magnets keeping the electrons on their circular track by a magnetic field of 0.17 Tesla. The source of protons were negatively charged hydrogen ions, preaccelerated to 50 MeV in a linear accelerator. The protons were then injected into the proton synchrotron DESY III and accelerated further to 7 GeV. After being transferred to PETRA, they were accelerated to 40 GeV and finally injected into their storage ring inside the HERA tunnel, where they were further accelerated to an energy of 920 GeV. To keep the protons on track the proton storage ring used superconducting magnets with $\mathbf{B} \approx 4.5$ Tesla.

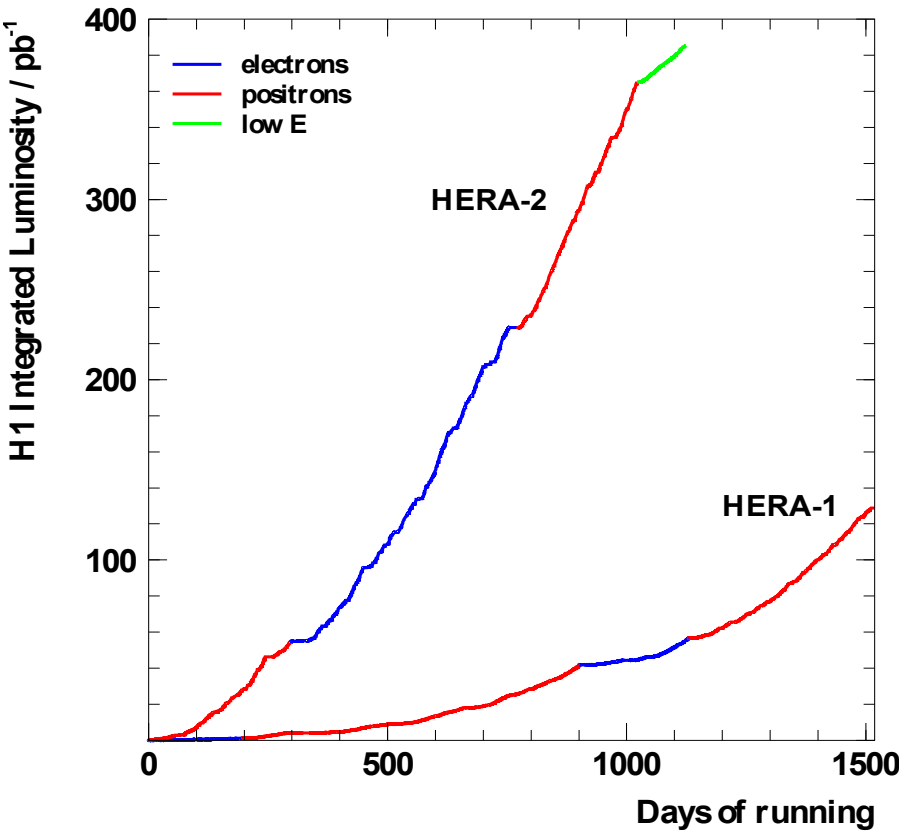

Figure 3.2: Integrated luminosity delivered by HERA I and HERA II phase together with the low and medium proton energy running period.

In the year 2000 the so-called HERA I phase was finished and the detectors together with the collider were upgraded for the HERA II phase delivering later on an increase in luminosity by a factor of 5. Figure 3.2 presents the integrated luminosity for the whole HERA running period as well as the luminosity collected during the low and medium proton energy runs in the year 2007.

For each of the electron and proton beams inside the accelerator rings, 210 particle bunches were injected, each containing approximately 10^{11} particles. The distance of 28.8 m between every bunch in each beam corresponds to the bunch crossing time interval of 96 ns or to the collision rate of 10.4 MHz. Because of the presence of the large amount of background in the experiments, a procedure to deal with it was developed. This procedure included the filling of 10 electron (proton) bunches without a corresponding proton (electron) bunch partner, so-called *pilot bunch*. Investigating events with such electron or proton pilot bunches, non-*ep* induced background reactions could be studied, e.g. beam-gas events originating from proton collisions with the remaining gas nuclei in the beampipe, beam halo muons and muons of cosmic radiation.

3.2 The H1 Detector

The H1 detector is a general purpose detector designed for the study of *ep* interactions at HERA. It is arranged cylindrically around the beam axis and provides nearly full coverage of the solid angle. The main limitations are due to the space occupied by the beampipe and the strong superconducting focusing magnets installed inside the experiment during the luminosity upgrade for HERA II. At HERA the center-of-mass of *ep* collisions is boosted along the direction of the incoming proton, therefore the H1 detector is designed asymmetrically. The coordinates are defined using right-handed Cartesian $(\mathrm{x}, \mathrm{y}, \mathrm{z})$ and spherical (r, θ, ϕ) coordinate systems. The nominal interaction point defines the origin of these systems. The z-axis is pointing along the direction of flight of the incoming proton. The x-axis points to the center of the HERA storage ring and the y-axis points upwards. The azimuthal angle ϕ lies in the xy-plane such that $\phi = 0$ points to the positive x-direction, and finally the polar angle θ is measured from the positive z-axis (see figure 5.4).

Figure 3.3 reflects the shell structure design of the H1 detector. Starting from the most inner part the tracking detectors were placed, they had a purpose to measure the momentum and charge of the particles produced in *ep* collisions. The tracking detectors were followed by the electromagnetic and hadronic calorimeters, which measure the energy of these particles. The super conducting solenoid generates a magnetic field of 1.15 Tesla. It is located outside the calorimeters to avoid adverse effects on the calorimetric energy measurement of particles, particularly the scattered electron and photons. The iron return yoke for the magnetic flux was used as a muon detector.

The detector components important for this analysis are presented in the following sections. For a very detailed description, please refer to [A$^+$97a, A$^+$97b] .

H1 Detector at HERA

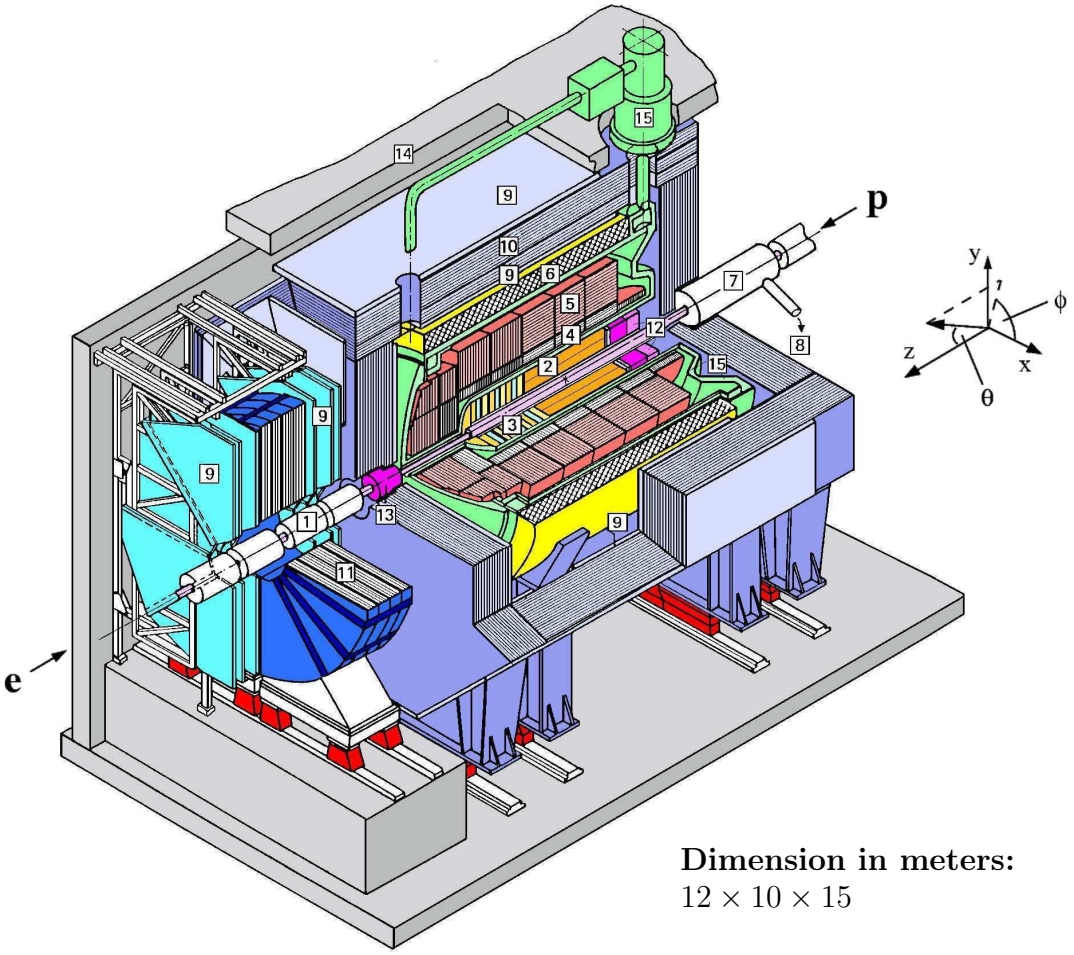

1 beam pipe	9 muon chambers
2 central tracking chamber	10 instrumented iron
3 forward tracking chamber	11 muon toroidal magnet
4 electromagnetic LAr calorimeter (Pb)	12 warm calorimeter (SpaCal)
5 hadronic LAr calorimeter (Fe)	13 forward calorimeter
6 superconducting solenoid	14 concrete shielding
7 compensating magnet	15 cryostat
8 Helium cooling	

Figure 3.3: Schematic drawing of the H1 detector with its main components.

3.3 Tracking

The most inner part of the H1 detector is occupied by a tracking system which consists of silicon strip detectors, drift chambers and multi-wire proportional chambers. All these detectors measure the flight path of charged particles, i.e. the tracks from which the primary and secondary vertices are reconstructed. The magnetic field which is parallel to the z-axis forces charged particles to have a helix as their trajectories and thus makes it possible to measure the sign of their charge and their momentum.

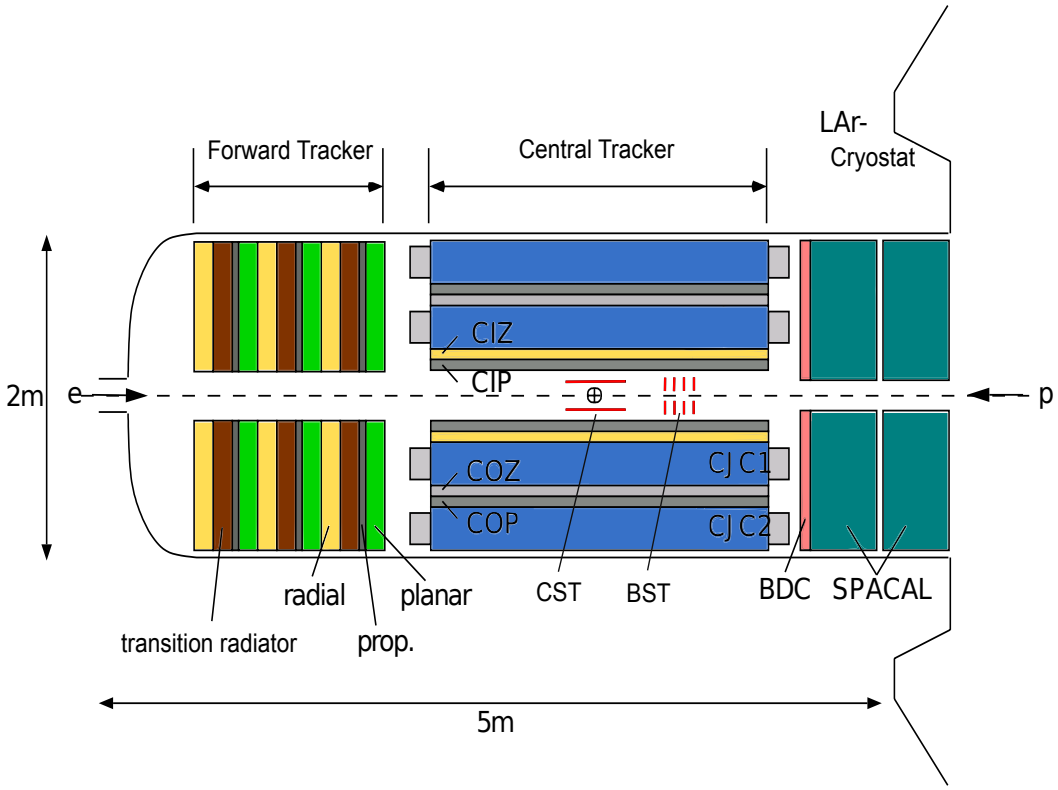

Figure 3.4: A schematic longitudinal view of the H1 tracking system.

Figure 3.4 shows a schematic overview of the different sub-detectors of the H1 tracking system in the rz-plane. The tracker is divided into central (CTD) and forward (FTD) tracking devices. During the HERA II upgrade the Backward Drift Chamber (BDC) was replaced by the Backward Proportional Chamber (BPC). The purpose of the BPC was to improve the position measurement of particles going into the backward direction.

3.3.1 The Central Track Detector (CTD)

The CTD is a combination of different sub-detectors. It covers the angular range of $15° < \theta < 165°$ with a full azimuthal acceptance (see figure 3.5).

- The Central Silicon Tracker (CST) is located around the nominal interaction point in the region $29° < \theta < 151°$. It consists of 32 ladders in two layers at

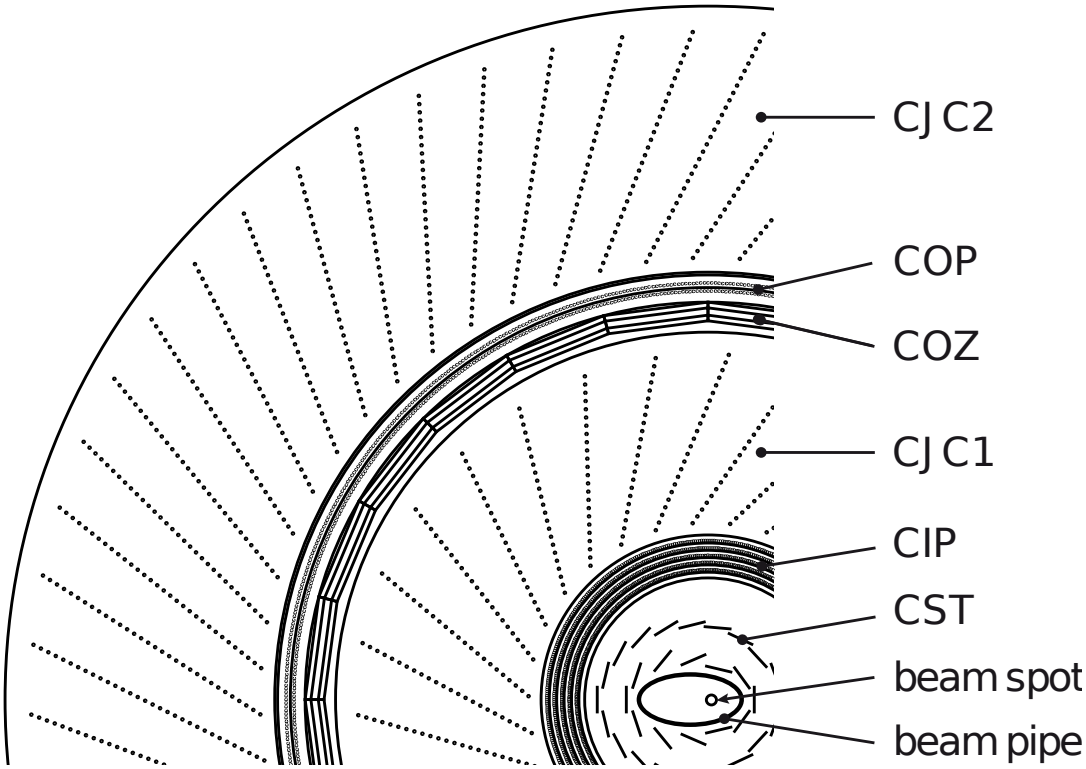

Figure 3.5: The central tracking system in the $r\phi$ plane.

a radius of 6 cm and 10 cm, and allows to measure the r and ϕ coordinates of a track with an impact parameter resolution of 57 µm. The tracker was used to improve the precision measurement of the tracks which have been reconstructed with CJCs.

- The Central Jet Chambers (CJCs), two large concentric drift chamber detectors, covered an angular range of $15° < \theta < 165°$ with an active length of 220 cm along the beam pipe and radial extension of $20.3 < r < 45.1$ cm (CJC1) and $53.0 < r < 84.4$ cm (CJC2). The CJC1 had 30 drift cells each consisting of 24 anode wires, and the CJC2 was designed with 60 drift cells and every cell had 32 anode wires. The anode wires were strung parallel to the z-axis and the magnetic field, **B**. The cells are tilted by about 30° such that the ionization electrons drift approximately perpendicular to tracks for a wide range of particle transverse momenta and, in addition, high P_T tracks which traverse straight through the chambers are measured in at least two cells. This ensures an optimum track resolution in z-coordinate and solves the usual drift chamber ambiguity − the wrong mirror track segments, which do not point to the event vertex and obstruct only small parts of a real track in the opposite half cell. This also results in a precise time of passage of particle and thus of the T0 measurement.

- The Central Inner Proportional Chamber (CIP), a multiwire proportional chamber [H199b], is a replacement of the HERA I Central Inner z-Chamber

(CIZ). It is placed at an average radial distance of 16.2 cm covering the polar angle acceptance of $9° < \theta < 171°$. It has a diameter of 40 cm and consists of five radial layers. It is able to supply fast timing signals well within the time difference between HERA bunch crossings of 96 ns and thus allows to make first trigger level decisions based on charged particle tracks.

- The Central Outer z-Chamber (COZ), a thin drift chamber is designed as a polygonal chamber to improve the track reconstruction in the rz-plane. It is 2.59 m long and 25 mm wide, contains 4 layers of anode wires with 16 and 24 rings and has a polar angle coverage of $25° < \theta < 156°$. Its anode wires were strung transverse to the z-axis. Thus, electrons drift along the beam axis and provide a more precise measurement of the z-coordinate then the one obtained using charge division from the CJC chambers.

3.3.2 The Forward Track Detector (FTD)

The FTD is an ensemble of drift chambers designed to trace tracks in the polar angle range of $5° < \theta < 25°$. The left side of the figure 3.4 shows integrated assembly of three identical super-modules. Each super-module has three planar drift chambers oriented in different wire geometries: a MWPC for fast triggering, a passive transition radiator and a radial wire drift chamber which provides accurate rϕ (drift coordinate) information.

3.4 Calorimetry

The calorimeter system of the H1 detector closed up the complete tracking system. It was designed to provide identification and precise energy measurement of electrons, photons and hadronic particles as well as to establish a good performance in the measurement of jets with a large number of particles. The H1 calorimeter system consists of the following components:

- the Liquid Argon (LAr) calorimeter is the main instrument to detect the hadronic final state (HFS) in general and the scattered electron in the regime of high $Q^2 > 100$ GeV^2.

- the "Spaghetti" Calorimeter (SpaCal) is mainly used to identify the scattered electrons in the backward region for $Q^2 \lesssim 100$ GeV^2.

- the Tail Catcher as a part of the Instrumented Iron Yoke

- the Plug calorimeter

The tail catcher and the plug calorimeter have specialized intricate application and are not used in the current analysis.

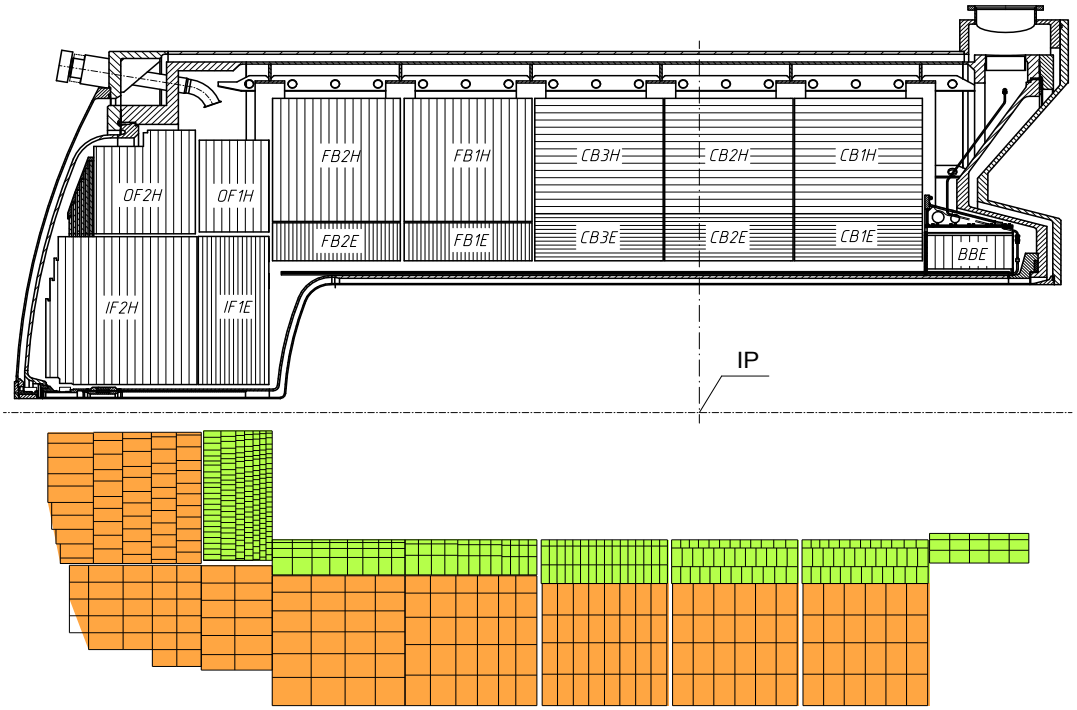

Figure 3.6: Longitudinal view of the LAr calorimeter inside the cryostats. The upper part shows the different calorimeter "wheels" and the sampling structure of the absorber plates. The read-out cells are shown in the lower half in green and orange colors for electromagnetic and hadronic parts, respectively [Nik07].

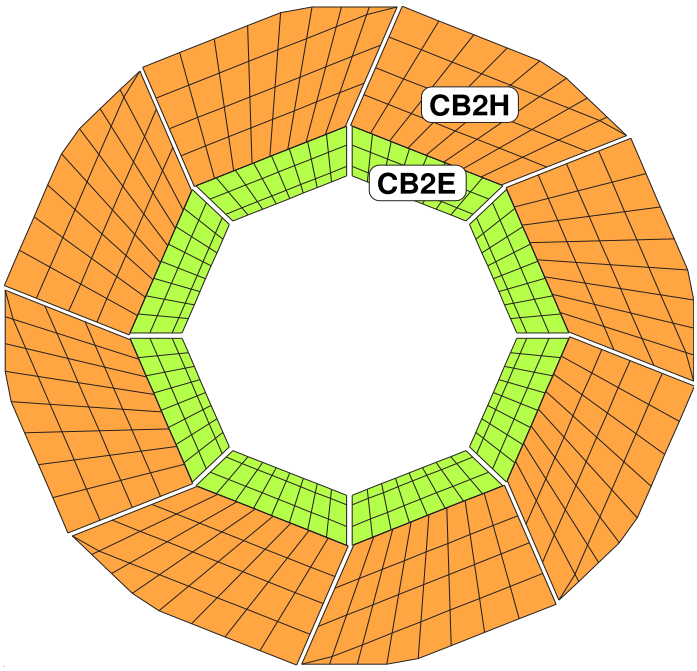

Figure 3.7: The CB2 wheel of the LAr calorimeter segmented in the radial direction, viewed along the proton beam direction. The wheel is divided into eight octants. Again, the electromagnetic and hadronic calorimeters are shown in green and orange colors respectively [Nik07].

3.4.1 Liquid Argon (LAr) Calorimeter

Figure 3.6 presents the longitudinal view of the calorimeter along the beam axis. It consists of eight self-supporting tower "wheels" starting from the most forward IF2 to the most backward BBE, which is the only wheel that has no hadronic section in it. Each of the wheels is segmented in ϕ into eight identical stacks or octants, figure 3.7. Each wheel has been individually calibrated to achieve equal response and finally similar energy resolution and optimal energy scale uncertainty. During the offline analysis one has to take into account the area in-between the wheels and octants, the so-called z-cracks and ϕ-cracks.

Since the development of showers in the active material for particles of electromagnetic and hadronic nature is different the LAr calorimeter provides the possibility to identify the electromagnetically or hadronically interacting particles. It is a sampling calorimeter where an active LAr material is interleaved with layers of absorbers such that only a sample of the energy deposition is measured. The LAr consists of lead absorber plates in the electromagnetic part and of absorber plates made of stainless steal in its hadronic section together with the liquid argon which was chosen as an active material for this calorimeter. This calorimeter was constructed to give a fine granularity for e/π separation and energy flow measurements. It is stable over time and gives a homogeneous response and thus allows for a not too complex calibration procedure. The orientation of the absorber plates is made such that incident particles impact their surface at angles not smaller than 45°. A single incoming particle typically originates an electromagnetic and/or hadronic shower inside the absorber material. The charged particles of the shower in turn ionize the LAr such that part of the primary particle's energy, which is proportional to the electric charge collected on the readout structures, can be read out as a signal. With the help of many calorimetric cells ($\sim$ 44000 readout channels), partially shown in the lower half of figure 3.6, one can ensure a good spatial resolution. Together with the tracking system the LAr plays an important role in the measurement of the HFS.

Technical specifications of the Liquid Argon (LAr) calorimeter		
	Electromagnetic	Hadronic
Angular range	$4° < \theta < 154°$	$4° < \theta < 135°$
Readout channels	30784	13568
Absorber material	Lead	Stainless Steel
Energy resolution	$\sigma_E/E \approx 11\%/\sqrt{E} \oplus 1\%$	$\sigma_E/E \approx 50\%/\sqrt{E} \oplus 2\%$
Radiation length X_0	20 to 30 (X_0^{Pb}=0.56 cm)	
Interaction length λ_I		4.5 to 8 ($\lambda_I^{Fe/Pb} \approx 17$ cm)

Table 3.1: Technical specifications of the LAr calorimeter separated into electromagnetic and hadronic parts. For more details see [H193, H194a]

Electrons and photons and hadronically interacting particles lose their energy differ-

ently. A high energy electron or photon passing through an absorber rapidly loses its energy due to bremsstrahlung and pair production. The produced secondary particles behave similarly if their energy is still high enough, building up a shower. The development of the shower stops when the energy of these secondary particles becomes smaller than the so-called *critical energy*, E_c (< 10 MeV) and subsequent energy loss is dominated by either ionization and excitation for electrons or the Compton effect and the photoelectric effect for photons. The mean distance over which an electron loses all but $\frac{1}{e}$ of its energy, the radiation length, X_0 is used to specify the absorbing quality of the medium for electromagnetic particles.

Hadronic particles inside the absorber material undergo elastic as well as inelastic interactions on the nucleons. Secondary hadrons are created and a hadronic shower is produced. The interaction length, λ_I is used to characterize the longitudinal development of a hadronic shower in a medium. Eventually, ionization losses, nuclear excitations and capture halt further development of the hadronic shower.

Inside hadronic showers energy is spend on nuclear bindings and also on the creation of slow neutrons, muons and neutrinos. Due to this invisible energy, hadronic response of the calorimeter, h is usually smaller compared to the electromagnetic response e:

$$\frac{e}{h} > 1. \tag{3.1}$$

The calorimeters for which the equation 3.1 holds called non-compensating. The LAr calorimeter is a non-compensating one. More technical specifications related to the LAr calorimeter are presented in table 3.1.

3.4.2 The Backward "Spaghetti" Calorimeter (SpaCal)

In this analysis the region of $Q^2 \sim 0$ GeV^2 is of great importance. In this region the scattered electron remains in the beam pipe and is not detected. Events where the scattered electron escapes the beam pipe and is detected in the backward direction have to be rejected. Backward "Spaghetti" Calorimeter (SpaCal) is used to identify and reconstruct such electrons. Moreover, it assists in the measurement of backward jets. Figure 3.8 shows the placement of the SpaCal in the H1 detector.

The SpaCal covers the region in polar angle $153° < \theta < 177.5°$. It was made up of electromagnetic and hadronic modules and is a sampling calorimeter. In both electromagnetic and hadronic sections lead blocks were used as absorber materials with scintillating plastic fibers embedded in a lead matrix. The fibers are running parallel to the z-axis. Shower photons within the absorber produce scintillation light in the fibers, which is amplified by Photomultiplier Tubes (PMTs) and converted into a measurable signal that is proportional to the energy of the shower particles.

With this design high angular resolution and excellent energy resolution for electrons were obtained. The electromagnetic part of the calorimeter had 1192 cells with the size of $4 \times 4 \times 25$ cm^3, containing fibers of 0.5 mm in diameter. It had a length of 27.5 X_0 and together with the hadronic section contained the total energy of scattered electrons. An energy resolution of $\sigma^{em}/E \approx 7\%/\sqrt{E/\text{GeV}} \oplus 1\%$ was achieved [N$^+$96].

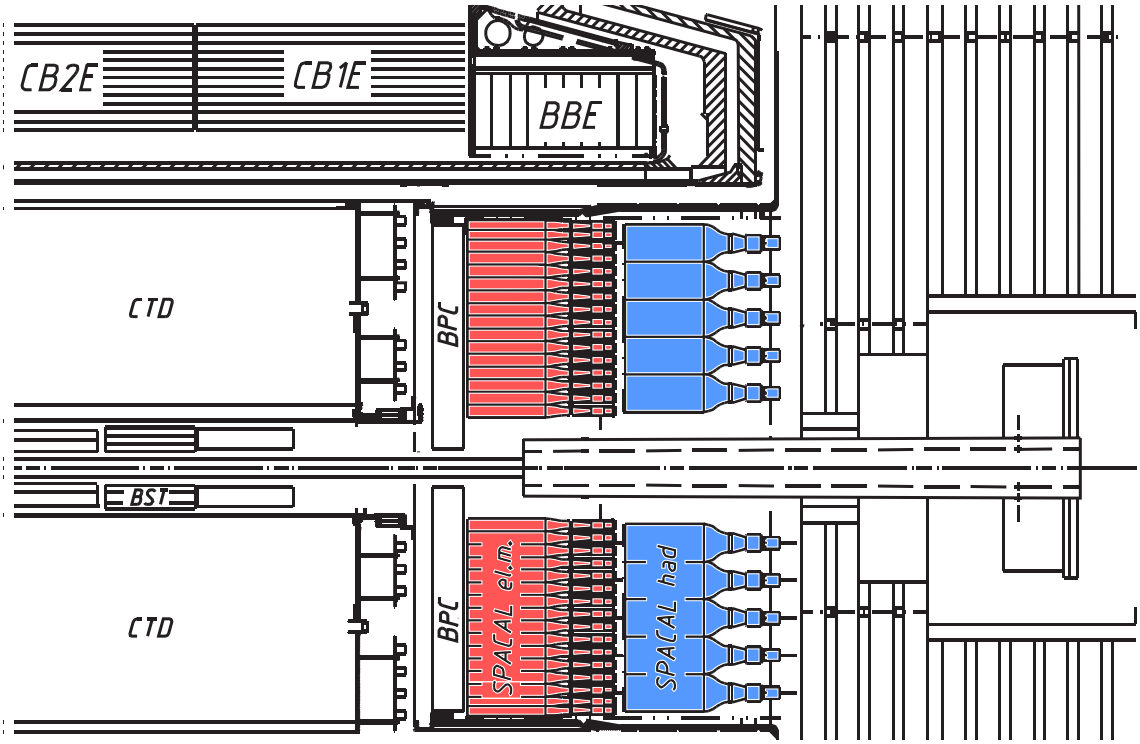

Figure 3.8: The placement of the SpaCal in the H1 detector. The electromagnetic and hadronic calorimeters are presented in red and blue colors respectively.

The hadronic part was build in a similar way as the electromagnetic one. It consisted of 136 calorimeter cells with larger size of $12 \times 12 \times 25$ cm^3. The hadronic section together with the electromagnetic part of the SpaCal added up to about $2\lambda_I$. In test beam measurements, the energy resolution for the hadronic part of the SpaCal was obtained as $\sigma^{had}/\mathrm{E} \approx 50\%/\sqrt{\mathrm{E/GeV}} \oplus 2\%$ [A$^+$96].

3.5 Luminosity Measurement

For a particle collider with beam particles p_1 and p_2, the instantaneous luminosity is defined with equation [Kog10]:

$$\mathcal{L}(t) = \frac{f_0 n_b N_1 N_2}{A}, \tag{3.2}$$

in units of cm^{-2}s^{-1}, f_0 is the revolution frequency, n_b is the number of colliding bunches per revolution, and $N_1(N_2)$ denote the single bunch intensity of type $p_1(p_2)$ particles. A is the effective cross section of the beams. The integrated over time luminosity, equation 3.3, is determined by counting the number of observed events for a specific reaction $p_1 p_2 \to X$ with a well known cross section.

$$\mathrm{L} = \int_T \mathcal{L} dt = \frac{N_{p_1 p_2 \to X}}{\sigma_{p_1 p_2 \to X}}. \tag{3.3}$$

The integrated luminosity, L, is often used in units of inverse picobarns (pb^{-1} $\approx$

10^{-36} cm^2).

The luminosity at H1 is determined via the production of a radiative photon in elastic ep scattering, $ep \rightarrow ep\gamma$. This can be divided into either the Bethe-Heitler (BH) process or the QED Compton (QEDC) scattering. The choice is made depending on the considered phase space. In the BH process [BH34] a photon and a scattered electron, emitted collinear to the incident electron, are captured in the Photon Detector (PD) and in the Electron Tagger (ET), respectively. The advantage of the BH method is the large corresponding cross section, $\mathcal{O}$(100mb), thus tiny statistical uncertainties could be achieved for a small amounts of integrated luminosity. On the other hand there are several sources of possibly large systematic uncertainties, these are:

- acceptance limitations of the small angle detectors (PD,ET),
- synchrotron radiation, emitted by the electron beam as it passes the focusing magnets in the vicinity of the interaction region,
- ep collisions outside the nominal interaction region, which must be accounted for, when analyzing the cross sections with the main detector.

In case of the QEDC scattering the outgoing electron and photon have sizable transverse momenta with respect to the incident electron, whereas the momentum transfer at the proton vertex is close to zero[2]. The typical cross section for this process obtained for the analysis of the HERA luminosity measurement is of the order of $\mathcal{O}$(0.1nb). The statistical uncertainty amounts to 0.8%, and the total systematic error is 2.1% for the whole HERA II phase. In addition a 1.5% of systematic error corresponding to the smaller 2006 $e^{\pm}p$ data sample related to time dependent corrections (the so-called uncorrelated systematic error on DIS event yield) has to be taken. This measurement is taken as a source of the luminosity uncertainty for this analysis since it is in agreement with the BH measurement, which has a slightly higher uncertainty of 3.4%.

3.6 Time-of-Flight (ToF) System

The Time-of-Flight (ToF) system was introduced within the H1 detector in order to efficiently distinguish between the events originating from ep collisions and the ones coming from beam-gas and beam-wall interactions. This system consists of several high time resolution scintillator detectors used in the HERA II phase, these are PToF, FIT, SToF, BToF and LVetowall. Figure 3.9 shows the placement of these components in the H1 detector.

3.7 Triggering and Data Acquisition

The trigger system of the H1 detector was designed in order to select ep events in general and also specific processes and to reject background events, the rate of

[2]If the momentum transfer at the proton vertex becomes large, inelastic processes start to dominate and the reaction becomes sensitive to the proton structure [H112].

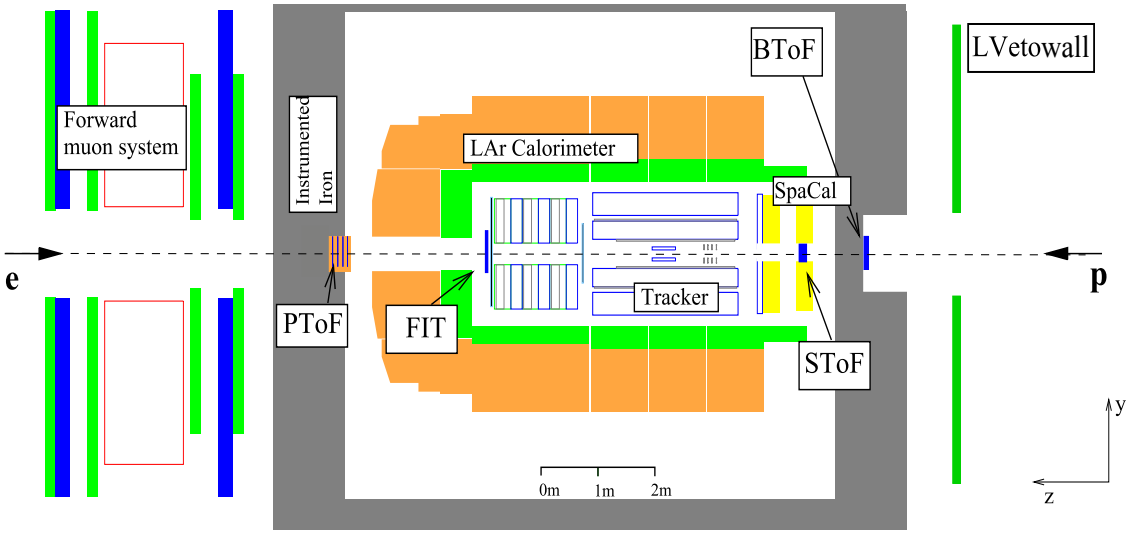

Figure 3.9: The Time-of-Flight (ToF) system located at various places within the H1 detector. LVETOWALL is outside the visible range of this figure. It is located "up-stream" of the proton beam.

which is orders of magnitude higher. The sources of background are due to beam-gas and beam-wall interactions as well as synchrotron radiation from the electron beam. Also the beam halo and cosmic muons and their interactions within or outside of the detector provide a large source of background. A variety of physics processes occurring at HERA are of interest and they span a wide range of cross sections and consequently rates. The total rate of untagged and tagged photoproduction processes at the luminosity of HERA I phase ($L = 1.5 \cdot 10^{31}$ cm^2 s^{-1}) is about 1 kHz and 25 Hz, respectively. The production of W-bosons by comparison has a much lower rate of a few times per week[3]. Since the beam-related background rates scale approximately with the intensity of the beam currents, which after the upgrade to the HERA II phase remained similar to the one of HERA I, the physics-related event rates proportional to the luminosity by a factor of $\sim 4-5$ for HERA II.

The high luminosity corresponds to a large number of collisions (equation 3.2) that might occur at the interaction point and this could only be achieved having a large amount of proton and electron bunches in the accelerator rings. With 210 bunches the time between two successive bunch crossings at HERA was 96 ns corresponding to a frequency of $\sim$ 10.4 MHz. At the same time the rate which the H1 data acquisition system handled was about 50 Hz. Hence, it was of great importance to trigger only on events of interest for the offline physics analysis. For this purpose H1 has implemented a pipelined multi-layered (four levels) trigger system, which is presented schematically in figure 3.10. Each of the levels consecutively filtered the

[3]See table 5 in [A$^+$97a] for more processes.

data, making more and more complex decisions at the cost of increasing the dead time[4] with each trigger level.

3.7.1 The First Trigger Level (L1)

This trigger level consists of 256 Trigger Elements (TEs) from different trigger systems, based on the information from specific subdetectors [A+97a]. The response time of some subdetectors is relatively large, thus the information is first sent into a dead time free pipeline, bunch crossing by bunch crossing, for up to 24 bunch crossings, i.e. 2.3 µs. The information from the TEs is used as an input to the Central Trigger Logic (CTL) where they can be combined using logical operators into 128 *subtriggers*. Each single subtrigger is able to make an L1 trigger decision for a broad variety of physics processes. Some subtriggers were designed as monitor triggers for the purpose of controlling the performance of different subdetectors and for the investigation of trigger efficiencies. If after 24 bunch crossings the CTL decides to keep an event the pipelines are stopped and dead time accumulates until the detector is read out and the pipelines are restarted. The output rate of the L1 system was ~ 1 kHz.

If for some common physics processes one or more subtriggers had too large rate they could be scaled down which was referred to as prescaling. For instance, if a subtrigger was prescaled with n, than it implies that only one out of n events with fulfilled conditions is selected and a corresponding weight is acquired by this selected event. In general, for each event at every trigger level subtrigger decision bits were assigned. These bits are divided into *raw* and *actual* bits. If the defined subtrigger condition satisfies selected criteria than the raw bit is fired. If the verification of this decision was approved, than the actual bit is fired on the corresponding level.

3.7.2 The Second Trigger Level (L2)

The second trigger level was made up of two independent trigger systems running in parallel − the topological trigger and the neural network trigger, L2TT [H198b] and L2NN [H197] respectively. The L2TT used an information grid to derive a topological event signatures from subdetectors. The L2NN made use of multidimensional correlations from outputs of L1 trigger quantities. 13 different neural networks on parallel computers were trained to identify specific *ep* interactions. These outputs from L2NN and L2TT provide the L2 trigger elements for the CTL. The data readout starts in case if at least one L1 actual subtrigger passes an L2 subtrigger validation, thus collecting the information from all subdetectors for usage at the fourth and final trigger level. If it does not pass the L2 level the pipelines of L1 are restarted. The L2 decision time for acceptance or rejection of an event having passed the L1 stage was within 20 µs.

[4]Event processing time needed by each level, while the detector was insensitive for registering new events.

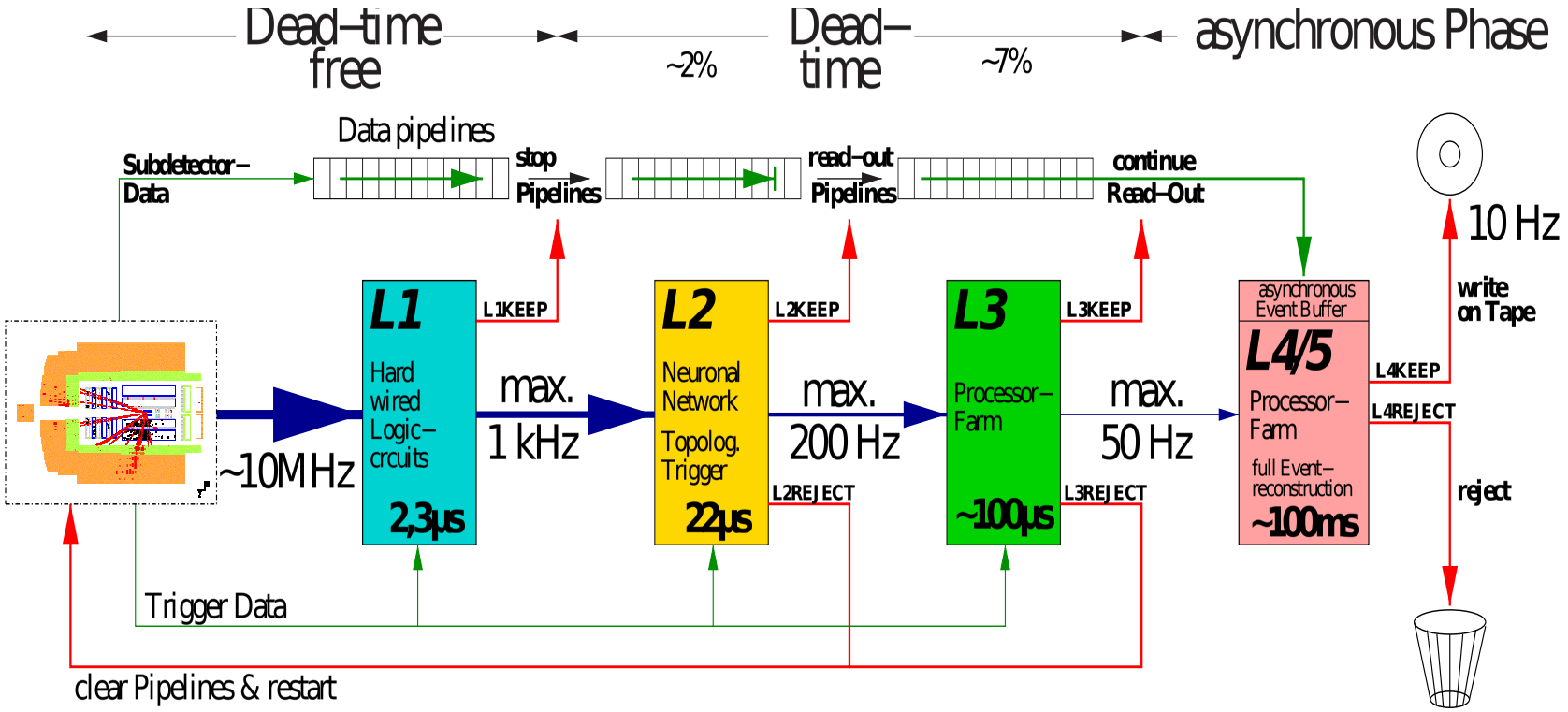

Figure 3.10: A schematic view of the four level H1 trigger system. The input and output rates of each trigger level and also the decision time are presented. The rate is reduced from the input value of 10.4 MHz to an output rate of ~ 10 Hz.

3.7.3 The Third Trigger Level (L3)

The third trigger level was installed during the HERA II period as a part of the Fast Track Trigger (FTT) [Bö7, H101]. With the upgrade of HERA the event rate has increased and the main requirement of FTT was to provide a high reduction factor using the fast reconstruction of tracks from a subset of "hits" in the CJC. The FTT TEs are based on track momenta, multiplicity and topology. The third trigger level reduced the trigger rate by rejecting events after $\sim 100\,\mu s$ available, providing at maximum an output rate of 50 Hz.

3.7.4 The Fourth Trigger Level and Online Reconstruction (L4/5)

Whenever the complete event information from all subdetectors was available, a full event reconstruction was performed on the L4/5 trigger level. The L4/5 filter farm was an asynchronous software integrated into the central data acquisition system and fed the decision making algorithms with the raw data. The logical modules of the L4/5 level distinguished events into certain physics classes. Afterwards the raw event information as well as the reconstructed data were stored on the Production Output Tapes (POTs) and the subset of the POT reconstructed information was duplicated to the Data Summary Tapes (DSTs). The average processing time for this level was $\sim 100\,ms$ providing an acceptance of 10 Hz.

CHAPTER 4

MONTE CARLO EVENT GENERATORS

4.1 MC Generators

MC event generators are sophisticated computational simulations of collisions of high energetic elementary particles. They are used to estimate effects like limited detector acceptance or resolutions and migrations, initial and final state QED radiation, non-perturbative hadronization. A typical event generator simulates the physics process(-es) and insures that a complete set of final state partons as well as particles and their four-momenta are provided. Such a simulation is based on a "random" number generator which in turn gives the name for these type of programs – Monte Carlo (MC) generators. In principle since MC generation rely on repeated calculation an unlimited event samples can be provided, that gives more precision to model the data.

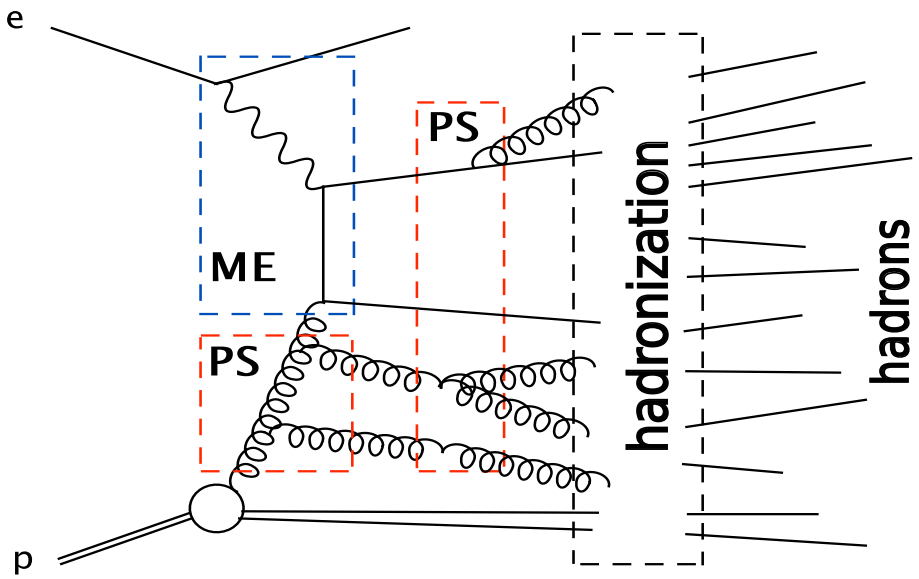

Figure 4.1: Schematic overview of an event generator. Shown are the hard matrix element (ME), initial and final state radiation represented via parton showers (PS) and hadronization. This figure is taken from [Fin06], p. 22.

The generation of events is basically split into separate stages given by the factorization theorem (2.2.2). Figure 4.1 depicts a schematic interpretation of the event generating procedure on the basis of the Boson-Gluon Fusion (BGF) process. The starting point are the PDFs, discussed in 2.2.2. The PDFs define flavor, the energy and the flux of the parton and are evolved according to the DGLAP evolution equations (2.2.2) to the appropriate scale, which is given by the transverse mass m_T. The next step is the hard partonic subprocess characterized by a matrix element (ME), calculable within the pQCD. In the MC generators used within this analysis only leading order ME are implemented. Initial and final state parton showers (PS) mimic QCD radiation down to a cut-off scale. Beyond this scale the hadronization process takes a role and the colored partons are transformed into colorless hadrons.

As soon as the simulated information on the final state particles is available the result of the event generation is fed into the H1 detector simulation program which contains a detailed description of the detector's geometry. This simulation program is a GEANT-based [BHHL78] software package H1SIM [H189]. Afterwards, the real data and MC events have equal format that both could be reconstructed with H1REC (see section 5.1.1) and run through the analysis chain and thus directly used for the comparison with each other.

4.2 Generation of Photoproduction Events

The signal photoproduction events are generated using the Pythia and Herwig MC generation programs. The major difference between the MCs used to generate γp and DIS events is in the treatment of the photon. The DIS case treats the photon as a single object without any photon's intrinsic structure whereas the γp MCs cover a photon structure function (see section 2.4) as well as a multiple interaction scheme.

4.2.1 Multiple Interactions

In H1 a number of studies have been made concerning the multiple interactions in the γp events. The processes, where an underlying event can be considered as everything in addition to the lowest order hard process, consist of contributions coming from higher order QCD radiation, simulated by PS, hadronization and also multiple interactions. This multi-parton interactions take place when the density of partons in the colliding beams is large enough that more than one interaction happens within one collision [MM08].

Figure 4.2 shows the average transverse energy density $\langle E \rangle / (\Delta\eta\Delta\phi)$, in the $|\eta^*| < 1$ region outside the two jets, measured as a function of x_γ^{obs} (equation 2.31). Models which do not have multi-parton interactions cannot describe the measurement whereas models with multi-parton interactions included show a good comparison of data and MC (Pythia mia). Both studies [H196, MM08] have shown that multi-parton interactions are expected within the Pythia models for resolved photons ($x_\gamma < 1$) but not for the point-like photon contributions where $x_\gamma \sim 1$. In Herwig, multiple interactions are simulated by adding low P_T hadrons (the so-called soft underlying event or SUE) to a fraction of the resolved events.

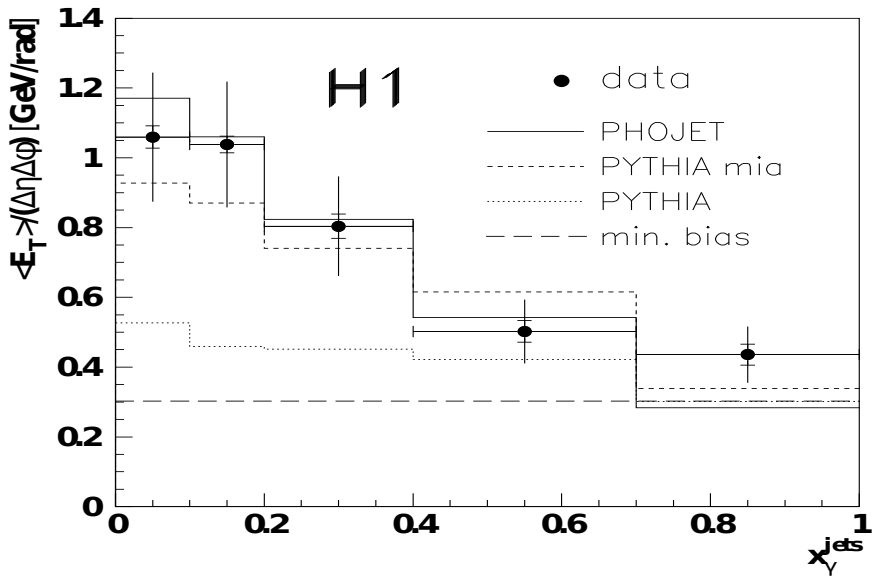

Figure 4.2: Transverse energy flow $\langle \mathrm{E} \rangle / (\Delta\eta\Delta\phi)$, in the $|\eta^*| < 1$ region outside the two jets as a function of $\mathrm{x}_\gamma^{\mathrm{jets}}$ $(\equiv \mathrm{x}_\gamma^{\mathrm{obs}})$ [H196].

4.2.2 Pythia

The Pythia [SMS06] event generator is the main MC program used for the measurements produced in this thesis. It is based on the DGLAP approach of the evolution equations. Two different versions of generatros have been used, Pythia6.1 and Pythia6.4. They both contain Born level QCD hard scattering matrix elements, regulated by a minimum cut-off in transverse momentum. To simulate direct and resolved photoproduction of jets the leading order parametrisations CTEQ5L [PSH$^+$02] for the proton PDF and GRV-LO [GRV92] for the photon PDF were used for Pythia6.1 and CTEQ6L [PSH$^+$02] for the proton PDF and SASGAM 1D [SS95, SS96] for the photon PDF used in the Pythia6.4 generator. For the hadronization process the "Lund string" [GAP83, A$^+$79] fragmentation scheme was applied (as implemented in JETSET [Sjo94] program). Pythia can either be run in the so-called massive or in the massless matrix elements mode for all quark flavors. The latter is often referred to as the full inclusive mode. During the processes of final state emission an outgoing virtual parton of large time like mass generates a shower of partons of lower virtuality. In this case the momentum transfer scale $\hat{\mathrm{P}}_{\mathrm{T}}$ of the out-going partons in the hard subprocess controls the emission amount. Since a pQCD calculation is not applicable for $\hat{\mathrm{P}}_{\mathrm{T}} \to 0$, a minimum cut-off value $\hat{\mathrm{P}}_{\mathrm{T}}^{\mathrm{min}}$ is applied. For Pythia6.1 it is 10 and 15 GeV and in case of Pythia6.4 it is 3 and 4 GeV, respectively. All the respective luminosity weightings have been taken into account. The kinematic range of the generated events extends for Pyhtia6.1 as $\mathrm{Q}^2 < 4.0$ GeV^2 and $0.001 < \mathrm{y} < 0.999$ whereas for Pythia6.4 they are slightly different $\mathrm{Q}^2 < 6.0$ GeV^2 and $0.01 < \mathrm{y} < 0.99$. The direct and resolved photon components for version Pythia6.1 were generated separately. This version includes charm (c) and light quark flavors u, d, s. Pythia6.4 is generated with direct and resolved processes in one go having c, b, u, d, s quark flavors included. All distributions containing the legend Pythia1 are related to Pythia version 6.4 and the ones with Pythia2 are the

alias of Pythia version 6.1

4.2.3 Herwig

Herwig [CKM$^+$01] is a general purpose MC event generator, which includes among others the simulation of hard lepton-hadron scattering. It uses the parton-shower approach for initial and final state QCD radiation, involving color coherence effects and azimuthal correlations both within and between jets. The major difference to Pythia is the hadronization model. Herwig uses the cluster hadronization algorithm. In this approach, after the perturbative stage of parton generation, all final gluons are split non-perturbatively into essentially light (u and d) quark and antiquark pairs. Such $q\bar{q}$ (diquark [Bou95]) pairs are combined into colorless cluster. Heavy clusters can be divided into two light clusters first. Afterwards all clusters decay into hadrons.

The Herwig generator was used in the scope of this analysis for the estimation of model uncertainties. The version used is Herwig6.4 with direct and resolved contributions of the subprocesses with generated u, d, s, c quark flavors. The soft underlying events were applied to 35% of the resolved γp interactions. The leading order parametrisations CTEQ5L for the proton PDF and GRV-GLO [GRV92] for the photon PDF were used in Herwig. Following kinematic selection was applied $Q^2 < 4.0$ GeV^2 and $0.001 < y < 0.999$ as well as $\hat{P}_T < 13.0$ GeV for generation.

4.3 Generation of Background Events

The Rapgap [Jun95] and Djangoh [CSS94] event generators were used to model the background from low Q^2 DIS events and to study the effect on the selected data sample. The Rapgap event generator was used as a main source of background events for this analysis. The Djangoh event generator was used to determine the systematic uncertainties coming from DIS background sample, of course by distinguishing the measured cross sections due to differences in the obtained corrections from Rapgap and Djangoh. The effect of both MCs on NC DIS low Q^2 analysis, using the jet selection applied for current analysis, was investigated and reweights on both MCs were applied in order to mimic the data sample.

4.3.1 Rapgap

Similar to Pythia Rapgap uses leading order matrix elements matched with DGLAP parton showers for the simulation of DIS events and the hadronization is performed using the Lund string model as given by the JETSET MC program. The leading order parametrisations CTEQ6L for the proton PDF and SAS 2D for the photon PDF were used in Rapgap. The generator version Rapgap3.1 was used to determine the low Q^2 DIS background for $2 < Q^2 < 200$ GeV^2 and $0.01 < y < 0.9$ kinematic region.

4.3.2 Djangoh

The MC generator Djangoh describes the inclusive *ep* DIS interaction at leading order. The Parton Density Function (PDF) chosen to be for proton CTEQ6L and GRV94-LO for photon. It includes an implementation of the Color Dipole Model (CDM) in ARIADNE [Loe92]. There parton radiation is modeled through gluon emission from color dipoles. The kinematic range was chosen same as for the Rapgap event generator: $2 < Q^2 < 200$ GeV^2 and $0.01 < y < 0.9$.

CHAPTER 5

DATA SELECTION AND CORRECTIONS

5.1 H1OO Framework

In the year 1998 the H1 group had decided to migrate from their analysis software framework based on Fortran to a new one in order to generalize the analysis purposes. Software packages were created and evolved which provided powerful and successful tool for physical analysis. In order to accomplish this, one had to [H107a]:

- provide a unique, modern, extendable and re-usable framework
- incorporate and support all H1 physics analysis
- standardize the physics algorithms (kinematic reconstruction, selection criteria, particle identification etc.)
- provide one unique code reference and thus facilitate exchange of information between different analysis groups
- make expert knowledge reusable by non-experts and lower the thresholds of starting a new analysis
- provide a faster, more efficient access to the data

The storage of the analysis objects and the software in H1 are based on the RooT[1] framework, which uses an object-oriented programming language C++ (The software is based on a set of H1OO classes written in C++). One writes a private code, compiles it to check for possible errors and finally runs the created program, or one uses a RooT command line interpreter, called CINT, for running macros interactively. This makes the necessary homogeneity and extendability of any analysis achievable and also provides efficient storage, analyzing and graphics display facilities [H107a].

[1] http://root.cern.ch/drupal

5.1.1 Three-Layer Data Storage

The data sample used in this analysis was collected with the H1 detector in the year 2006. Candidate events were selected by the H1 trigger system (see section 3.7) and were written on tape. The storage of the physics analysis data in the H1 framework is made in three layers. These three layers are physically written to different file streams. The relations between the different pieces of information for a given event are managed by the H1Tree class such as if they were one single TTree [H113,Roo13].

The first layer contains the Data Summary Tape (DST) files representing the outcome of the H1 reconstruction software H1Rec [H108], which includes improved (DST7) wire hits, channel numbers and cell energies information as well as an alignment of the tracking detectors and thus track and vertex identification. They are written in FPACK format [H191] and include the information on properties of every object in an event stored in BOS banks [H188]. The so-called Object Data Store (ODS) based on RooT is a one-to-one equivalent of the DST information[2], but in object format and in principle could already be used as a basis for physics analysis. Nevertheless, one cannot expect fast data processing over such a huge amount of information as hundreds of millions of events. To solve this issue two additional layers, created from ODS, have been introduced, one is Micro Object Data Store (MODS), which contains particle-level information reconstructed from clusters and tracks and another one is H1 Analysis Tag (HAT), which contains event-level information like kinematic variables, particle multiplicities, energy sums in different parts of the detector, etc. Both levels are significantly smaller in size than ODS, yielding $\sim$ 3.0 kB/event for MODS and $\sim$ 0.4 kB/event for HAT, respectively [H107b].

One still faces the issue of a large amount of data to run through. To solve this problem one makes a so-called preselection of data by applying an analysis related selection, producing from MODS and HAT the preselected RooT files. Selection is often referred to as a *cut* on a variable, for instance, if one wants to cut off events with Q^2 greater or equal to 4.0 GeV^2 than one demands a cut $Q^2 < 4.0$. One of the key points of H1Tree are selections. As an example, selection on HAT level[3] is an arbitrary logical combination of arithmetic expressions applied on variables stored in this data layer. If one wants to select events with at least two jets and reject the events with the transverse momentum of the first jet less than 10.0 GeV the selection string might look like this:

$$\text{fNumInclKtJets} > 1 \;\&\&\; \text{fInclKtJetFwdPt1} > 10.0$$

Such a selection technique was used in this analysis to perform the preselection of data.

[2]This requirement allows backward conversion from ODS to DST without information loss.
[3]The description of all variables stored on HAT level one finds in H1HatEvent class [H109].

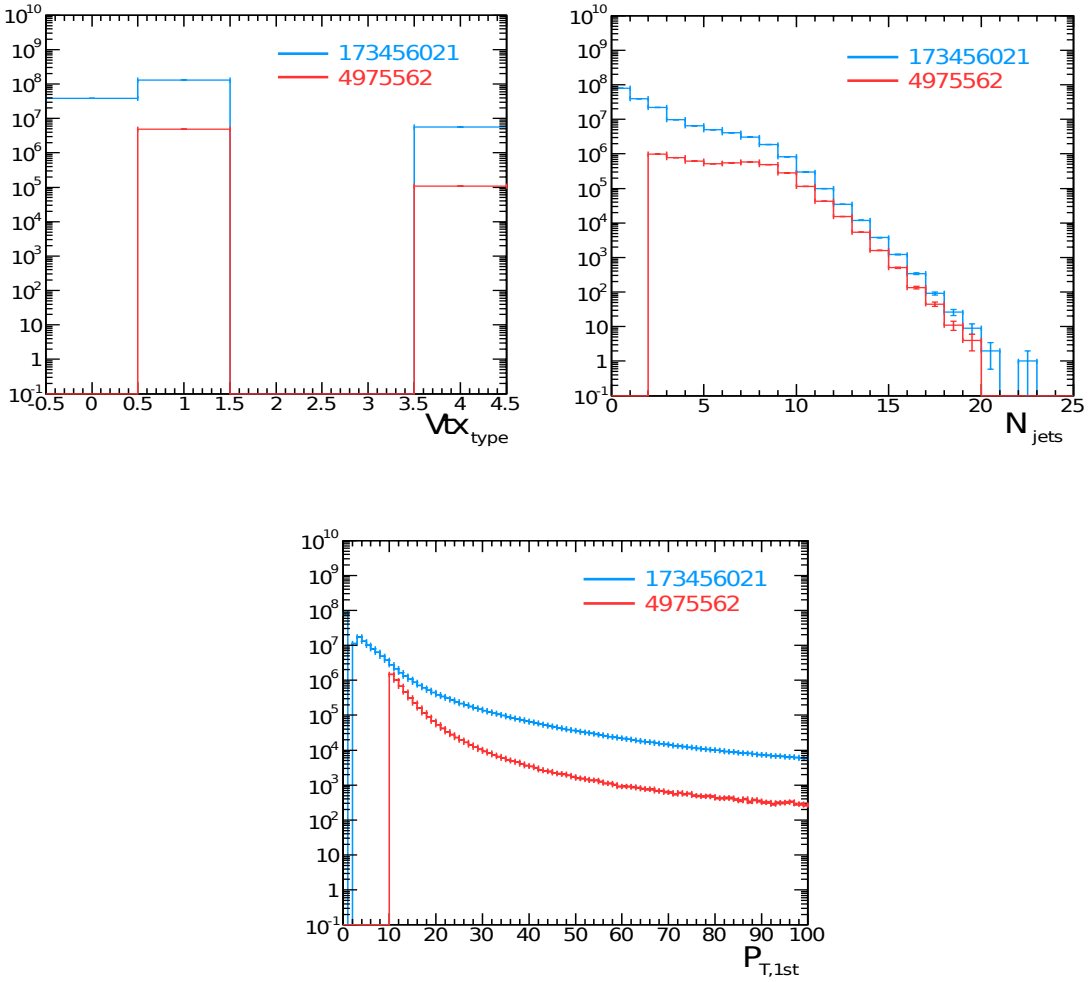

Figure 5.1: Preselection variables. The blue and red line describe the distributions of the variables before and after the preselection.

5.2 Data Preselection

In order to reduce the running time used for the processing of a large amount of recorded data a preselection of events was foreseen for this analysis. It is made on HAT level variables, which gives a reasonably fast selection, since only a few data are read in from the RooT files. The MODS level selection takes longer because the program first has to read in the complete variables information and only afterwards the selection is performed. That was the reason to discard the MODS level at this step of the analysis. Events that pass the selection on HAT level are stored into new RooT files which will be used for further selections and analyzing.

In this analysis only three HAT level variables are used for the preselection. The requirements on them are shown in table 5.1. A reconstructed central vertex or a forward vertex is required to reduce background events. The number of jets in the event has to be larger than one, and the jet with the highest transverse momentum must have $P_{T,1st} > 10$ GeV. Figure 5.1 shows the effect of these selections. In blue

Preselection on HAT
$\mathrm{Vtx}_{\mathrm{type}} = 1$ or $\mathrm{Vtx}_{\mathrm{type}} = 4$
#jets > 1
$\mathrm{P}_{\mathrm{T,1st}} > 10$ GeV

Table 5.1: Preselection cuts used in analysis. This is HAT level information only.

is shown the total number of events recorded by H1 for the year 2006, e^+p period. In red is displayed the number of events after the preselection. The corresponding amount of events to process is reduced from $\sim$ 173.5 million events to $\sim$ 5 million events. For this preselection the $\mathrm{P}_{\mathrm{T,1st}}$ cut on the jets is done without having yet performed the Hadronic Final State (HFS) energy calibration, which will be discussed later in section 5.3.2.

Since the HAT information on the second highest jet transverse momentum $\mathrm{P}_{\mathrm{T,2nd}}$ is also available, it is also possible to impose an additional cut on it. Unfortunately, one faces the issue of discarding some events, which would fulfill the final analysis requirements, if one applies the cut on the second highest jet transverse momentum. This feature was found by running the analysis over the full 2006 e^+p data without preselection but with all the final selection cuts (see section 5.8). The HAT level distributions of the highest and second highest jet transverse momenta $\mathrm{P}_{\mathrm{T,1st}}$ and $\mathrm{P}_{\mathrm{T,2nd}}$ provide a good reason to cut only on the highest jet transverse momentum $\mathrm{P}_{\mathrm{T,1st}}$, and that the requirement should be $\mathrm{P}_{\mathrm{T,1st}} > 10.0$ GeV (figure 5.2). In this case one is on the safe side of not discarding any events which would fulfill the final selection cuts.

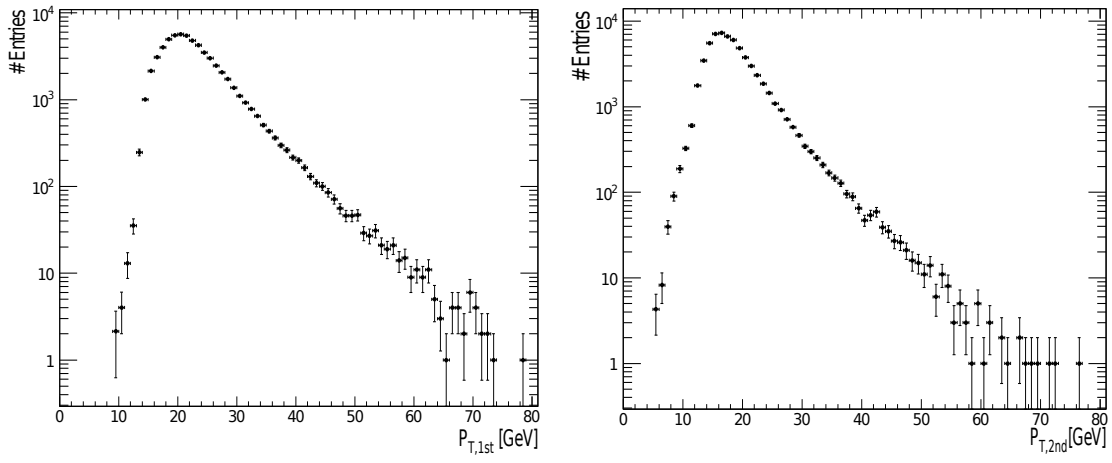

Figure 5.2: HAT level variables after the final selection discussed in section 5.8 are shown. 2006 e^+p data are shown without any preselection applied. Preselection of the $\mathrm{P}_{\mathrm{T,2nd}}$ jet variable may cut off some of the useful events.

5.3 Hadronic Final State Calibration

The HFS is defined by all identified detector level particles (with the exception of isolated electrons) obtained by the hadronic reconstruction algorithm in H1OO 2 HADROO2. Since the measurement of jets requires an accurate determination of the energies of the hadronic final state particles, which were identified in the tracking detectors or in the LAr or the SpaCal calorimeters, it is important to precisely calibrate the HFS energies, using the information either from the particle's track momentum or the cluster energy deposit. Improved in the year 2010, the HADROO2 algorithm defines the HFS objects, and the subsequent calibration technique delivered the constants for precise energy definitions of the HFS which are used for the production of DST7 files.

5.3.1 Hadronic Reconstruction in H1OO

For the definition of the HFS the HADROO2 algorithm is applied. This energy flow algorithm uses particle momenta information from tracks and from calorimeter energy deposits to decide which information is more precise and how best to use it. Depending on the uncertainty of the measurement of the track and the cluster energy deposit it is decided which of the two measurements is used for the reconstruction of an HFS object.

Tracks The tracks involved are "*good quality*" tracks, the so-called "*Lee West*" tracks [H100]. Measured with the Central Track Detector (CTD) and the Forward Track Detector (FTD) these tracks are classified into three categories, central, combined and forward tracks, according to the quality cuts described in [H105]. Tracks from primary and secondary vertices can be chosen, but precedence is given to primary ones, and the information on these selected tracks is taken as one input for the HADROO2 algorithm.

Clusters The cluster positions are corrected for alignment using the run-dependent parameters[4]. Calorimeter clusters originate from energy depositions in the LAr or SpaCal calorimeters. For the same incident energy in the LAr calorimeter a higher response to electrons is observed on average than compared to that of the hadrons, as expected. In order to correct for that, a weighting technique within H1Rec was introduced [H194b]. A particle is accepted as an electromagnetic object if $\geqslant 95\%$ of its energy deposits is in the electromagnetic section of the calorimeter, where 50% of its energy must be in the first two layers of the calorimeter. One should also keep in mind that the occurrence of negative energy cells, which may be neighboring cells to cells with positive energy, are taken as a part of the cluster and thus invalidate a systematic positive bias in the energy measurement. A set of noise suppression algorithms, acting symmetrically with respect to negative and positive energy deposits, are applied in order to remove electronic and background noise. The cluster's 4-vector is calculated by summation of the respective cell 4-vectors.

[4]During the runtime pauses the detector was under maintenance and some parts of it were exchanged. Also cooling down the calorimeter to its working temperature of 72 K produced its shrinkage [Kog10]. These factors required the correction for misalignment of the tracking system and calorimeter to nominal positioning values.

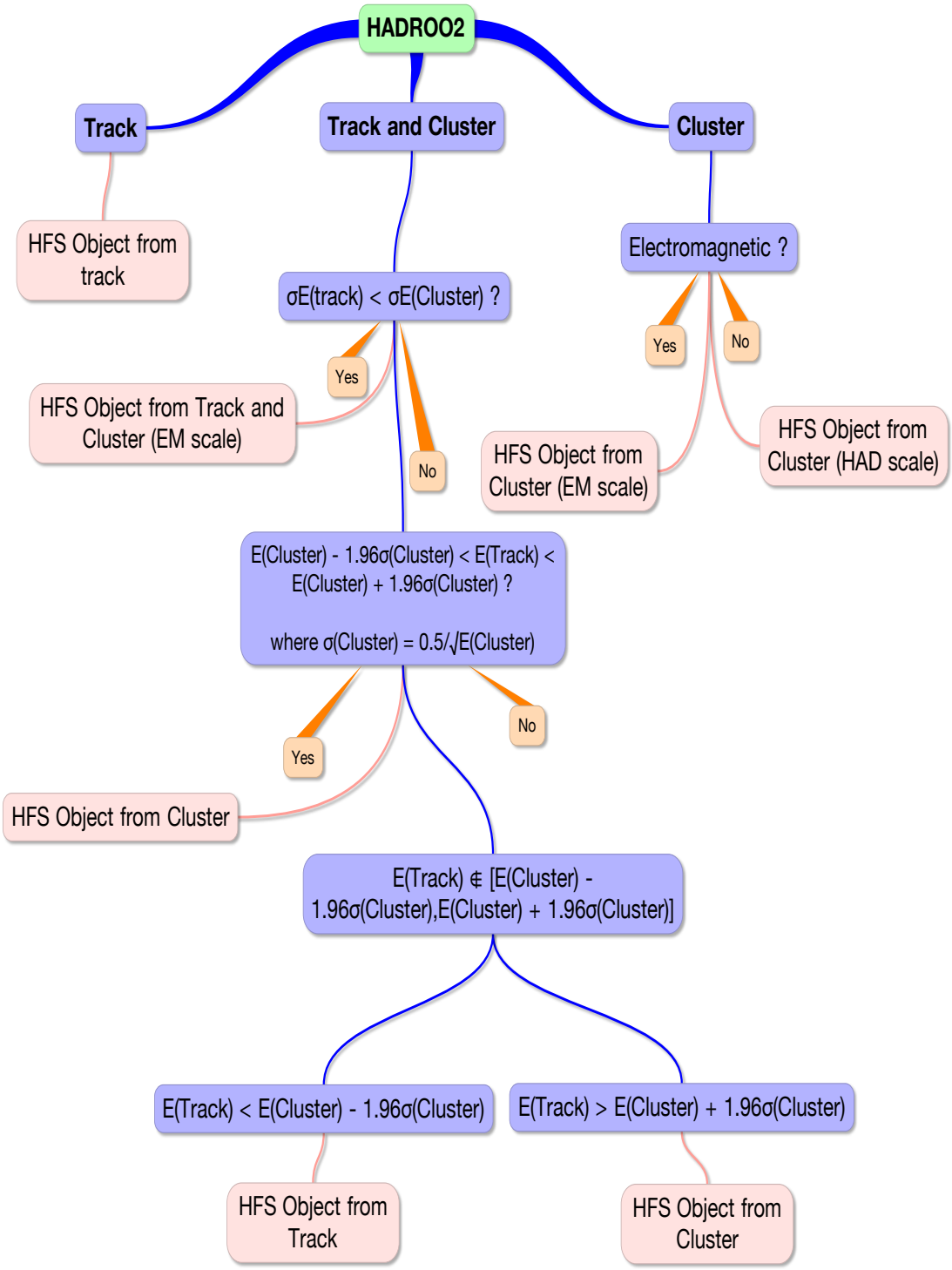

Figure 5.3: Schematic interpretation of the HADROO2 algorithm.

A schematic interpretation of the HADROO2 algorithm is shown in figure 5.3. The idea behind it is to first extrapolate the tracks to the calorimeter clusters to which they are associated, then:

- The tracks without paired clusters are taken as the tracks of charged particles which produce no shower, and they are taken as part of the HFS.

- The clusters without associated tracks are considered to originate from neutral particles (γs, neutral hadrons), which deposit energy impacts into the hadronic part of the calorimeter.

- The track is pointing to a cluster. The trajectory of a track inside the calorimeter is continued as a straight line, and if its length is less than 25 cm, and it intersects with the barycenter of a cluster, then one assumes the cluster and track originate from the same particle. If the error of the track energy measurement is smaller than the one from the cluster

$$\left(\frac{\sigma(\mathrm{E})}{\mathrm{E}}\right)_{\mathrm{Track}} < \left(\frac{\sigma(\mathrm{E})}{\mathrm{E}}\right)_{\mathrm{Cluster}} \tag{5.1}$$

  then, using the pion mass hypothesis for the measured track, the energy of the particle will be reconstructed from the track, and the energy deposited in the calorimeter is set to zero to avoid double counting of the energy. However, the cluster energy is set to zero only, if the equation 5.2 is true:

$$\mathrm{E}_{\mathrm{Cluster}} < \mathrm{E}_{\mathrm{Track}} \left(1 + 1.96\sqrt{\left(\frac{\sigma(\mathrm{E})}{\mathrm{E}}\right)^2_{\mathrm{Track}} + \left(\frac{\sigma(\mathrm{E})}{\mathrm{E}}\right)^2_{\mathrm{Cluster}}}\right), \tag{5.2}$$

  where the possible fluctuations of both measurements are taken into account. If equation 5.2 is false, the excess energy of the cluster is from a neutral particle or another track. The $\mathrm{E}_{\mathrm{Track}}$ is than subtracted from $\mathrm{E}_{\mathrm{Cluster}}$ and the remaining energy is used further on in the algorithm.

- If the equation 5.1 is false, i.e. $\mathrm{E}_{\mathrm{Track}} \pm \sigma_{\mathrm{E}_{\mathrm{Track}}}$ is greater than $\mathrm{E}_{\mathrm{Cluster}} \pm \sigma_{\mathrm{E}_{\mathrm{Cluster}}}$, where $\sigma_{\mathrm{E}_{\mathrm{Cluster}}} = 0.5/\sqrt{\mathrm{E}_{\mathrm{Cluster}}}$, then:

  - The condition $\mathrm{E}_{\mathrm{Cluster}} - 1.96\ \sigma_{\mathrm{Cluster}} < \mathrm{E}_{\mathrm{Track}} < \mathrm{E}_{\mathrm{Cluster}} + 1.96\ \sigma_{\mathrm{Cluster}}$ is compared, and if it is fulfilled then the track is removed, and the energy of the cluster is used.

  - If $\mathrm{E}_{\mathrm{Track}} > \mathrm{E}_{\mathrm{Cluster}} + 1.96\ \sigma_{\mathrm{Cluster}}$ then the track is suppressed, and a particle is declared to be a part of HFS using the calorimetric cluster.

  - Finally, if $\mathrm{E}_{\mathrm{Track}} < \mathrm{E}_{\mathrm{Cluster}} - 1.96\ \sigma_{\mathrm{Cluster}}$ then the track measurement is used and the cluster energy is subtracted [H105].

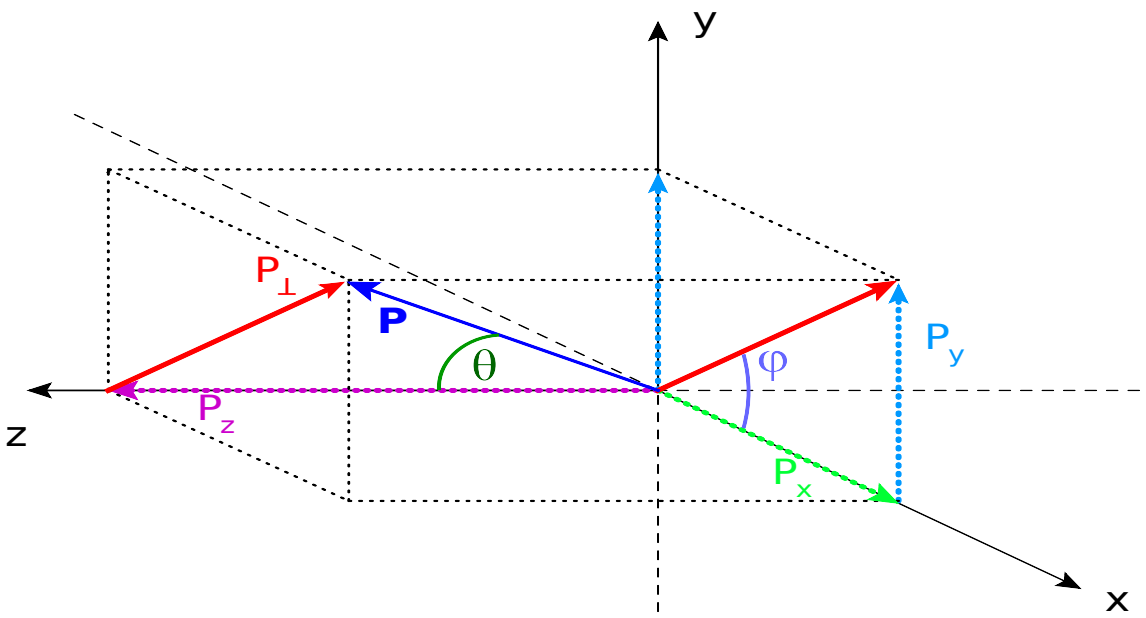

Figure 5.4: Depiction of transverse momentum $P_\perp$ of a single particle, which builds up a part of the jet's transverse momentum.

5.3.2 Calibration

After the selection criteria, explained in section 5.3.1, the charged and neutral particles are assigned by the HADROO2 algorithm as hadrons. A collimated bunch of these particles is defined as a jet. A jet contains an amount of particles energy which cannot be measured in calorimeter. The conversion efficiency of energy into a measurable signal is e for the electromagnetic part and h for the hadronic part ("non-compensation", see equation 3.1). For the electromagnetic part a measurable signal is almost completely generated, whereas for a large amount of energy in the hadronic part it remains undetectable. This undetectable energy is referred to as an invisible energy, and it is related to processes where energies get absorbed in the passive medium (recoil of nuclei, nuclear binding, evaporation neutrons [GS08]). Hence, the measured energy is smaller than the actual energy carried by the hadrons, and as a consequence the energy of jets should be corrected.

In the ep collisions, for the events with a single jet in a final state, the transverse momentum of the scattered electron P_T^e balances the jet P_T^{jet}. P_T^{jet} is the transverse momentum of the whole HFS system, which can be written in a different form P_T^h and is defined by:

$$P_T^h = \sqrt{\left(\sum_h P_X^h\right)^2 + \left(\sum_h P_Y^h\right)^2}, \tag{5.3}$$

where the sum runs over all hadrons which build the jet. The depiction of the transverse momentum of a single particle, which builds up a jet, is shown in figure 5.4.

A few points are worth to be mentioned [Kog10]:

- The selected tracks entering the HFS are well measured, and the calibration

procedure must not affect their energies.

- Before applying the calibration the hadronic energy scale is known within $4-5\%$.
- The jet calibration is made using the NC DIS sample selecting only one jet events.
- The calibration procedure must be insensitive to the absolute energy scale of the HFS. It is mandatory that no cuts should be applied on variables depending on the HFS measurement in order not to bias the calibration.

The calibration procedure makes use of a double angle method which is independent of the absolute energy scale. The method employs the scattered electron angle θ_e and the inclusive hadronic polar angle θ_h. The total transverse momentum P_T^{da} is defined by:

$$P_T^{da} = \frac{2E_0^e}{\tan\frac{\theta_e}{2} + \tan\frac{\theta_h}{2}}, \tag{5.4}$$

where E_0^e is the energy of incident electron. Since this method is insensitive to the absolute energy scales, it allows the usage of P_T^{da} as a reference, if conditions due to Quantum Electrodynamics (QED) Initial State Radiation (ISR) and Final State Radiation (FSR) photons and leakage losses can be eliminated introducing the good P_T^{da} measurement cuts. For the definition of cuts and $\tan\frac{\theta_e}{2}$, $\tan\frac{\theta_h}{2}$ see [H199a, Kog10]. For events satisfying the above criteria and after the application of a correction factor to P_T^{da} as described in [Kog10] the agreement of P_T^{da} with P_T^{gen}, where P_T^{gen} is the transverse momentum of the generated HFS in simulated events, is in most part of theta θ_{jet} range within 0.5%. The calibration check is made using the balance between the hadronic and double angle methods for data and MC:

$$P_T^{bal} = \frac{P_T^h}{P_T^{da}} \tag{5.5}$$

A minimization procedure is used to determine the parameters of calibration functions for electromagnetic and hadronic clusters within and outside of the jet, which results in an agreement between data and MC within 1% [Kog10]. Therefore, the hadronic energy scale is varied by $\pm 1\%$ to later determine the systematic uncertainty of the jet cross section measurement due to this source.

5.4 Run Selection and Luminosity Calculation

A time interval during which data events were recorded is called a *run*, it is a period with stable experimental conditions, which typically continue for more than two hours and for which the integrated luminosity is determined. Runs are classified as "good", "medium" or "poor", depending on beam, background and readout conditions as well as overall detector performance specific for a particular analysis. For this analysis the conditions of good and medium run qualities with a minimal integrated

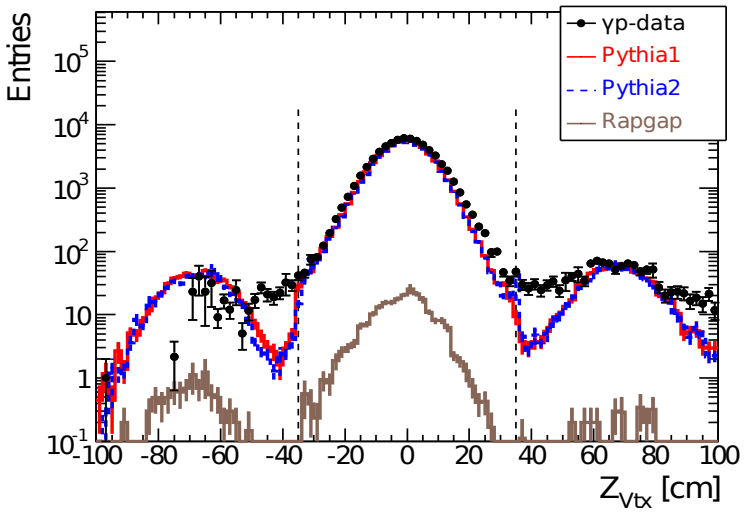

Figure 5.5: Distribution of the Z-position of the primary event vertex. Peaks of the satellite bunches can be seen at around ±70 cm.

luminosity of 0.2 nb^{-1}/run have been selected, yielding for the 2006 e^+p period an integrated luminosity of $\approx$ 92.4 pb^{-1}. The following subdetectors had to be included into the readout: the CJC1 and CJC2, the LAr calorimeter, the ToF and luminosity systems, the calorimeter trigger, the CIP, the VETOWALL and the SpaCal calorimeter. See chapter 3 for more information on these detector parts. A full run was rejected, if any of the above subdetectors had not been operating for a significantly long time interval within this run. If in an event any of the subdetectors was temporarily switched off than this event was not taken for further analysis. A requirement on the vertex position (equation 5.6) discussed in the following section is also included in the calculation of luminosity.

5.5 Selection of γp Events

5.5.1 Event Vertex

An accurate determination of the primary vertex of the interaction allows for a better measurement of the kinematic quantities and modeling of the detector acceptance. The beams accelerated within HERA have the characteristic spread of particle bunches. The proton bunch has a longitudinal extension of $\sigma_Z(p) \approx 11$ cm while the electron bunch is shorter, $\sigma_Z(e) \approx 2$ cm. To take into account varying shifts in the mean position and length of the interaction region of the beams one demands that an event vertex is reconstructed within ±35.0 cm of the nominal Z-position of vertex.

$$-35.0 \text{ cm} < Z_{Vtx} < 35.0 \text{ cm}. \tag{5.6}$$

This cut substantially reduces the background events coming from interactions of the proton beam with the residual gas or with the beam pipe walls.

Before the colliding beams are brought to their respective nominal energies, they pass

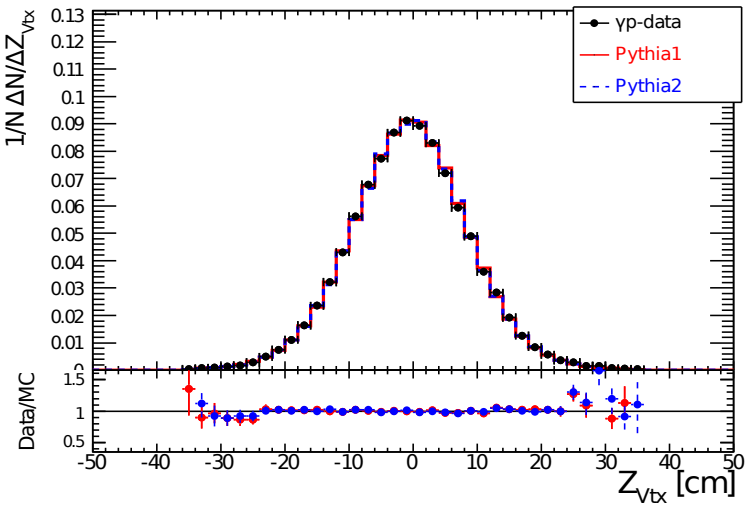

Figure 5.6: Shape normalized distribution of the Z-position of the primary vertex. A very good agreement is obtained after reweighting (see section 5.11) of the simulated MC events.

long injection and pre-accelerating step. One of these steps is a bunch length compression, which is necessary to decrease the longitudinal size of the proton bunches to the design value mentioned above ($\approx$ 11 cm). Unfortunately, as a side effect, some small fraction of the proton current escapes from the main bunches and forms parasitic non-Gaussian proton-beam tails – satellite bunches [H195b]. Figure 5.5 shows accompanying satellites which are as well suppressed by the event vertex cut. The black bullets correspond to the analyzing γp data sample, the solid red line and a dashed blue line correspond to two Pythia models described in 4.2.2 and brown line corresponds to the Rapgap background MC model described in 4.3.1.

After each beam filling at HERA, the orbits of the beams are optimized to gain more luminosity. That implies that the true interaction region varies from run to run. To mimic this effect the mean and standard deviation of the position of the primary vertex are identified and applied within the MC simulation. There is a small residual shift between data and MC observed. This shift is corrected by applying a weight scheme to the MC events [Shu11] which leads to an excellent agreement between data and MC, as is seen in figure 5.6. This distribution is shown after the final selection, which is discussed later on in section 5.8. The black bullets correspond to the γp events, from which the background MC sample was already subtracted.

5.5.2 γp Events with $Q^2 < 4$ GeV^2

Scattered Electron Rejection

As it was already discussed in section 2.3 the photoproduction domain corresponds to the region of $Q^2 \sim 0$ GeV^2. These are exactly the events where no scattered electron is identified and it flies straight into the beam-pipe. Nonetheless there are events where scattered electron hits the regions of SpaCal close to the beam-pipe and because of the limited geometrical acceptance of SpaCal the efficiency to measure scattered electron below $Q^2 = 4.0$ GeV^2 vanishes fast with decreasing Q^2. Due to

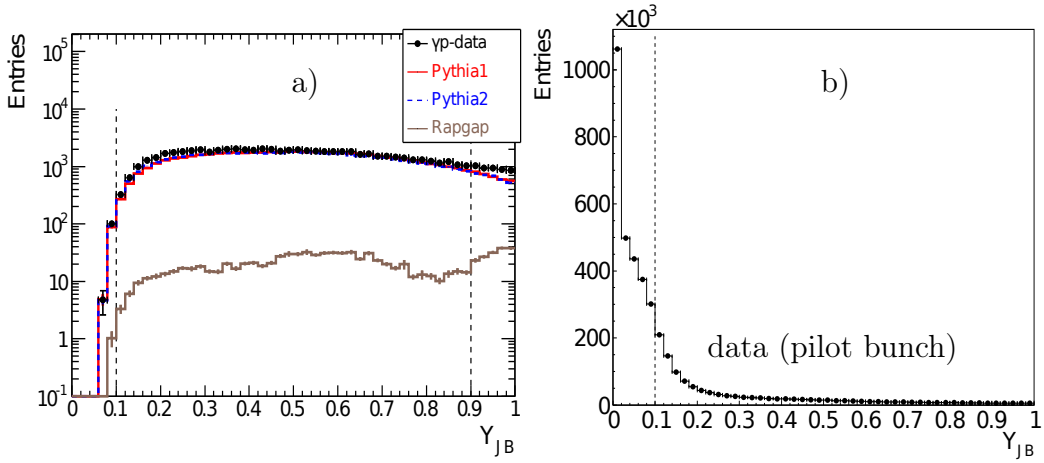

Figure 5.7: Distribution of y_{JB} after the final selection (see section 5.8) except of the cut in $0.1 < y_{JB} < 0.9$ which corresponds to the vertical dashed lines (a). Figure (b) shows the data events corresponding to the proton pilot bunches.

this fact the cut for the rejection of the scattered electron was extended to:

- take event, if no scattered electron was found, or
- take event, if scattered electron was found and its $Q_e^2 < 4.0$ GeV^2.

All events not fulfilling the above conditions are removed from further analysis. As long as the efficiency for the identification of the scattered electron is not 100% a fraction of DIS background events is remaining among the γp events.

E-P_z and y_{JB} Selection

The unidentified scattered electron is treated as an HFS particle leading to wrongly calculated observables. In order to fight this an additional variable on the total hadronic $(E - P_z)_h$ was required, which is defined as:

$$(E - P_z)_h = \sum_i E_i - P_{z,i}, \tag{5.7}$$

where the index i runs over all HFS particles. In the massless approach of incoming electron and proton, it can be easily calculated, using the energy and momentum conservation, that $(E - P_z)_h + (E - P_z)_e$ of the scattered electron should sum up to twice the incident electron beam energy, $2E_e$. Thus, for those events, were the scattered electron was mistakenly identified as a part of the HFS, $(E - P_z)_h$ is expected to be close to 55.2 GeV. That was also shown in [Car02]. A cut in $(E - P_z)_h$ at $0.9 \cdot 2E_e$ removes most of these DIS background events. Since y_{JB} [BJ79] and $(E - P_z)_h$ are related to each other via

$$y_{JB} = \frac{(E - P_z)_h}{(2E_e)}, \tag{5.8}$$

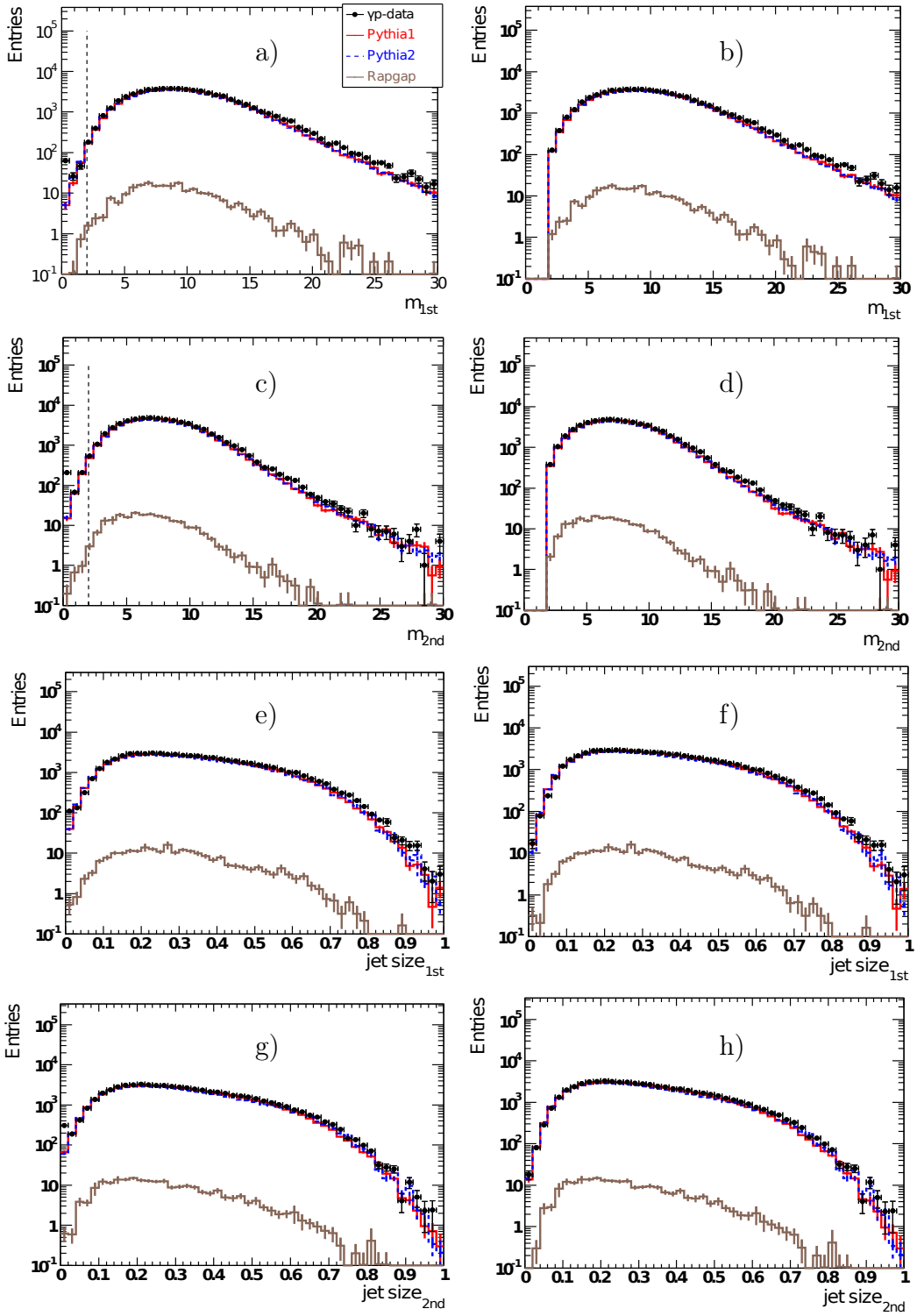

Figure 5.8: Data are compared to the MC events for the jet mass and jet size distributions of the leading and second leading jet. The left column corresponds to the events which passed all the final selection cuts, see section 5.8, but the cuts on jet mass and jet size. The left edge of each distribution of this column shows an inconsistency of data and signal MC. In the right column are shown events obtained after the application of the cuts on jet mass and jet size. A good description of the data by the signal MC is seen.

the cut $(E - P_z)_h < 0.9 \cdot 2E_e$ equals to the cut $y_{JB} < 0.9$, see figure 5.7a. The Jacquet−Blondel reconstruction method of the event kinematics is also known as a hadronic reconstruction method (see 2.2.1). In this method no information about the scattered electron is used, only the measurement of the hadronic final state enters.

Distribution of y_{JB} shown in figure 5.7a has a kinematic domain where for low values $y_{JB} < 0.1$ there is no enough resolving power from photon side to interact hardly in high P_T interaction. Moreover, the region of small y_{JB} is also the region of high x, which corresponds to hard scattering with the HFS at very small angles, making it difficult for a proper reconstruction. For a large fraction of background events due to beam-gas interactions, $(E - P_z)_h$ is expected to be small and therefore $y_{JB} \sim 0$. Figure 5.7b shows the proton pilot bunches of the whole 2006 e^+p data sample. A subsequent cut for $y_{JB} > 0.1$ was applied in order to reject this type of events. Hence, the cut $0.1 < y_{JB} < 0.9$ is used to define lower and upper boundaries for the visible phase space range for this analysis.

Jet Mass and Size Selection

The above cuts are not enough to get rid of a small source of background where the scattered electron fakes a high transverse momentum jet or is a part of one. The following jet observables were introduced in order to suppress this background:

- The invariant mass of a jet is defined as:

$$m_{jet} = \sqrt{\left(\sum_i p_i\right)^2}, \tag{5.9}$$

  where i runs over all particles which relate to the jet and p_i is the four-vector of particle i. Electrons which fake jets often have a very low profile of a jet mass which is not the case for hadronic jets. If one of the 2 leading jets has a jet mass below 2.0 GeV than the event is rejected, see figure 5.8 before (a, c) and after (b, d) the cuts (including the cuts described below).

- It can happen that the axis of one (or both) of the leading jets points into a ϕ-crack of the LAr calorimeter. In [Car02] it was shown that electrons scattered into these regions have a more pronounced structure in the region of small jet sizes. All events, where one of the leading jets enters the region of ± 2 degrees of a ϕ-crack in LAr and has a jet size smaller than 0.05, are rejected from further investigation. The distributions of the size of the first and second leading jet are shown in figure 5.8 before (e, g) and after (f, h) these and the above cuts. The jet size is defined as:

$$\text{jet size} = \frac{\sum_i E_i \cdot \sqrt{(\Delta\phi(\text{jet} - i))^2 + (\Delta\eta(\text{jet} - i))^2}}{E_{jet}}. \tag{5.10}$$

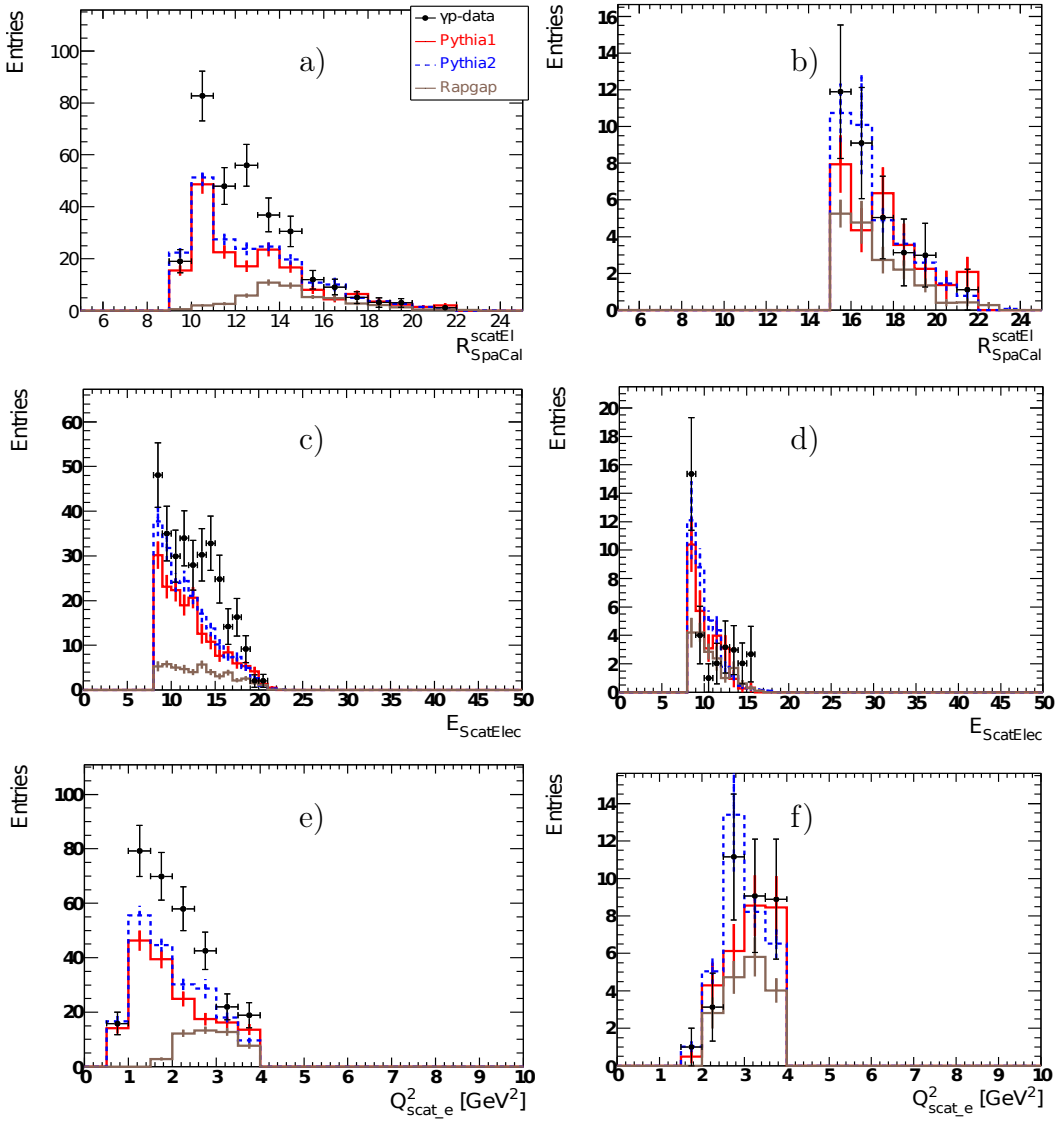

Figure 5.9: Distributions of scattered electron variables before the SpaCal radius cut $(\mathrm{a}, \mathrm{c}, \mathrm{e})$ and after the cut was applied $(\mathrm{b}, \mathrm{d}, \mathrm{f})$. Note that after the cut the y-axis scale of each distribution has changed.

Scattered Electron SpaCal Radius Cut

The cuts on the scattered electron and its Q^2 were introduced in order to mimic the residual acceptance of events with $Q_e^2 < 4$ GeV^2. After investigation of the events which fulfill this condition, it was found that the data distributions of the SpaCal radius, the scattered electron energy E_e and Q_e^2 are not well described by the MCs, see figure 5.9 (a, c, e).

Requiring a radius for the SpaCal acceptance of $\geqslant 15.0$ cm leads to an improved correspondence of data and MC for these quantities, see figure 5.9 (b, d, f). Events with a scattered electron, its $Q_e^2 < 4$ GeV^2 and $R_{\text{SpaCal}}^{\text{scatEl}} < 15.0$ cm are removed from further analysis. The impact of this cut influences the jet cross sections on the per mil level, and therefore no uncertainty corrections will be applied.

Missing P_T Requirement

Events, where part of the total transverse momentum of the event is carried away by an undetected neutrino and thus not visible in the detector, are due to Charged Current (CC) DIS background events. For this events a large unbalanced transverse momentum of the final state is seen in the detector, see equation 5.11. This momentum is called $P_{T,\text{Miss}}$. Thus, such background events are rejected by demanding that $P_{T,\text{Miss}}$ is less than 25.0 GeV, see figure 5.10.

$$P_{T,\text{Miss}} = \sqrt{\sum_{\text{HFS}+e'} \left(P_x^2 + P_y^2\right)}. \tag{5.11}$$

where the sum runs over all the Hadronic Final State (HFS) particles plus the scattered electron in the event.

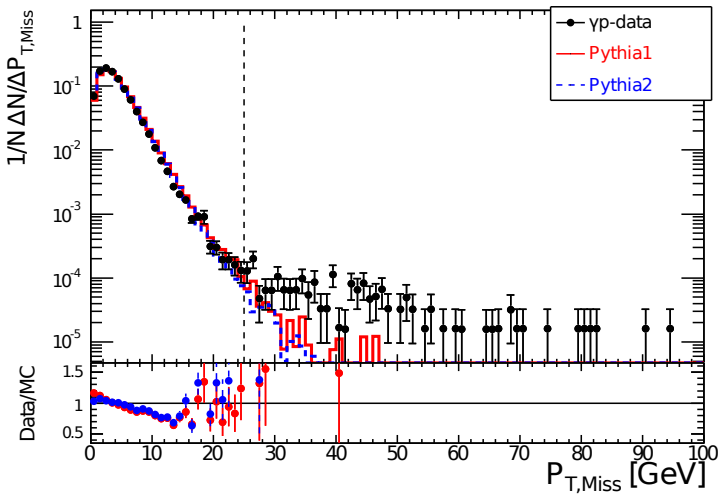

Figure 5.10: Missing transverse momentum of the events. The tail of the data is not described by both models for $P_{T,\text{Miss}} > 25.0$ GeV.

The Treatment of the Remaining DIS Background

The aforementioned DIS selections reduce the amount of the background drastically. Nonetheless, after these selections applied, some amount of the background events still remains in the sample. Running through the Rapgap (4.3.1) MC model, the amount of the remaining events can be estimated. The fractional amount of Rapgap (Djangoh, 4.3.2) compared to data events is 0.5% (0.4%). Further, they are statistically subtracted from data. For each shape normalized distribution, which reflects the comparison of data to MC, (i.e. figure 5.10) the black data bullets are presented with already subtracted DIS background events.

5.6 γp Events with High P_T Dijets

5.6.1 Selection and Ordering of High P_T Jets

As long as the HFS objects are defined, the jets can be selected simply by adding up the transverse energies $P_{T,i}$ of all HFS objects i belonging to the respective jet. For the purpose of finding jets one uses an algorithm (see section 2.5.1) with a reference frame applicable for the analysis. The reference frame used in this analysis is the laboratory frame. After the algorithm has found jets they are sorted and the output is stored in an array ordered in P_T. The jet with the highest transverse momentum is placed first, while a jet with the smallest P_T is in the last position of this array.

For this thesis photoproduction events with high transverse momenta dijets are considered. High P_T provides a natural hard scale to make perturbative QCD calculations possible. Contrary, at low P_T soft physics dominates the cross section, whereas the aim of the current analysis is to concentrate on hard processes.

Therefore, an event is kept for further investigation, if two jets satisfying the following requirements are found:

- Two leading jets in P_T are required with $P_{T,1st} > 15.0$ GeV and $P_{T,2nd} > 15.0$ GeV. The choice of a "symmetrical" cut is related to the application of a cut on the dijet invariant mass, see further section 5.6.2.

- The jets fulfilling the above P_T requirements must have pseudorapidities in the range of $-0.5 < \eta^{5}{}_{1st,2nd} < 2.5$. This restriction assures that jets are well contained in the LAr calorimeter, which has a geometric acceptance in the range of $-1.47 < \eta_{LAr} < 3.35$. The cut reduces migrations and helps to avoid a deterioration of the jet calibration in the forward direction. This can be characterized by the particle losses outside the acceptance of the calorimeter for extensive jets and also the dead material in front of the calorimeter. Also at small angles there may be particles that scattered from outside the acceptance into the acceptance. The lower bound on the jets η selection is chosen because of the poor measurement of hadronic jets in the SpaCal region. The SpaCal is located at lower values of pseudorapidity, where jets with size 1 in η can slightly overlap with the SpaCal acceptance although the jet-axis is still well inside the LAr calorimeter [Str04].

[5] For the definition of η see equation 2.39.

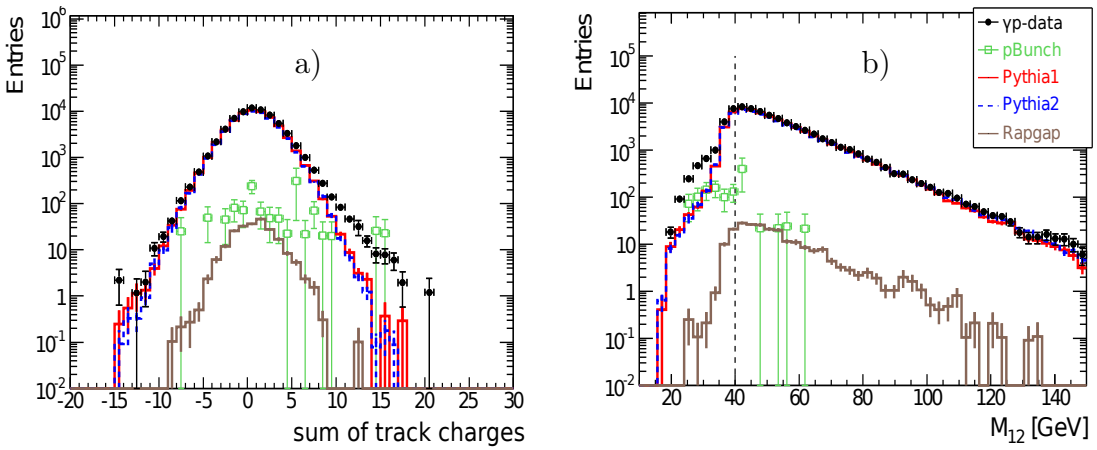

Figure 5.11: Distribution of the sum of track charges (a) and the dijet invariant mass (b). Both distributions are shown in green for the sample of proton pilot bunches.

The ordering of jets is a key concept of a detailed multi-jet analysis. Apart from P_T-ordering, the sorting of jets can also be performed in pseudorapidity in addition. The jets are classified according to the selection and comparison of the pseudorapidities of each pair of the two leading jets found in the event. The jet with the largest value of η is called the forward jet, and the one with the smaller η is called the backward jet. Shape normalized histograms in figure 5.27 show the jets P_T distributions of the dijets in P_T-ordered (a, b) and $\eta-$ordered (c, d) schemes.

In the following, the subscript "forw" and "back" refer to forward and backward jets with angular ordering. The labels "1st" and "2nd" refer to leading and subleading jets ordered in P_T. Quantities that are independent from any ordering like x_γ, x_P or mean values of P_T and η are obviously not affected by any of these ordering schemes.

5.6.2 Dijet Invariant Mass Cut

In a previous analysis the cuts on the two leading jets in P_T were "asymmetrical", i.e. $P_{T,1st} > 25.0$ GeV and $P_{T,2nd} > 15.0$ GeV [Str04]. This was made to avoid regions of phase space with the P_T of the two leading jets being identical or close to each other, where the existing NLO QCD calculations suffer from an incomplete cancellation of infrared singularities [H106, FR97]. In the current analysis one of the aims was to gain higher statistics in data and to reduce the size of the NLO correction in the calculation. For these reasons the selection of the transverse momentum of the leading jet was lowered to $P_{T,1st} > 20.0$ GeV. Unfortunately, this introduced more background in the analysis. The distribution of the sum of the track charges (figure 5.11a) gives a hint that the interactions of the proton beam with gas is one of the sources of this background. The sample of proton pilot bunches (see section 3.1) allowed to investigate events which interact with beam-gas.

Figure 5.11b shows the distribution of the invariant mass of the dijets system. One observes the contribution of the beam-gas events towards smaller values of the invariant mass together with a bad description of data by MC in that region. Therefore, a new selection cut is introduced into the analysis which removes all events for which

Phase space definition
$Q^2 < 4.0$ GeV^2
$0.1 < y < 0.9$
$P_{T,1st} > 15.0$ GeV
$P_{T,2nd} > 15.0$ GeV
$-0.5 < \eta_{1st/2nd} < 2.5$
$M_{12} > 40.0$ GeV

Table 5.2: Phase space definition of the measured dijets photoproduction cross section.

the invariant mass of the dijets is below 40.0 GeV. This cut also allows to reduce the minimum value of $P_{T,1st}$ even further in order to gain in statistics. A thorough investigation showed that demanding at least 15.0 GeV for both leading jets and the $M_{12} > 40$ GeV cut, balance each other in the same sense as the "asymmetric" P_T cuts which were made in a previous analysis – they insure convergence of fixed-order perturbative QCD calculations. Hence, the invariant mass cut as well as cuts in P_T and η of both leading jets define the visible phase space of this analysis. A summary of the analysis phase space definition is shown in table 5.2.

As one can see from figure 5.12, the description of data by MC after the selection in M_{12} is almost perfect. Still, some of the proton pilot bunches are contained in the main analysis sample and data are above MC in the tail of the positive sum of track charges. Further scanning of these events led to further reduction of beam-gas events.

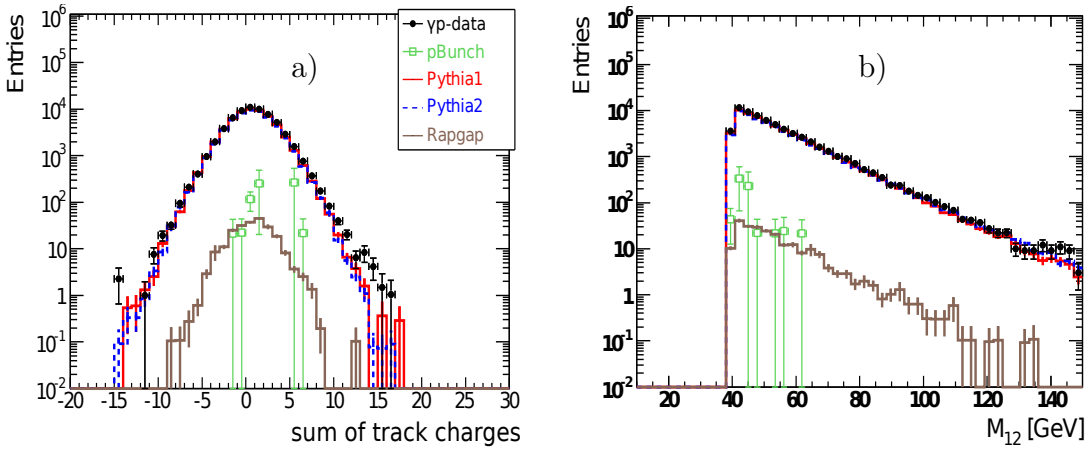

Figure 5.12: Distribution of the sum of track charges (a) and the dijet invariant mass (b) after application of the M_{12} selection.

Bit	Finder	Description
0	HALAR	Pure LAr "halo" longitudinal horizontal pattern
1	HAMULAR	Relaxed LAr "halo" pattern matching a deposit inside the Backward Iron Endcap
2	HAMUMU	Horizontal forward muon matching a deposit inside the Backward Iron Endcap
3	HASPALAR	Isolated inner forward LAr energy matching a deposit inside SpaCal
4	HAMUIF	Isolated inner forward LAr energy matching a deposit inside the Backward Iron Endcap
5	COSMUMU	Two opposite muon tracks of comparable direction
6	COSMULAR	LAr energy matching the direction of a muon tracks
7	COSTALAR	LAr energy matching the direction of two opposite Tail-Catcher clusters
8	COSTRACK	Two CJC tracks with directions exactly opposite in space
9	COSLAR	"Long" isolated LAr cluster with a small electromagnetic energy content

Table 5.3: Definition of ten topological non-*ep* background finders [H102].

5.7 Further Rejection of Background

In order to sort out the photoproduction events from the background ones further cuts have been applied to the analysis.

5.7.1 Non-*ep* Background Finders

The non-*ep* background finders were introduced into the H1OO framework in order to recognize and flag events containing particles which originate mainly from two sources:

- *cosmic muons*, coming from the highly energetic cosmic particles which hit the atmosphere of the planet, and
- *halo particles*, produced from interactions of the proton beam with the beam pipe wall or gas molecules in the beam pipe,

but not from the interactions of the electrons with the protons from the respective beams. Both sources are usually highly energetic and pass through the detector on a straight line. The *halo* signature is a long, almost horizontal line of energy deposits

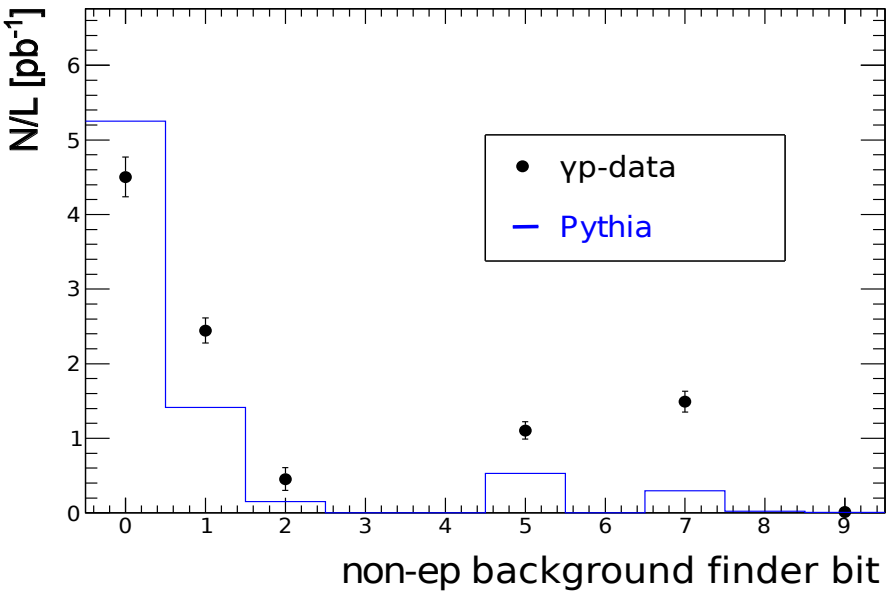

Figure 5.13: Background finder bits before any selection on them. Bits 0 to 4 correspond to halo finders, bits 5 to 9 are rejecting cosmic ray events.

in the LAr while for a *cosmic* muons two matching iron tracks on opposite sides of the instrumented iron or one iron track matched by energy deposits concentrated inside a long cylinder with small radius in the LAr provide a signature. In contrast to cosmic muons particles from p gas interactions are typically boosted in the forward direction, and it is less probable to find them in a back-to-back topology. The timing information is another useful tool to separate *ep* interactions from *halo* and *cosmic* ones by requiring the events to happen in coincidence with the crossings of the *ep* beam bunches. The *time window* introduced is suppressing about three quarters of the total non-*ep* background events [H102]. The classification of each of the non-*ep* background finder bits is shown in table 5.3. The first five bits from 0 to 4 are related to halo topologies and the bits from 5 to 9 to cosmic muon event topologies.

In figure 5.13 the description of the background finder bits after all the final selection cuts is shown. The veto was demanded on events, which were classified as background by pairs of finders with bit numbers 0 and 1, 5 and 6, 5 and 7, 6 and 7 and by the single bit 6. All the other bit numbers are of less importance as they do not contaminate the event sample. Every event rejected by any bit occurring singly or in combination was thoroughly scanned by means of the event display. This study revealed, that, using each of these bits in the selection as a single cut, discards also good photoproduction events which are of interest for the further analysis. Performing the background rejection by requiring pairs of bits as described above about 10 events per inverse picobarn are rejected as background in data and about 6 events in MC, which is about 1.5% and 1.0% of the total number of selected events for data and MC respectively. Compared with a total of $\approx$ 670 events/pb^{-1} for data and $\approx$ 630 events/pb^{-1} for MC in the final sample any uncertainty from this selection step is neglected (see section 6.4.7).

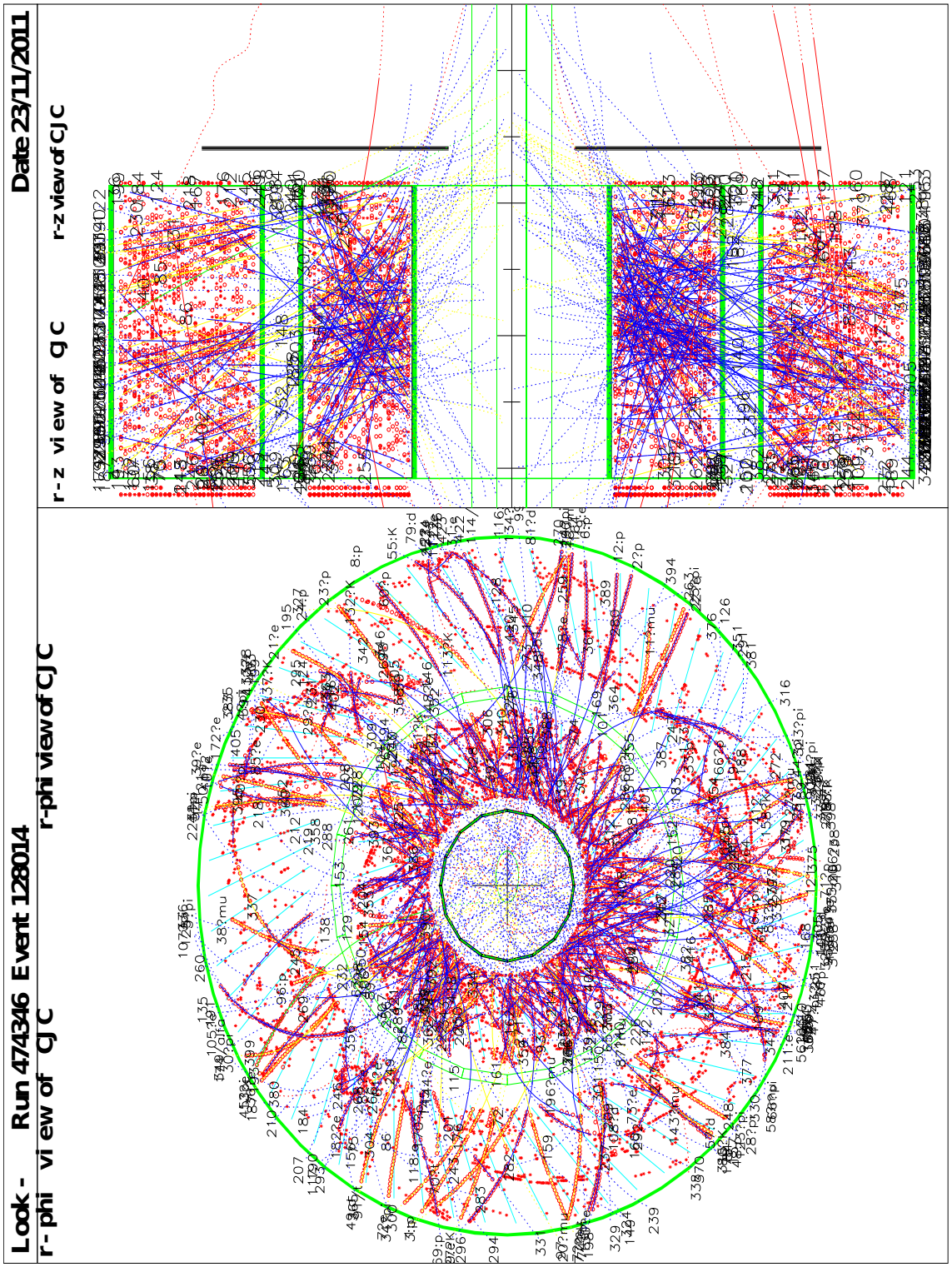

Figure 5.14: The CJCLOOK display at RAW/POT data level (GMCUT files). CJC1 and CJC2 are very busy with tracks pointing to many directions, which is well seen in the $r - \phi$ plane. The figure was provided by Claus Kleinwort.

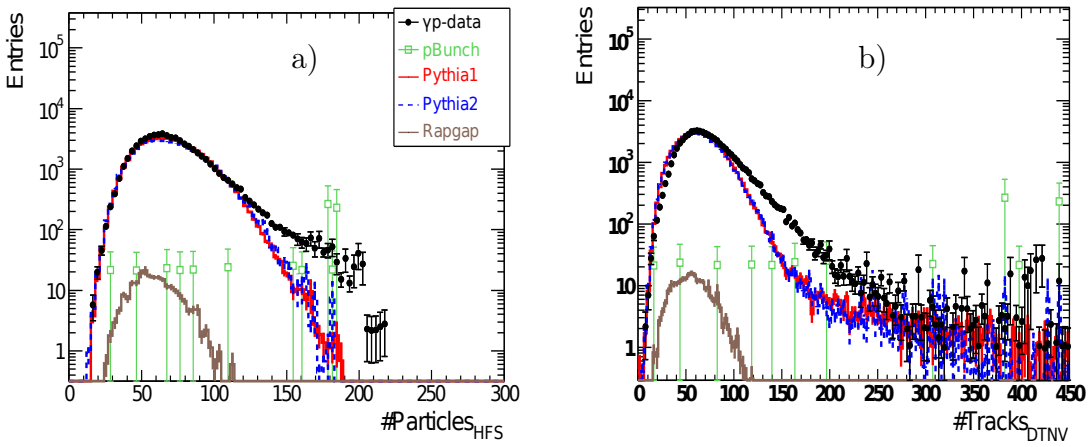

Figure 5.15: Distribution of the number of HFS particles (a) and the number of DTNV tracks in events (b).

5.7.2 Beam-Gas Selection

The distribution of the number of the HFS particles in events as well as the distribution of the number of non-vertex fitted tracks, also known as DTNV tracks, are both badly described in the regions above about 100 by the Pythia MC, see figure 5.15. The largest deviations between data and MC are seen for high multiplicity events. These events were scanned and a large number of LAr clusters as well as tracks were observed. The latter was supported by the huge amount of reconstructed tracks in the CJC (see 3.3.1), which point to many different vertices, some far away from the interaction region. A typical event is shown in figure 5.14. A feature of these events is that the track finding algorithm finds that the number of non-vertex-fitted tracks is as large as 450, the number of vertex-fitted ones is of the order $\sim$ 250, and after the Lee-West "good" track selection only $20 - 30$ tracks are fitted to the primary vertex. This gives a hint that some events coming from non-ep interactions are contaminating the photoproduction sample.

Tracks with a sufficient number of hits in the CJC (> 10) should have a small fake rate. The check for such "long" DTNV tracks should reveal the track timing, t0, distribution for ep interactions to peak at around 460 ticks ($\sim$ 500 ticks correspond to 1 bunch crossing) with an RMS of a few ticks. In figure 5.14 most tracks are not compatible with the triggered ep interaction. For these tracks t0 is not equal to 460 ticks indicating (overlays from) beam-gas interaction from satellite or different (than ep triggered) bunches. These can be also seen in figure 5.16a, where the track timing information is shown for the DTNV tracks which have more than 10 hits in the CJC tracker. As one observes, there are additional peaks at around 950 and 1450 ticks indicating that there are tracks from the interactions of the previous collisions, satellite bunches or beam-gas.

For a measurement of t0, tracks have to pass several wire (anode/cathode) planes. Due to the tilted wire planes this is, for long stiff tracks from the vertex, not a problem. Short tracks with large dca may have no t0 measurement. This is indicated in track timing figures by a spike at $t0 = 0$.

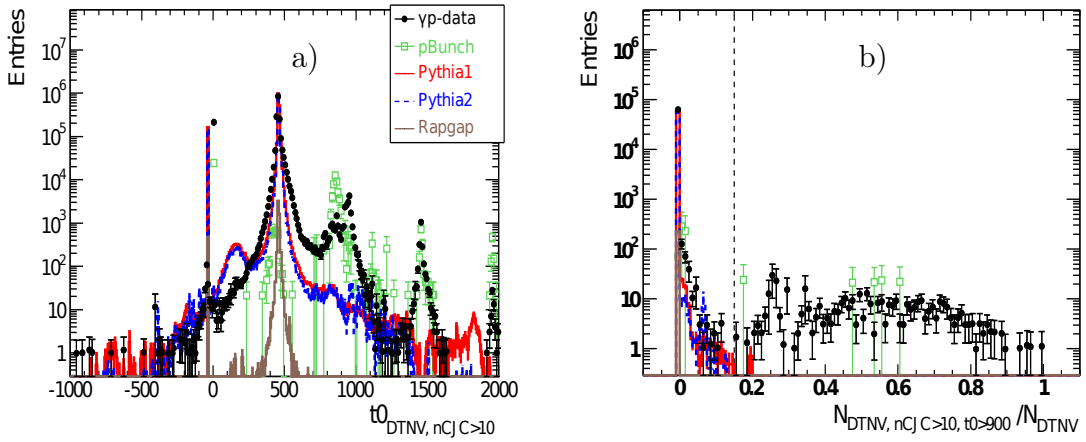

Figure 5.16: Distribution of the track timing t0 for those DTNV tracks which have more than 10 hits in CJC (a) and the ratio of the number of DTNV tracks with a number of CJC hits > 10 and track timing $t0 > 900$ to the number of all DTNV tracks (b).

The DTNV tracks timing distribution is a so-called "track-wise" distribution, which is not suited for the selection on an "event-wise" basis. For this reason a new variable was defined. It is the ratio of the number of DTNV tracks with CJC hits > 10 and $t0 > 900$ over the number of all DTNV tracks in the event, which is shown in figure 5.16b. This ratio gives a good distinguishing power against the background discussed. The following cut is implemented:

$$\frac{N_{\mathrm{DTNV,\ nCJC>10,\ t0>900}}}{N_{\mathrm{DTNV}}} < 0.15, \tag{5.12}$$

for events to be kept, which improves the t0 of the DTNV tracks drastically and rejects many of the events coming from non-*ep* interactions. The effect of this selection is shown in figure 5.17a.

Now, as one can see the events due to proton pilot bunches are still present in the sample. Further investigation led to another variable to cut on. This is the number of DTNV tracks with number of CJC hits > 20 and $|Z_0 - Z_{\mathrm{Vtx}}| > 20$, where Z_0 is the track's Z at dca[6]. The latter condition counts long tracks measured far from the reconstructed event vertex, Z_{Vtx}. Figure 5.17b shows the distribution of this variable with a subsequent selection indicated by the dashed vertical line at 27.0:

$$N_{\mathrm{DTNV,\ nCJC>20,\ |Z_0-Z_{Vtx}|>20}} < 27.0. \tag{5.13}$$

Further investigation of variables in the event has shown that the distribution of the vertex type number 1, which is the primary Z-vertex from the event taken from the H1 CJKV bank of vertices, is not defined for a small number of events. This is shown in figure 5.18a at the value -1. These type of events do not have any DTNV tracks in the CJC, they have more than 8000 CJC wire hits (on $\sim 2500/3000$ signal wires). In the CJC1 the hit density is apparently too large to find tracks.

[6]distance of closest approach

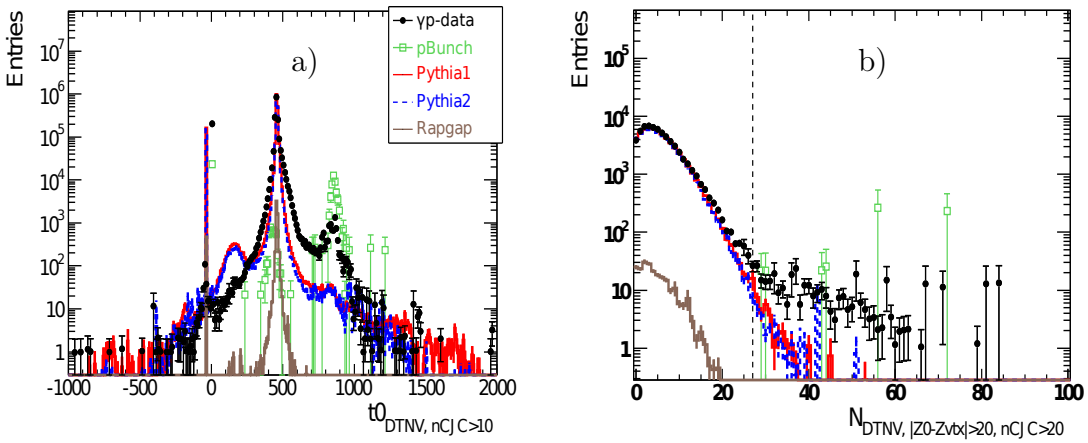

Figure 5.17: Distribution of the DTNV track timing t0 with number of CJC hits > 10 (a) and distribution of the number of DTNV tracks with the number of CJC hits > 20 and $|Z_0 - Z_{Vtx}| > 20$ after the ratio cut 5.12 (b).

It was found that the CJC reconstruction code has a cut in the number of CJC hits. For more than 8000 hits the full pattern recognition is not run and no tracks are vertex fitted. This is also seen in figure 5.19a. The privately modified reconstruction code with enlarged threshold, up to 12000, found vertex fitted tracks, which are, however, all out of time - not from the triggered bunch crossing, which can be seen in figure 5.19b. After scanning all these events they were all determined to be background and were removed from further analysis by rejecting events with a -1 vertex of type 1, see figure 5.18a. Figure 5.18b shows the track timing, t0, after all the cuts discussed in this subsection; no any proton pilot bunches event has been registered.

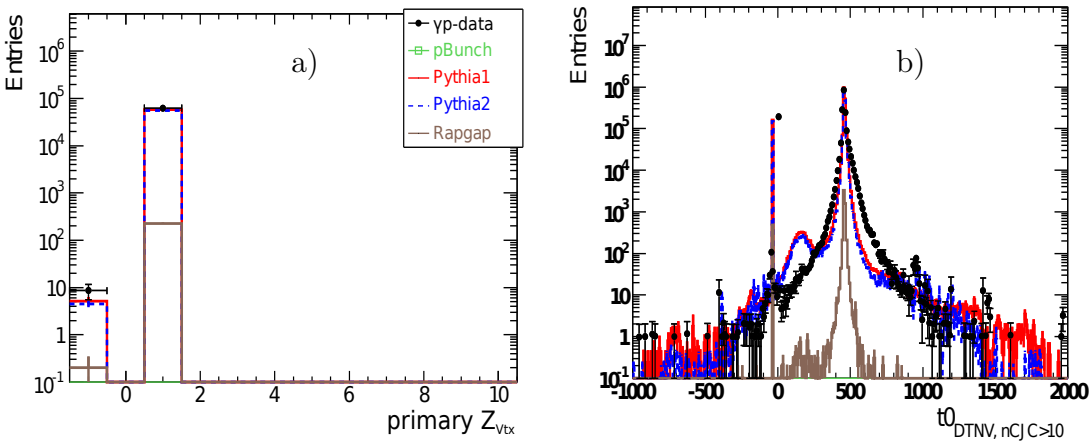

Figure 5.18: Primary Z vertex from event - type 1 (a). The track timing, t0, after all the cuts discussed in this subsection (b).

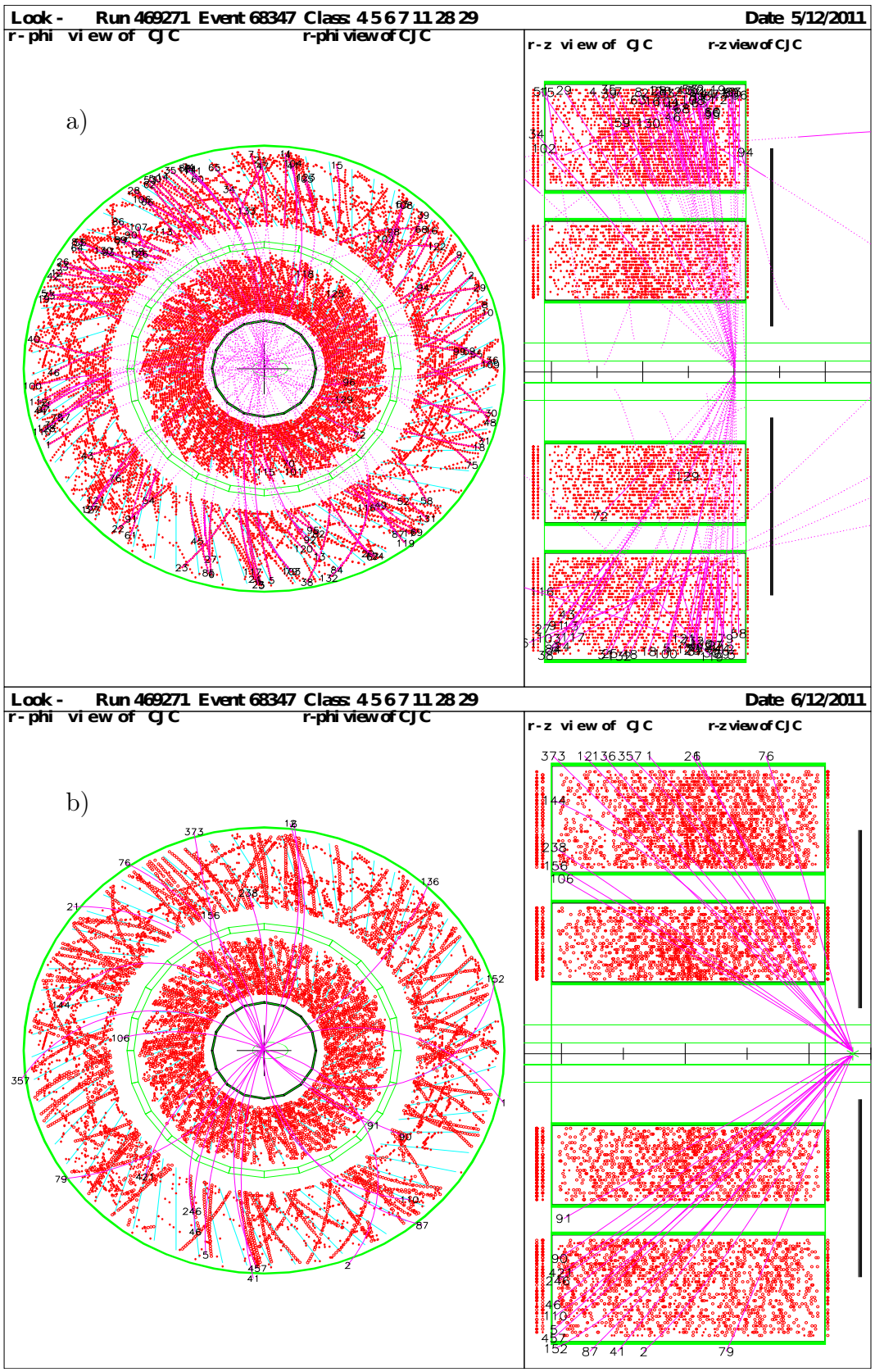

Figure 5.19: The tracking detectors CJC1 and CJC2 are full with track hits. The threshold for the number of hits in the CJC reconstruction code is by default set to 8000 hits (a), this could not provide a reliable vertex fitting. Shifting the threshold up to 12000 hits reveals the vertex fitted tracks which are out of time, pointing to the fact that these are not events from triggered ep bunch crossings. Figures were provided by Claus Kleinwort.

FINAL EVENT SELECTION
run quality "good" or " medium"
CJC1,CJC2,CIP,LAr,ToF,FTT,Veto,SpaCal,CaloTrig, Lumi HV on
$\lvert Z_{Vtx}\rvert < 35.0$ cm
$P_{T,Miss} < 25.0$ GeV
non-ep background finders (bit combinations 01, 56, 57, 67 and bit 6)
no identified scattered electron OR [is identified AND its $Q_e^2 < 4.0$ GeV^2]
$R_{SpaCal}^{scatEl} > 15.0$ cm
jet mass > 2 GeV
NOT [jet in ϕ crack AND jet size < 0.05]
$0.1 < y_{JB} < 0.9$
$P_{T,1st} > 15.0$ GeV
$P_{T,2nd} > 15.0$ GeV
$-0.5 < \eta_{1st/2nd} < 2.5$
$M_{12} > 40.0$ GeV
Beam-Gas Cuts (see section 5.7.2)

Table 5.4: Requirements for the final event selection. The operators AND, OR and NOT are logical.

5.8 Summary of Final Event and Jet Selection Requirements

The final event selection requirements are presented in table 5.4. After application of the hadronic calibration discussed in section 5.3 and this selection, the total number of selected events in data is 62182 and weighted (see section 3.7.1) events is 57533.

5.9 Selection Stability

The good quality of the data provided by the stability of the experimental detector conditions is verified by means of an offline analysis of the event yield. The event yield of the selected dijet photoproduction events per unit luminosity $\left(\text{pb}^{-1}\right)$ as a function of time, or, rather more precise, of the run number (see section 5.4) is shown in figure 5.20. For the 2006 e^+p data the check of detector deviations reveals that the event yield over the whole running period is stable within statistical fluctuations.

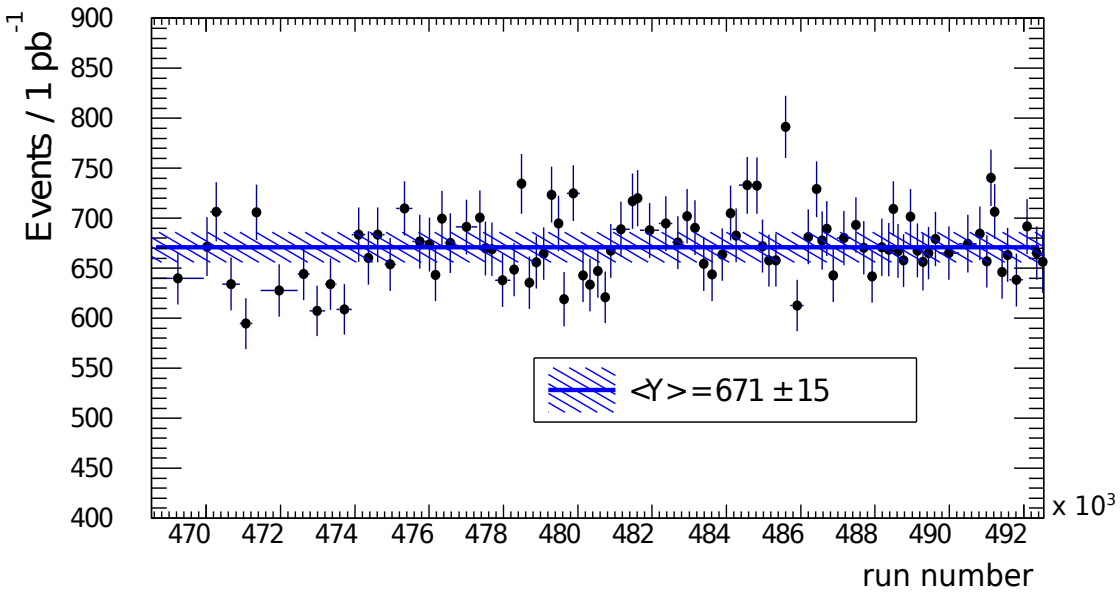

Figure 5.20: Number of selected dijet photoproduction events as a function of the run number. The average event yield $\langle Y \rangle$ is presented as solid line together with a band reflecting the 2.3% uncertainty from the luminosity (section 3.5) measurement [H112].

5.10 Trigger Studies and Efficiencies

The first insight into the trigger system of H1 was already given in section 3.7. To identify the fraction of photoproduction events, which is accepted by the H1 trigger system, one needs to determine one or several subtriggers with a corresponding positive decision for most of the selected events. For these subtriggers the efficiency is determined using monitor triggers, and corrections are derived which are then applied to the data.

First of all, reliable analysis subtriggers have to be determined. For this purpose the distribution of subtirgger bits is plotted in figure 5.21 for the γp events after all the selection cuts except the one for the scattered electron. The reason for this is described later on in this section. As one can see from this figure, the subtriggers s64 and s76 are firing most often. They are both purely LAr calorimeter subtriggers, which fire on the basis of high transverse energy deposits in a trigger tower, with additional vertex and timing conditions. Also the average prescale factors for both of these subtriggers are equal to 1.0 such that each single event is taken into consideration to be rejected or accepted by the procedure. The subtrigger s64 consists of trigger elements identifying energy deposits in the forward part of the calorimeter and LAr total transverse energy, while s76 requires only LAr total transverse energy deposits above a lower energy threshold than that of s64.

The efficiency of the analysis subtriggers is calculated by selecting events using an independent subtrigger(-s), also called *monitor subtrigger*. The efficiency is than defined by the ratio:

$$\epsilon = \frac{\mathrm{N(S \;\&\&\; M)}}{\mathrm{N(M)}}, \tag{5.14}$$

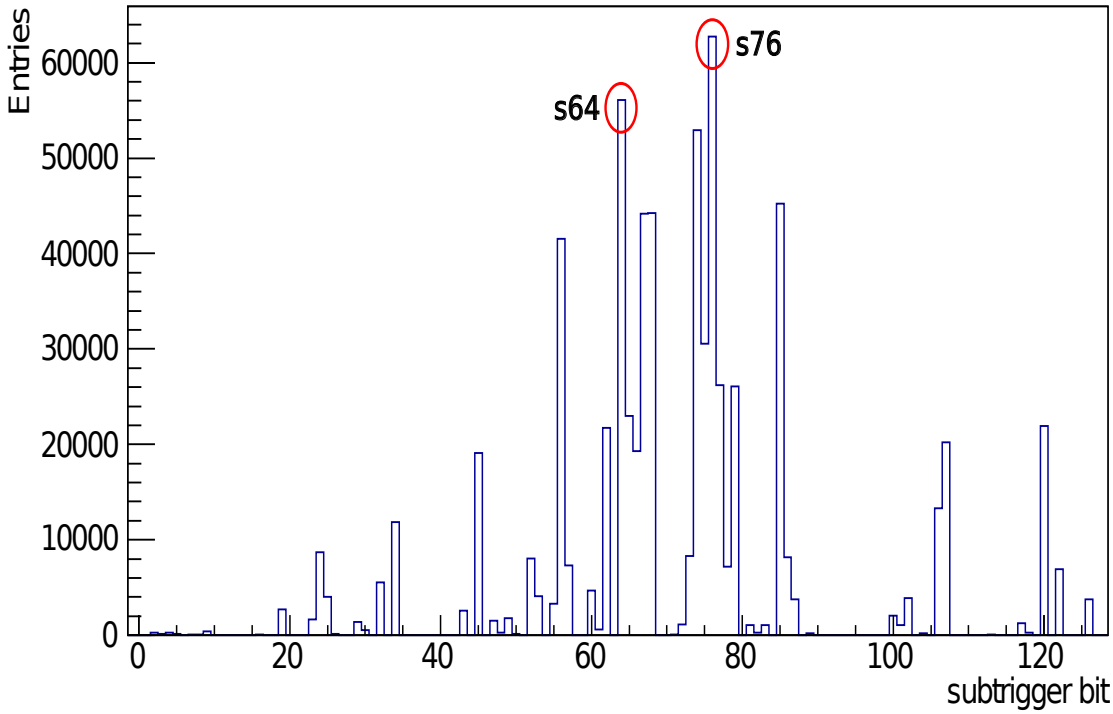

Figure 5.21: Distribution of subtrigger bits fired after the final event selection is applied to data.

where N(S && M) is the number of events triggered by both the analysis subtriggers (S stands for signal) and monitor subtriggers (M), && is the logical AND operator, N(M) is the number of events triggered by the monitor subtrigger only. For a subtrigger to be used as an independent one, it must not have the same conditions which are used in the analysis subtrigger, but it still must select events which pass the analysis selection criteria with sufficient efficiency. There is unfortunately no monitor subtrigger available which fits well for the determination of high-P_T photoproduction events. As a consequence a similar test event sample has to be defined to check the trigger efficiencies. Subtriggers s0, s1, s2 and s3 require only energy in the electromagnetic SpaCal and are therefore independent of the analysis subtriggers. Events with an electron found in the SpaCal are not rejected for the test event sample and thus are used to determine the trigger efficiency. However, the full analysis cuts would kill events passing the monitor subtriggers because of the scattered electron cuts. Thus all the cuts related to the rejection of the scattered electron in the event are switched off. The test sample is then made up of events with two high-P_T jets and an electron in the SpaCal. This is only valid if the kinematics of the test samples are similar to the pure photoproduction sample, which was shown in [Bat99, Car02, Str04].

The efficiencies of the signal trigger combination of s64 and s76 are presented in figure 5.22 (left column) as function of different observables. The amount of events selected by the signal and monitor subtriggers is low in same kinematic regions, which results in significant statistical errors in the examining sample. Different combinations of corrections applied to P_T-only (η-only) distributions were tried out, but the result was that only P_T (η) distributions were corrected for inefficiencies but

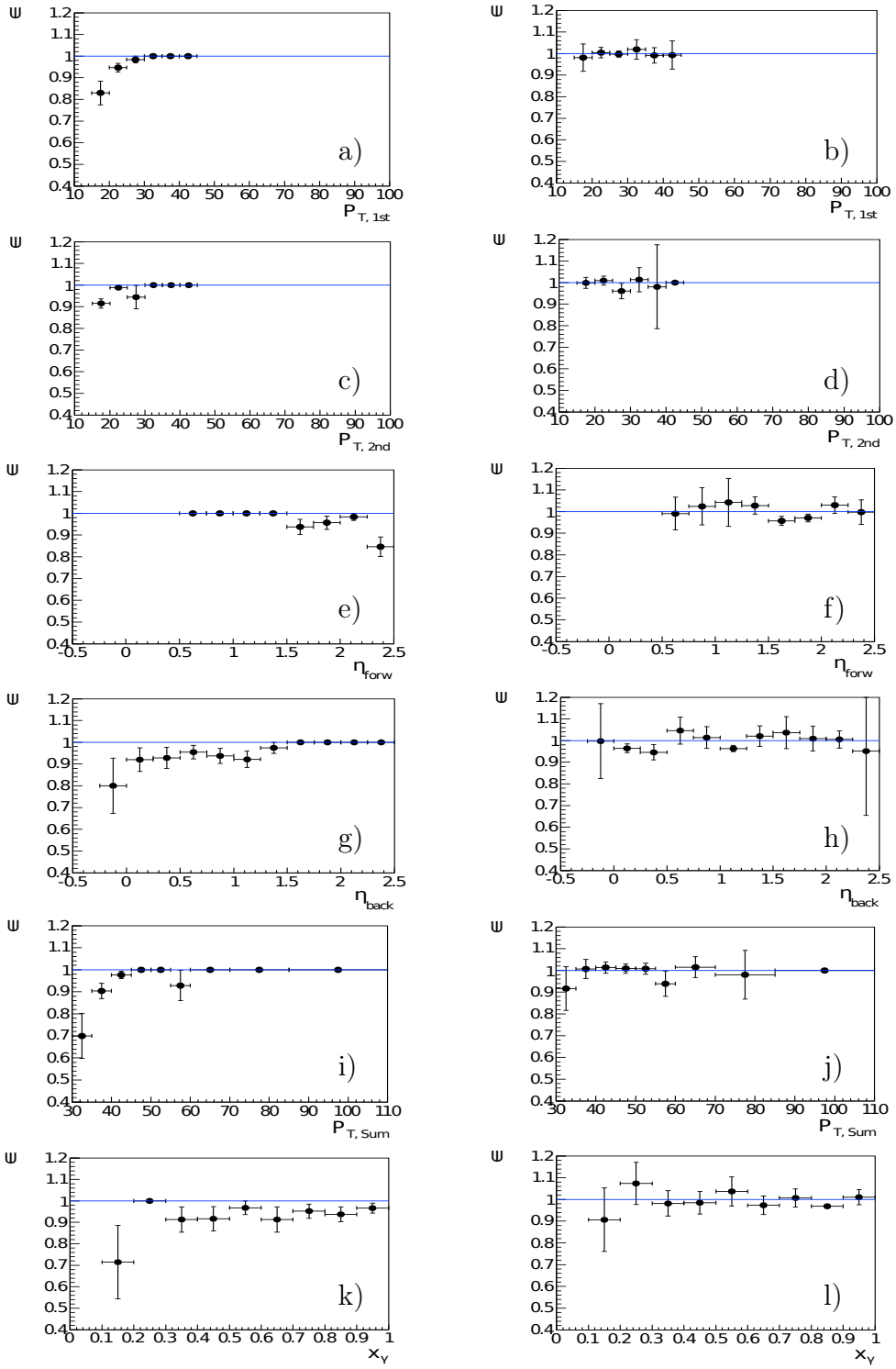

Figure 5.22: The efficiency of the combined s64 and s76 signal subtriggers as a function of $P_{T,1st}$ (a, b), $P_{T,2nd}$ (c, d), η_{forw} (e, f), η_{back} (g, h), $P_{T,Sum} = P_{T,1st} + P_{T,2nd}$ (i, j) and x_γ (k, l) before (left column) and after (right column) the correction to the data has been applied.

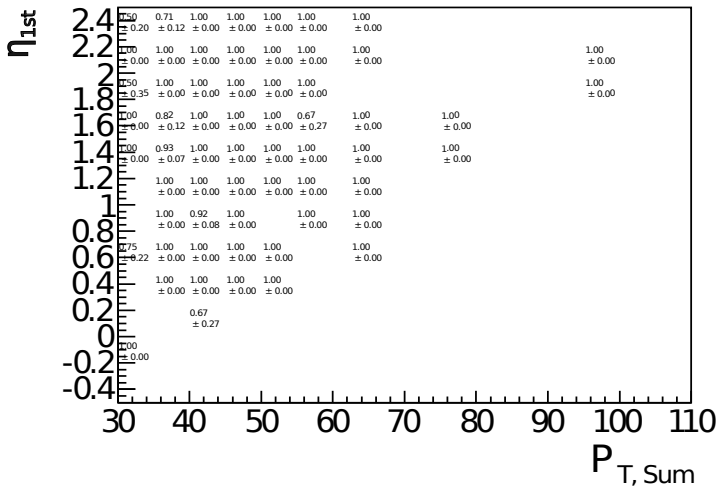

Figure 5.23: The efficiency of the combined s64 and s76 signal subtriggers shown in bins of $P_{T,Sum}$ vs bins in η_{1st}.

distributions of η (P_T) were not affected. The distributions in the right column of figure 5.22 have been corrected for inefficiencies using three iterations of corrections of the 2-dimensional distributions of $P_{T,Sum}$ versus:

1. η_{forw};
2. η_{back};
3. η_{1st}, where 3 different topologies of the jet-to-jet distributions in η were considered. The topologies are:
   - both jets i and j have $\eta_i > 2.0$ && $\eta_j > 2.0$, which corresponds to the most forward direction of the detector;
   - $\eta_i > 2.0$ && $\eta_j \leqslant 2.0$ OR $\eta_i \leqslant 2.0$ && $\eta_j > 2.0$, which means only one of the jets points into the forward direction;
   - $\eta_i \leqslant 2.0$ && $\eta_j \leqslant 2.0$, which corresponds to none of the two leading jets being in the forward direction;

An example of a 2-dimensional efficiency distribution is shown in figure 5.23, for the case of $P_{T,Sum}$ vs η_{1st}. As one can see inefficiencies are coming mainly from low P_T and very forward η regions.

Additionally, a correction factor of 1.2 was applied for the inefficiency in the region $x_\gamma < 0.2$ and $P_{T,Sum} < 45.0$.

The resulting correction from this procedure is used to correct the data. The efficiency thus obtained is unity within $2 - 5\%$ for different distributions. This uncertainty is than calculated (see section 6.4.5) and added to the global systematic uncertainty of the analysis.

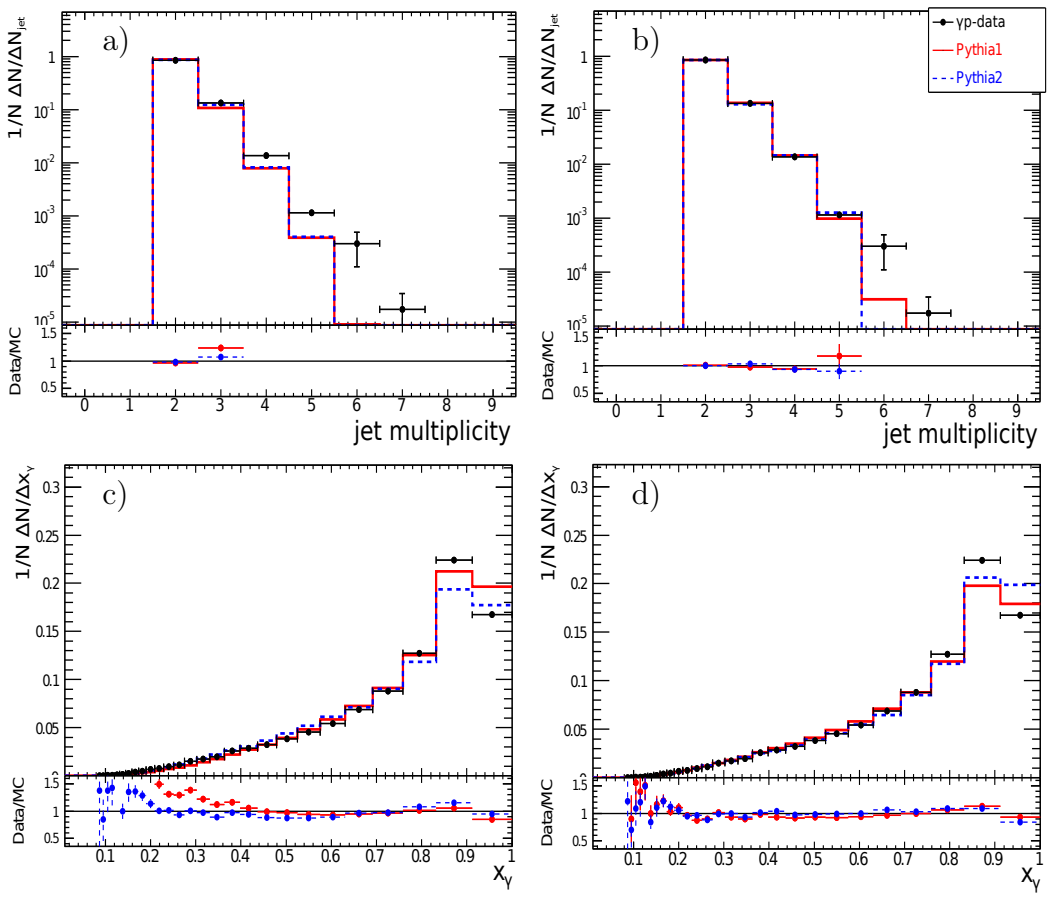

Figure 5.24: Distribution of number of jets in the events as well as the x_γ distribution displayed before (a, c) and after (b, d) the reweighting of MC events.

5.11 Data to MC Comparison

This section presents a comparison of measured data with simulated events from MC predictions obtained using the Pythia generator. These MC predictions are later used to correct the data for detector effects in order to obtain cross sections. It is therefore important that the simulation describes the data well in order to account for migrations between the measurement bins and also in and out migrations of the visible phase space used for the extraction of the cross sections.

The reconstruction efficiencies as well as corrections for dead material in front of the calorimeter have been taken into account during the simulation and reconstruction of the MC events. The remaining discrepancies between data and reconstructed observables can be assigned to uncertainties and inadequacies in the underlying physics of the MC model, as for instance, missing higher orders in the perturbative series. To improve the agreement between data and MC, weights are applied to tune the generator level distributions. The ratios of data to the reconstructed MC distributions define the weights, which are applied on generator level. If not specified otherwise, all distributions are normalized to one in order to compare shapes only.

Two very important observables in the analysis show discrepancies in the distribution of data and MC. The MC events were chosen to be corrected for inadequately

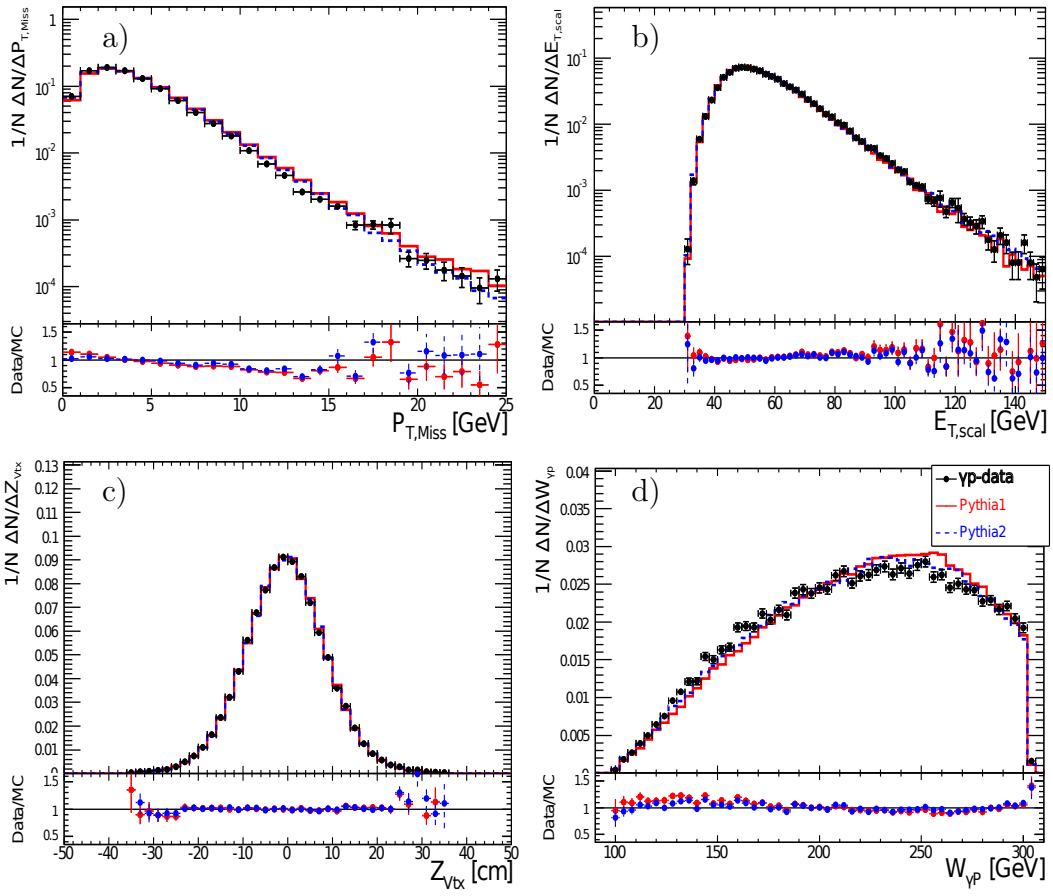

Figure 5.25: Comparison of data with Pythia MC predictions for quantities not calculated from jets: $P_{T,Miss}$, $E_{T,scal}$, Z_{Vtx} and $W_{\gamma p}$.

modeled physics effects and are displayed in figure 5.24. The left row shows the distributions of jet multiplicity and x_γ before application of the correction. Here, in figure 5.24a, one observes an increasing disagreement for events with more than two jets. For both Pythia models as well as for the Herwig generator, the one which is used later on for the MC uncertainty studies, the jet multiplicity is corrected such that each model acquires its own weights. The x_γ distribution, figure 5.24c, is not well described for lower values; below 0.4 the MC simulation underestimates data for both Pythia models. Again, independent weights were applied for each MC model. The histograms in the right row represent the same observables, but for the case when the correction weights had already been applied, see figure 5.24b, d. This improves the description of these observables and does not bias any other distributions studied in the analysis.

Figure 5.25 shows event kinematic observables which are not calculated from jets. The distribution in figure 5.25a shows the missing transverse energy. For $P_{T,Miss} < 10$ GeV the shape description of data by the MC models is well within $5-10\%$ and gets slightly worse above 10 GeV. A perfect agreement of data and MC in the distribution of the scalar transverse energy, $E_{T,scal}$, of the HFS system is shown in figure 5.25b. This is due to the improved calibration technique used in this analysis. The shape distribution of the interaction vertex Z_{Vtx} in figure 5.25c is shown for data and MC

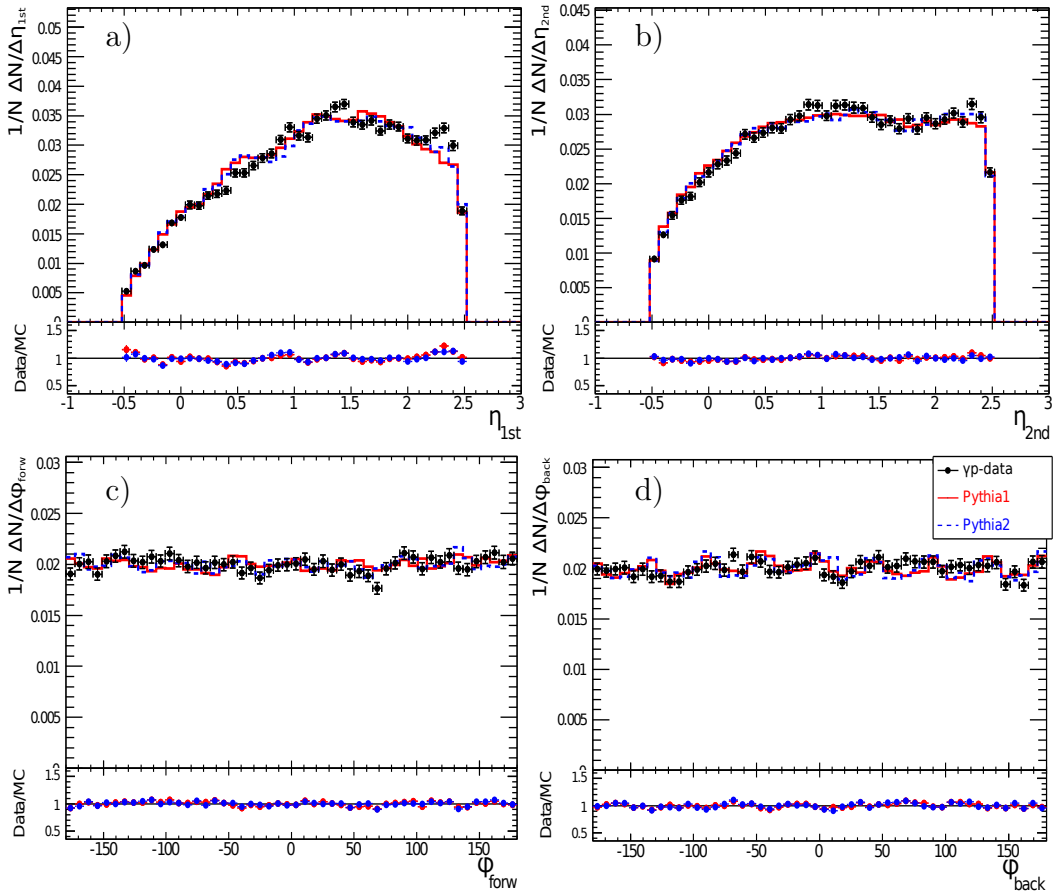

Figure 5.26: Comparison of data and Pythia MC predictions for the jet quantities η_{1st}, η_{2nd}, ϕ_{forw} and ϕ_{back}.

after a reweighting of $\mathrm{Z_{Vtx}}$ in simulation was applied; this is done on the fly each time the analysis is run over MC files. For more information refer to 5.5.1 and [Shu11]. A perfect agreement of data and MC is shown for the whole region of $|\mathrm{Z_{Vtx}}| < 35\mathrm{cm}$. Figure 5.25d demonstrates the distribution of the invariant mass of the γp system, calculated via:

$$\mathrm{W}_{\gamma p} = \sqrt{4 \cdot \mathrm{y_{JB}} \cdot \mathrm{E}_p \cdot \mathrm{E}_e}, \tag{5.15}$$

where E_p and E_e are the energies of the incident beams and $\mathrm{y_{JB}}$ is the inelasticity calculated using the Jacquet-Blondel method [BJ79]. The description of the data by both MC models is in a good agreement.

The pseudorapidity distributions of the first and second jets, leading in $\mathrm{P_T}$, are shown in figure 5.26a, b. The good correspondence of data with MC is shown for both Pythia models. Azimuthal angle, ϕ, distributions are presented for forward and backward jets ordered in η, figure 5.26c, d. These distributions remain flat in the whole range of ϕ acceptance, also revealing a perfect agreement between data and MC generators.

Due to the improved calibration technique implemented into the H1 software, the transverse momentum distributions of $\mathrm{P_T}-$ordered 1st and 2nd jets as well as

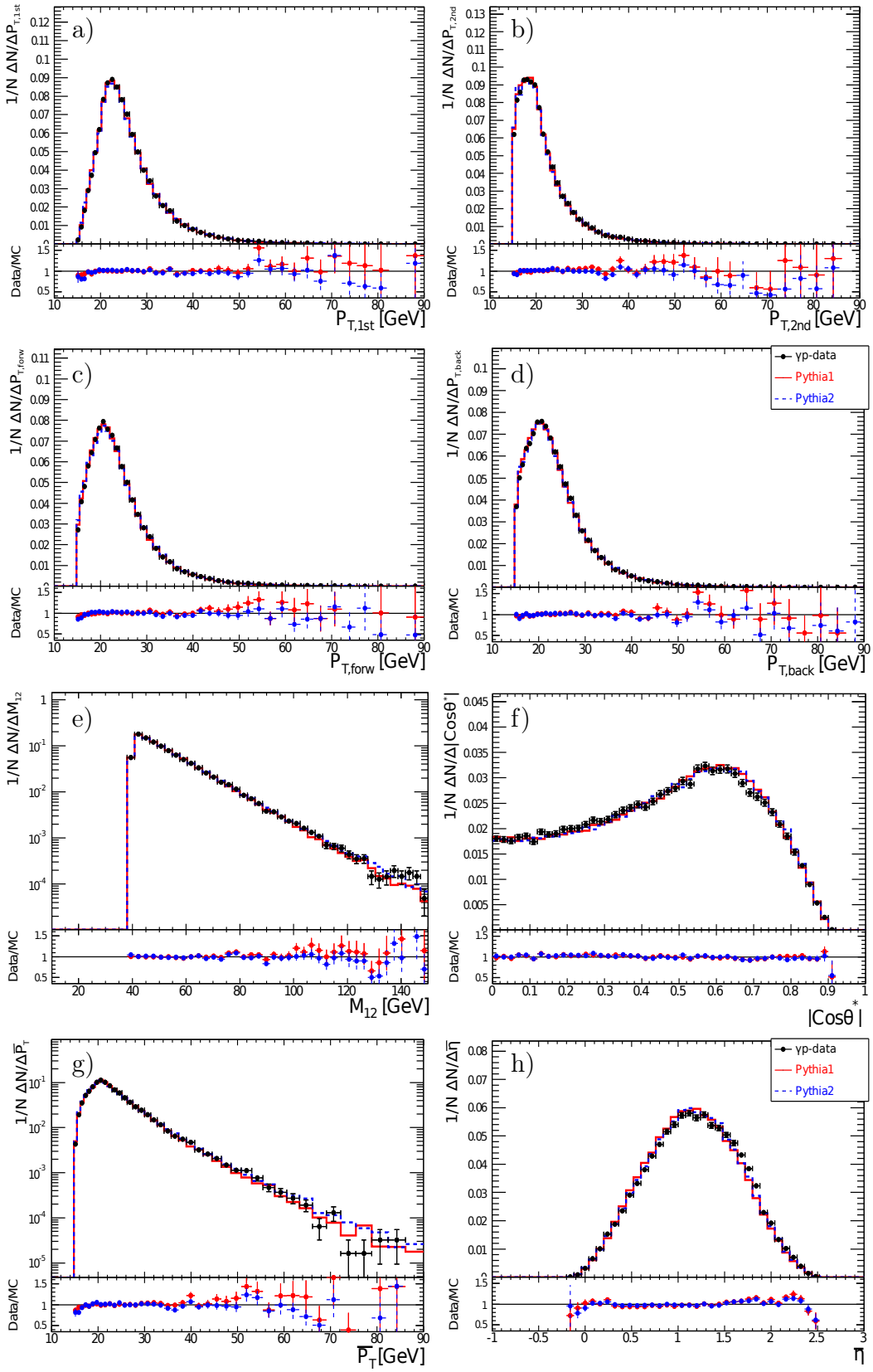

Figure 5.27: Comparison of data and Pythia MC predictions for jet quantities $P_{T,1st}$, $P_{T,2nd}$, $P_{T,forw}$ and $P_{T,back}$, M_{12}, $|\cos\theta^*|$, $\overline{P}_T$ and $\overline{\eta}$.

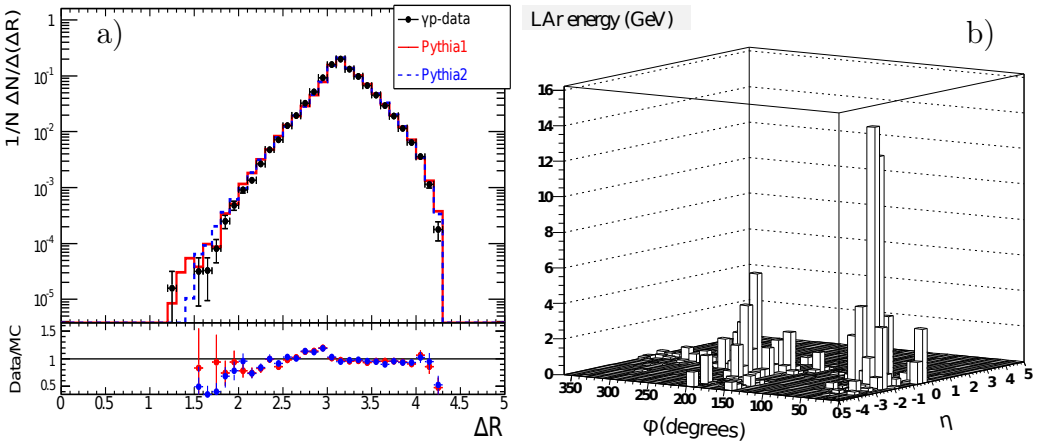

Figure 5.28: Comparison of data and Pythia MC predictions for ΔR. The event display represents the distribution of the LAr energy of particles building the jets in the $\eta - \phi$ frame, which can be easily related to the distance ΔR between the two leading jets.

$\eta-$ordered forward and backward jets display almost perfect agreement of the Pythia models with data, see figure 5.27.

Figure 5.27e, f, g and h show distributions of the invariant mass of the two leading jets, M_{12}, the absolute (see the last paragraph in section 2.4.1) value of the angular distribution of dijets in their center-of-mass system, $|\cos\theta^*|$, the average $\overline{P}_T$ and the average $\overline{\eta}$ which are defined as:

$$\overline{P}_T = \frac{(P_{T,1st} + P_{T,2nd})}{2} \text{ and } \overline{\eta} = \frac{(\eta_{1st} + \eta_{2nd})}{2}. \tag{5.16}$$

All four shape normalized distributions do not show any significant discrepancies between data and both Pythia MC models, except perhaps at the largest value of $\overline{\eta}$.

One of the interesting distributions shown in figure 5.28a is the distance between the two leading jets, which is defined via:

$$\Delta R = \sqrt{(\eta_{1st} - \eta_{2nd})^2 + (\phi_{1st} - \phi_{2nd})^2}. \tag{5.17}$$

The description of data by both MC models for the bulk of the ΔR region indicates good agreement, except for the highest bin and a few bins at low ΔR. Figure 5.28b shows a 3-dimensional representation of LAr energy deposits for a particular dijet photoproduction event, reconstructed using the h1red event display tool, in the $\eta-\phi$ frame. Clusters of these particles are afterwards built up into jet structures.

The shape normalized distribution of x_γ has already been shown in figure 5.24c. It was seen that Pythia has difficulties to predict the shape of the data. Last but not least, the shape normalized distribution of x_P is shown in figure 5.29. Both MC generators do a very good work for the whole region of this variable which dies out at 0.7.

In summary both Pythia models provide an adequate description of dijet data for

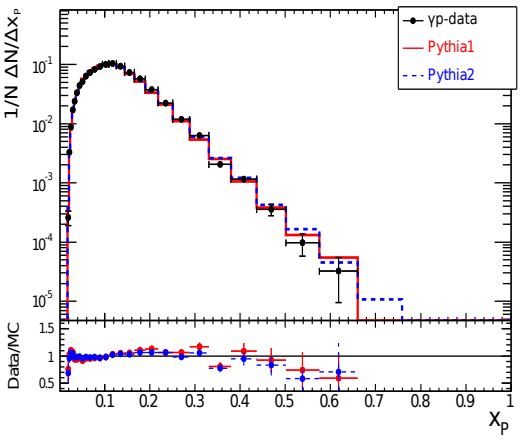

Figure 5.29: Shape normalized distribution of x_P shown for γp data compared with two Pythia MC predictions.

which a set of cross sections will be determined. A comparison of the models to the data in the final binning has also been evaluated, and both models are found to give a reasonable description of data for all bins. This is an a priori requirement for the data unfolding step which will be discussed in the next chapter.

CHAPTER 6

DETERMINATION OF THE DIJET CROSS SECTIONS

6.1 Cross Section Definition

In principle the ground rule of a particle physics analysis is to record interactions and count the number of times a particular process occurred. The cross section, σ, can be written as a Lorentz-invariant quantity. It is a measure of the probability of interactions in a two particle initial state. It has the dimension of an area. The cross section of a particular process can be measured in colliding beam experiments as:

$$\sigma^{\text{total}} = \frac{\text{N}^{\text{data}}}{\mathcal{L}}, \tag{6.1}$$

where N^{data} is the number of observed events, and $\mathcal{L}$ is the total collected luminosity (see 3.5). It defines the intensity of the colliding beams. Equation 6.1 is valid only in case of a perfect detector. In reality the picture is more complex. The quality of the event selection suffers from various detector effects and also from background events which have similar signatures as the selected signal data. The selection cuts on one hand reject background, but on the other hand they also reject signal events and thus introduce losses which have to be taken into account.

The cross section can be measured single differentially in bins of different observables with bin widths defined specifically for the detector resolutions:

$$\frac{\text{d}\sigma_i}{\text{d}\xi} = \frac{\text{N}_i^{\text{data}}/\epsilon_i - \text{N}_i^{\text{bkgd}}}{\Delta\xi \cdot \mathcal{L} \cdot \mathcal{A}_i}, \tag{6.2}$$

where i denotes the i^{th} bin of the cross section σ, N_i^{data} ($\text{N}_{\text{i}}^{\text{bkgd}}$, see section 5.5.2) is the number of data (background) events in bin i, ϵ_i is the trigger efficiency defined for data, $\Delta\xi$ is a bin width of a particular observable ξ, and $\mathcal{A}_i$ is the correction factor (acceptance) defined for each bin of the measurement. The total cross section of the reaction can be obtained by a simple integration over all the bins of a particular observable ξ. The binning of cross sections in this analysis has been chosen to

be almost[1] identical to the previous dijet measurements from H1 [Str04, H106] and ZEUS [GTLM10] in order to reproduce and compare the cross section measurements specific for the phase space criteria defined in these studies. Moreover the same binning is used for the selection on reconstructed level and the phase space of the current analysis.

6.2 The Detector, Hadron and Parton Level

It was already mentioned in section 2.5 that different levels of observation of interactions in a typical particle physics analysis exist:

The Detector Level At this level the detector registers complex electronic signals of the final state particles (leptons, photons and hadrons), thereafter the reconstruction of energies and momenta of these particles is done. The measurements of the recorded events are influenced by detector effects, such as limited acceptance, inefficiencies, migrations and finite resolutions. The effect of these imperfections is estimated using MC events, which are passed through the H1SIM program (see 4.1) and which are reconstructed in the same manner as the recorded data are. Observables at this level are referred to as detector level observables.

The Hadron Level Due to the color confinement (see 2.1) of QCD, partons from the interaction cannot be observed. The hadronization process transforms the final state colored objects into a set of colorless hadrons. The underlying partons from the hard interaction are observed as bundles of hadrons, i.e. jets. Observables of this level are referred to as hadron level observables, and the corresponding cross section is usually called the predicted (hadron level) cross section.

The Parton Level The parton level describes how individual partons from the incident particles are interacting with each other. This is the level before the fragmentation of partons into hadrons takes place. To compare partonic cross sections to the measured (hadron level) cross sections one needs to correct for the long-range hadronization effects. These hadronization corrections are obtained using MC models with parton and hadron level recorded final states, and are applied to NLO predictions.

It is easy to see that all three levels are different. Due to the hadronization effects the hadron level distributions will not correspond exactly to the distributions of the parton level, although a close correlation between the two exists. Similarly, the detector level effects prevent the detector level observables to be copies of the hadron level ones. Correction factors can be derived if on detector level data and MC distributions are in reasonable agreement, which requires a very good understanding and simulation of detector effects and a reasonably good modeling of the physics processes of the γp interaction.

[1] Except of $P_{T,1st}$ and $\overline{P}_T$, see section 6.3 for more information.

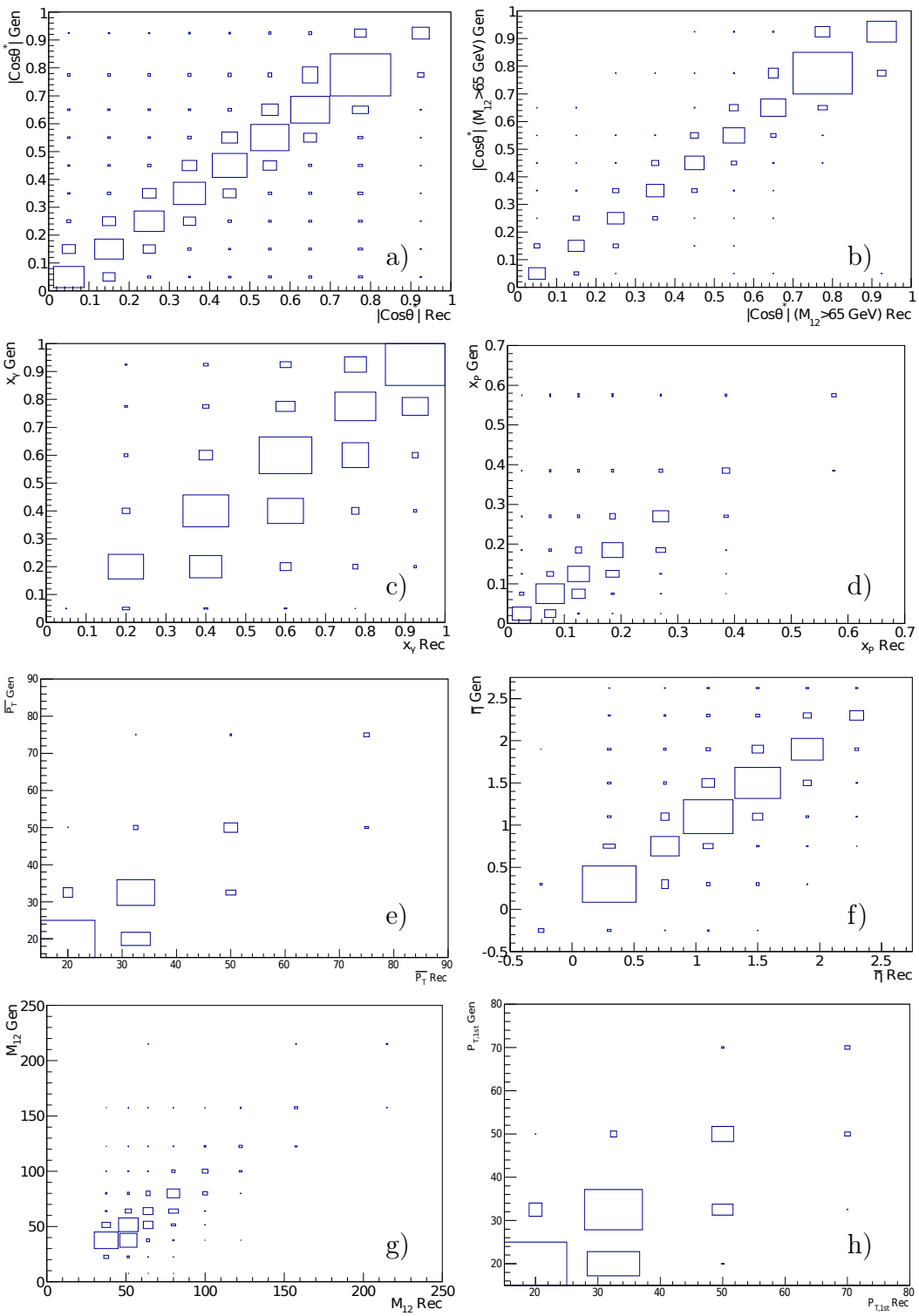

Figure 6.1: Pythia MC: correlations of GEN and REC level variables after the final selection (5.8) for variables: $|\cos\theta^*|$ (a), $|\cos\theta^*|$ with $M_{12} > 65.0$ GeV (b), x_γ (c), x_P (d), $\overline{P}_T$ (e), $\overline{\eta}$ (f), M_{12} (g), $P_{T,1st}$ (h).

6.3 Bin-By-Bin Correction Method

Previous chapter has revealed a reasonable agreement in distributions of data with MCs. Still, due to the limitations of the detector acceptance errors on reconstructed quantities exist. This fact corresponds to the smeared and shifted detector level distributions with respect to their true values. In this chapter the correction procedure of the detector level distributions to the ones of hadron level is discussed. These corrections are necessary for a comparison of cross sections with theoretical predictions which is achieved by investigating limited resolutions, mismeasurements and inefficiencies with the help of so-called bin-by-bin correction method.

MC events produced before and after the detector simulation correspond to the levels of generated (GEN or hadron level) and reconstructed (REC or detector level) quantities, respectively. These quantities are than compared with each other. Examining their correlations, the expectations are given to the perfect on diagonal distributions, but a good correlation is also satisfactory. Figure 6.1 shows the correlations between detector and hadron level of the dijet variables. The correlations are presented in logarithmic boxes for more visibility of the off-diagonal entries. Good correlations are visible for all the distributions. $|\cos\theta^*|$ alone (figure 6.1a) and together with a cut in $M_{12} > 65$ GeV (figure 6.1b) are in a good agreement on both levels as well as the distribution of the $\overline{\eta}$ (figure 6.1f). The correlations of x_γ (figure 6.1c), x_P (figure 6.1d), $\overline{P}_T$ (figure 6.1e), M_{12} (figure 6.1g) and $P_{T,1st}$ (figure 6.1h) have pronounced on-diagonal distributions and bins which are off-diagonal. This can be attributed to the fact that some forward and backward (1st and 2nd) jets are not properly matched between HAD and DET level. Thus, for instance for the $P_{T,1st}$ variable, such HAD level events with lower values of momenta exist that at the DET level the reconstructed values are smeared into the neighboring bins which are than correspond to the higher momenta.

A priori the bin sizes should be sufficiently large than the size of the obtained resolutions in order to achieve small migrations between bins. To study the migrations one uses the relation between GEN and REC level events. Besides the number of events reconstructed in bin i on REC level, N_i^{REC}, or generated in bin i on GEN level, N_i^{GEN}, additional quantities are of interest:

- N_i^{stay} is the number of events which are generated and reconstructed in bin i (figure 6.2a),
- N_i^{out} is the number of events which are generated in bin i, but are reconstructed in another bin inside the analysis phase space of the measurement (figure 6.2b),
- N_i^{in} is the number of events which are generated in a bin $\neq i$ of the analysis phase space, but are reconstructed in bin i (figure 6.2c),
- N_i^{lost} is the number of events which are generated in bin i, but are reconstructed outside the analysis phase space (figure 6.2d),
- N_i^{gain} is the number of events which are generated outside the analysis phase space but are reconstructed in bin i (figure 6.2e).

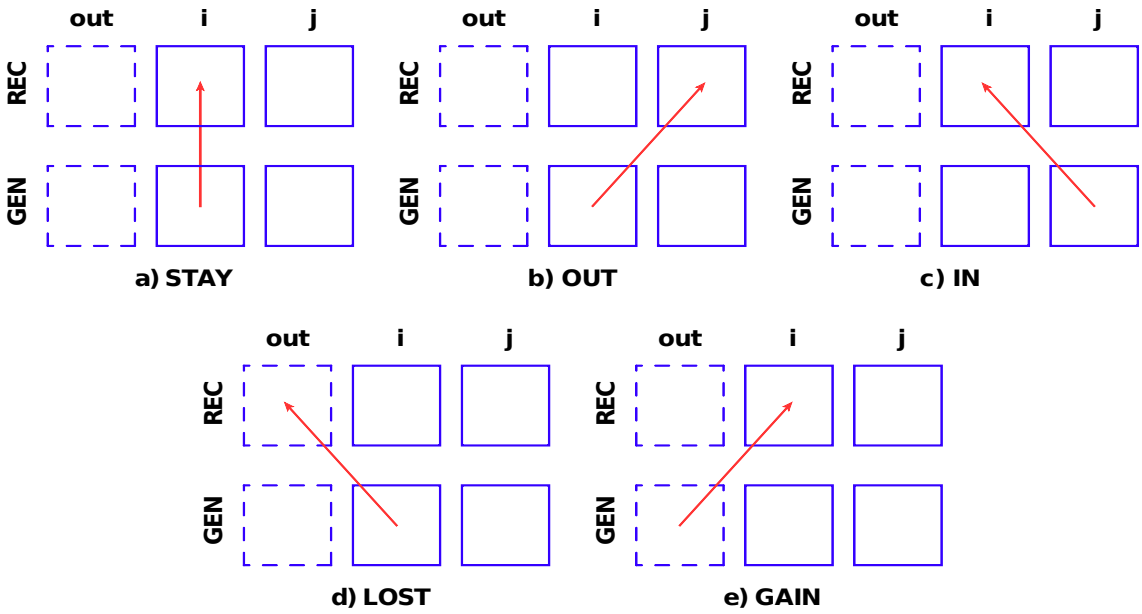

Figure 6.2: Schematic representation of possible migrations between the detector (REC) and hadron (GEN) levels. Boxes with dashed lines refer to regions outside the analysis phase space, whereas boxes with solid lines refer to the analysis phase space region.

The total number of GEN and REC events are than found using the information from all the above mentioned quantities:

- $\mathrm{N}_i^{\mathrm{GEN}} = \mathrm{N}_i^{\mathrm{stay}} + \mathrm{N}_i^{\mathrm{out}} + \mathrm{N}_i^{\mathrm{lost}}$,
- $\mathrm{N}_i^{\mathrm{REC}} = \mathrm{N}_i^{\mathrm{stay}} + \mathrm{N}_i^{\mathrm{in}} + \mathrm{N}_i^{\mathrm{gain}}$.

In order to quantify the relationship between both levels and the migration effects, the acceptance, purity and stability is studied for each measured observable. The study is made using the Pythia event generator described in 4.2.2.

Acceptance Factor $\mathcal{A}_i$ in equation 6.2 represents a correction factor of the bin-by-bin correction method. This quantity is also called the acceptance of the detector level. The acceptance of bin i is defined as:

$$\mathcal{A}_i = \frac{\mathrm{N}_i^{\mathrm{REC}}}{\mathrm{N}_i^{\mathrm{GEN}}} \ , \tag{6.3}$$

and it quantifies the number of reconstructed events in this bin with respect to the generated number of events in the same bin.

Purity The purity is defined as:

$$\mathcal{P}_i = \frac{\mathrm{N}_i^{\mathrm{stay}}}{\mathrm{N}_i^{\mathrm{REC}}} \ , \tag{6.4}$$

and it is sensitive to the fraction of events that migrate into the reconstructed level bin.

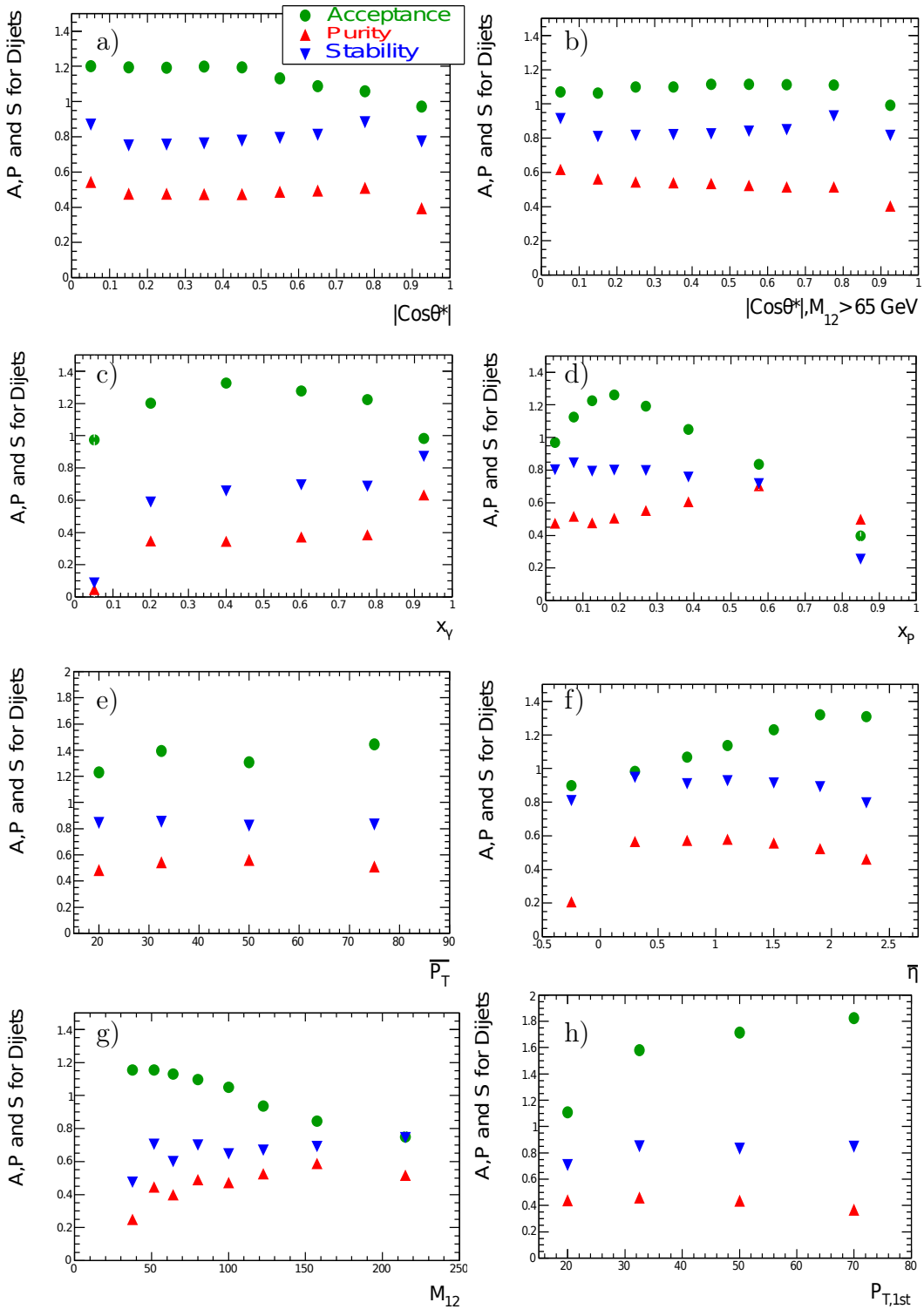

Figure 6.3: Acceptance, purity and stability obtained for the measurements of the variables: $|\cos\theta^*|$ (a), $|\cos\theta^*|$ with $M_{12} > 65.0$ GeV (b), x_γ (c), x_P (d), $\overline{P}_T$ (e), $\overline{\eta}$ (f), M_{12} (g), $P_{T,1st}$ (h).

Stability The stability is defined as:

$$\mathcal{S}_i = \frac{\mathrm{N}_i^{\mathrm{stay}}}{\mathrm{N}_i^{\mathrm{GEN}} - \mathrm{N}_i^{\mathrm{lost}}} = \frac{\mathrm{N}_i^{\mathrm{stay}}}{\mathrm{N}_i^{\mathrm{stay}} + \mathrm{N}_i^{\mathrm{out}}} \ , \tag{6.5}$$

and it reacts to the fraction of events that migrate out of the generated level bin.

To interpret stability and purity differently, they quantify the measure of correlations between true (generated) and reconstructed variables.

The set of quantities shown in figure 6.3 comprises a selection of variables for which cross sections will be determined. The distributions of purities and stabilities in this figure are relatively flat for all examined variables and are mostly above or at the level of 30%. Bins which do not satisfy this criterium of 30%, like for instance the first bin of the x_γ, $\overline{\eta}$ and M_{12} distributions, are excluded from further measurement. The binning chosen for the $\overline{\mathrm{P}}_{\mathrm{T}}$ and $\mathrm{P}_{\mathrm{T,1st}}$ distributions is not the same as in the previous H1 analysis. A study on the binning, used in the previous analysis, has shown that the level of its purity has hardly exceeded 20%. The decision was met to apply a new binning scheme for these two variables, which also can be seen in figures 6.1 and 6.3:

- $\mathrm{P}_{\mathrm{T,1st}}$: $\{15.0,\ 25.0,\ 40.0,\ 60.0,\ 80.0\}$;
- $\overline{\mathrm{P}}_{\mathrm{T}}$: $\{15.0,\ 25.0,\ 40.0,\ 60.0,\ 90.0\}$.

6.4 Systematic Uncertainties

In the following for the determination of the dijet cross sections several sources of systematic uncertainties are considered. The uncertainties can be attributed to the detector performance, trigger efficiencies, selection inefficiencies, differences in the MC models and subtraction of the background contributions, etc. A detailed study on these sources of uncertainties has been performed and is summarized in this section. The systematic uncertainties of the cross sections due to the different sources are determined differentially but are given here for the total dijet cross section. The systematic uncertainties and the statistical uncertainty are added in quadrature in order to produce the total experimental uncertainty. The individual uncertainties are presented in a tabular form for the results of the dijet cross sections in appendix A.

6.4.1 Luminosity Measurement

The integrated luminosity of the data collected in the year 2006 is determined using elastic QED Compton events (see 3.5). The total systematic error for the complete HERA II phase is 2.1%, in addition there is the statistical uncertainty which amounts to 0.8% [H112]. Furthermore, the time dependent corrections of the integrated luminosity of smaller 2006 e^+p data sample (the so-called uncorrelated systematic error on DIS event yield) results into an additional uncertainty of 1.5%.

6.4.2 Liquid Argon (LAr) Noise Measurement

Clusters due to coherent noise in the LAr calorimeter are removed by means of several algorithms on the basis of topological arguments considering electronic noise, beam-halo and cosmic muons. In order to investigate the uncertainty due to this LAr calorimeter noise removal, the analysis of jets at high Q^2 in DIS was performed [H111]. The dijet cross sections without and with the rejected noise clusters were compared. For the latter case, 20% of the removed noise clusters were randomly selected and added back to the HFS reconstruction in data. Events passing the HADROO2 algorithm were stored in new MODS files, which allowed to compare the dijet quantities. The effect of noise on the dijet cross sections has a tiny impact, the control distributions were equally well described, and the correlated uncertainty in case of dijets is taken to be 0.6%.

6.4.3 Hadronic Energy Measurement

The variation of the energy of all HFS objects by ±1%, reveals the uncertainty of the hadronic energy scale in the measurement of dijets cross section. This variation of the HFS energies is done on the completely reconstructed and calibrated hadronic final state. The result yields the uncertainty on the hadronic energy measurement of ±4.1% for the total cross section.

6.4.4 Model Uncertainty Measurement

For this study the Herwig (see section 4.2.3) MC model was used as an alternative model for photoproduction of jets. Cross sections were obtained using correction factors determined for Herwig. The difference in the obtained cross sections to those obtained with correction factors from Pythia (see section 4.2.2) is assigned as the model uncertainty for this analysis and is ±1.9%.

6.4.5 Trigger Efficiency Uncertainty Measurement

The trigger efficiency uncertainty determination was performed on quantities, which were not used in the subtrigger reweighting procedure (see section 5.10). These are the y_{JB}, η_{2nd} jet and x_γ variables. The systematics study was made on all the variables and there was no difference observed. The preference was given to x_γ as this variable enters the cross section measurements. Figure 5.22l represents the reweighted x_γ trigger efficiency obtained for data. The idea is to shift up and down the event weight in case if $x_\gamma < 0.5$ by ±4% else if $x_\gamma > 0.5$ by ±2%. The impact to the total uncertainty is ±2.4%.

6.4.6 Background Measurement

In order to investigate the impact of the background subtraction uncertainty two background MC models (Rapgap and Djangoh) were used. Both models were reweighted according to the study performed on NC DIS low Q^2 jet events (see section 4.3). The uncertainty is taken as the difference between cross section results

obtained by subtracting either Rapgap or Djangoh MCs events from data. The resulting uncertainty is $\pm 0.1\%$.

6.4.7 Uncertainty of the non-*ep* Selection

The effect of the non-*ep* selection criteria on the uncertainty was investigated. In order to do this the different sets of non-*ep* background finders were switched off and on:

- the combination of finders 01 was switched OFF while 56, 57, 67 and 6 were switched ON;
- the combination of finders 01 was switched ON while 56, 57, 67 and 6 were switched OFF.

The difference in the obtained cross sections is less than a per mil level. The decision, not to include this source into the total uncertainty, has been made.

6.5 NLO QCD Calculations

The program[2] used for the calculation of the next-to-leading order (NLO) photoproduction dijet cross sections is the one of Klasen and Kramer [KKK98, KK97]. It applies the phase space slicing method [GKS84, BOO89] in order to cancel the infrared and collinear singularities present in $2 \rightarrow 3$ matrix elements and in the virtual corrections to the $2 \rightarrow 2$ contributions. The number of active flavors is set to 5, and the renormalization and factorization scales are set equal to $\mathrm{P_{T,1st}}$, which is the highest transverse momentum of the parton from the hard interaction in the event. The calculations are performed in the $\overline{\mathrm{MS}}$ scheme. CTEQ61 [$\mathrm{S^{+}03}$] and GRV-GNLO [FP92] are used as parameterizations for the parton densities of the proton and photon, respectively. The value $\alpha_s(M_Z) = 0.118$ is used as for the proton parameterization.

The NLO prediction is corrected for hadronization effects bin-by-bin, thus producing the nominal NLO prediction for this analysis:

$$d\sigma = d\sigma^{\mathrm{NLO}}_{\mathrm{partons}} \cdot \frac{d\sigma^{\mathrm{MC}}_{\mathrm{hadrons}}}{d\sigma^{\mathrm{MC}}_{\mathrm{partons}}} = d\sigma^{\mathrm{NLO}}_{\mathrm{partons}} \cdot C_{\mathrm{had}} \ , \tag{6.6}$$

where $d\sigma^{\mathrm{NLO}}_{\mathrm{partons}}$ is the dijet cross section for partons in the final state of the NLO calculation. From the above equation, it is clear that the hadronization correction factor, C_{had} defines the ratio of the dijet cross sections at the hadron level and parton level. The complete list of correction factors C_{had} for the different cross sections is presented in appendix A.

The following sources of theoretical uncertainties were investigated:

- only the renormalization scale was changed by $2^{\pm 1} \cdot \mathrm{P_{T,1st}}$.

[2]The NLO program was kindly provided by professor Juan Terron [Ter].

- only the factorization scale was changed by $2^{\pm 1} \cdot \mathrm{P}_{\mathrm{T,1st}}$.
- the model uncertainty of the hadronization corrections was estimated by taking half of the difference of the spread between the hadronization correction factors of the Pythia and Herwig MC models.

The above uncertainties were summed in quadrature and are presented in the figures as the shaded band to the nominal NLO prediction (blue line), which is labeled NLO⊗HAD.

CHAPTER 7

RESULTS

This chapter presents the measured single differential inclusive dijet cross sections in photoproduction for the reaction $ep \rightarrow \text{jet jet } X$ for the following phase space:

$Q^2 < 4.0$ GeV^2
$0.1 < y < 0.9$
$P_{T,1st} > 15.0$ GeV
$P_{T,2nd} > 15.0$ GeV
$-0.5 < \eta_{1st/2nd} < 2.5$
$M_{12} > 40.0$ GeV

The results are presented at the level of stable hadrons. Cross sections are compared to the Pythia MC generator (see section 4.2.2), which has LO matrix elements, initial and final state parton showers and uses the Lund string model of hadronization. The total cross section from Pythia is scaled up by a factor 1.05 to match the total cross section of the data. This factor is applied to Pythia prediction for all cross section distributions. The data have been corrected for detector effects and are shown with statistical (inner error bars) and total uncertainty (outer error bars). The total photoproduction dijet cross section is measured to be:

$$\sigma(ep \rightarrow \text{jet jet } X) = 597.73 \pm 5.74 \text{ (stat.)} \pm 34.97 \text{ (syst.) pb.}$$

The single differential cross sections are also compared to NLO predictions, presented with (NLO⊗HAD) and without hadronization corrections applied (see section 6.5). The total cross section from the NLO prediction is 552.44 pb and it is 7.58% lower than the measured one. The model uncertainty and the uncertainty due to the hadronic energy scale are the dominant contributions to the total uncertainty for each of the measured cross sections presented in this analysis. Each cross section distribution is accompanied by a ratio plot, which shows the ratio of data to

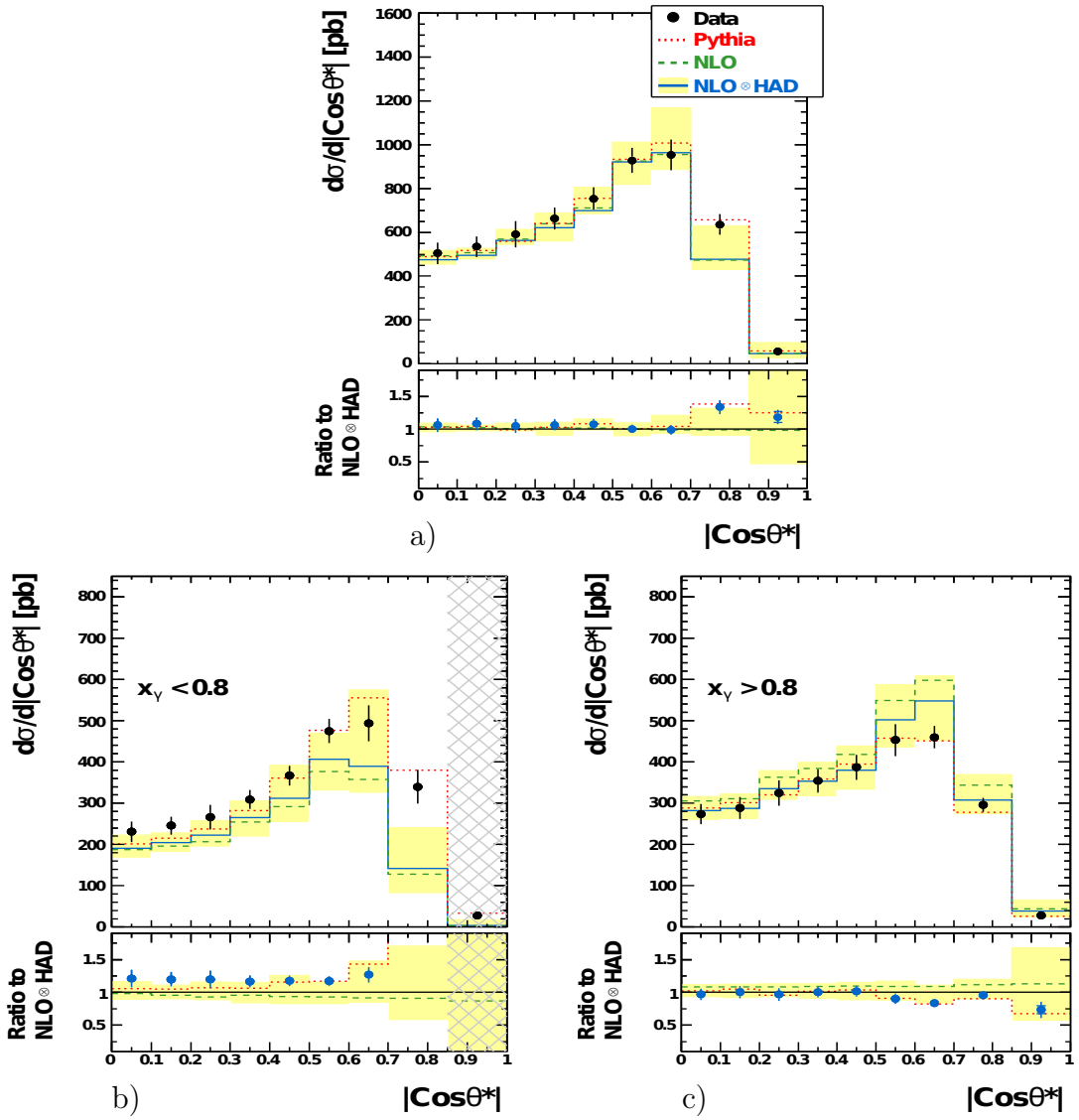

Figure 7.1: Cross sections as a function of $|\cos\theta^*|$, a) no condition on x_γ, b) for $x_\gamma < 0.8$ (resolved enhanced photoproduction region), c) for $x_\gamma > 0.8$ (direct enhanced photoproduction region). The data are compared to NLO predictions with (solid line) NLO⊗HAD and without (dashed) hadronization corrections and to Pythia predictions (dotted) scaled by a factor of 1.05. The inner error bar of the data points indicates the statistical and the outer error bar the total uncertainty. The band shows the total uncertainty of the NLO prediction. Below each figure the ratios to the NLO⊗HAD prediction are shown.

NLO⊗HAD (blue points with statistical and total uncertainties as discussed above) and the ratios of Pythia and NLO to NLO⊗HAD.

7.1 Differential Cross Section w.r.t. $|\cos\theta^*|$

The dijet cross section as a function of $|\cos\theta^*|$ is shown in figure 7.1. This distribution has sensitivity to the dynamics of the hard interaction. The measurement is presented without any requirement on x_γ (figure a) as well as for the resolved and direct photon enhanced regions, $x_\gamma < 0.8$ (figure b) and $x_\gamma > 0.8$ (figure c),

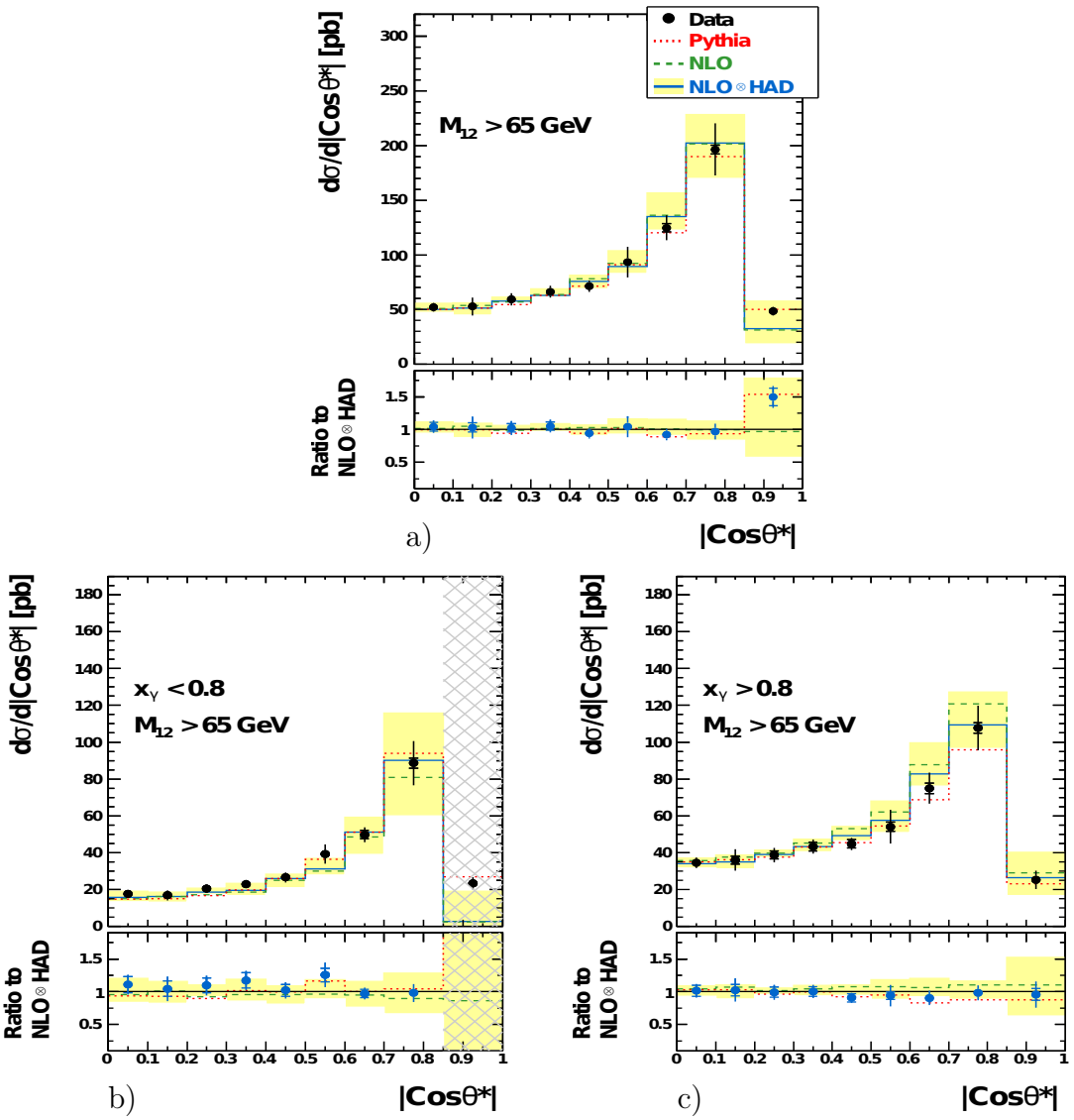

Figure 7.2: Cross sections as a function of $|\cos\theta^*|$ with $M_{12} > 65$ GeV, a) no condition on x_γ, b) for $x_\gamma < 0.8$, c) for $x_\gamma > 0.8$. For further details, see the caption to figure 7.1.

respectively. The dashed region of the last bin in figure b corresponds to a purity of less than 30% in this bin, and thus it is not considered a safe measurement. This applies to all dashed regions in any of the following cross section distributions.

All three distributions show a rise in the cross section with decreasing scattering angle θ^* and a subsequent drop at 0.7 that can be mainly attributed to the jet transverse momenta cuts, which play a more important role the closer the jets get to the $\pm$z direction. These cuts suppress the phase space in the large $|\cos\theta^*|$ region. The Pythia prediction agrees very well within the data uncertainties. In figure a, the uncertainties are large for both the data and the NLO prediction, for data they are around $6-10\%$, and for the prediction they are within $3-21\%$ for the first 7 bins and $\sim 50\%$ for the last two bins. The NLO prediction agrees with the data within uncertainties. The statistical uncertainty of data (except for the last bin) is less than 1.5% (4.6%). The NLO prediction for $x_\gamma < 0.8$ is slightly below the data,

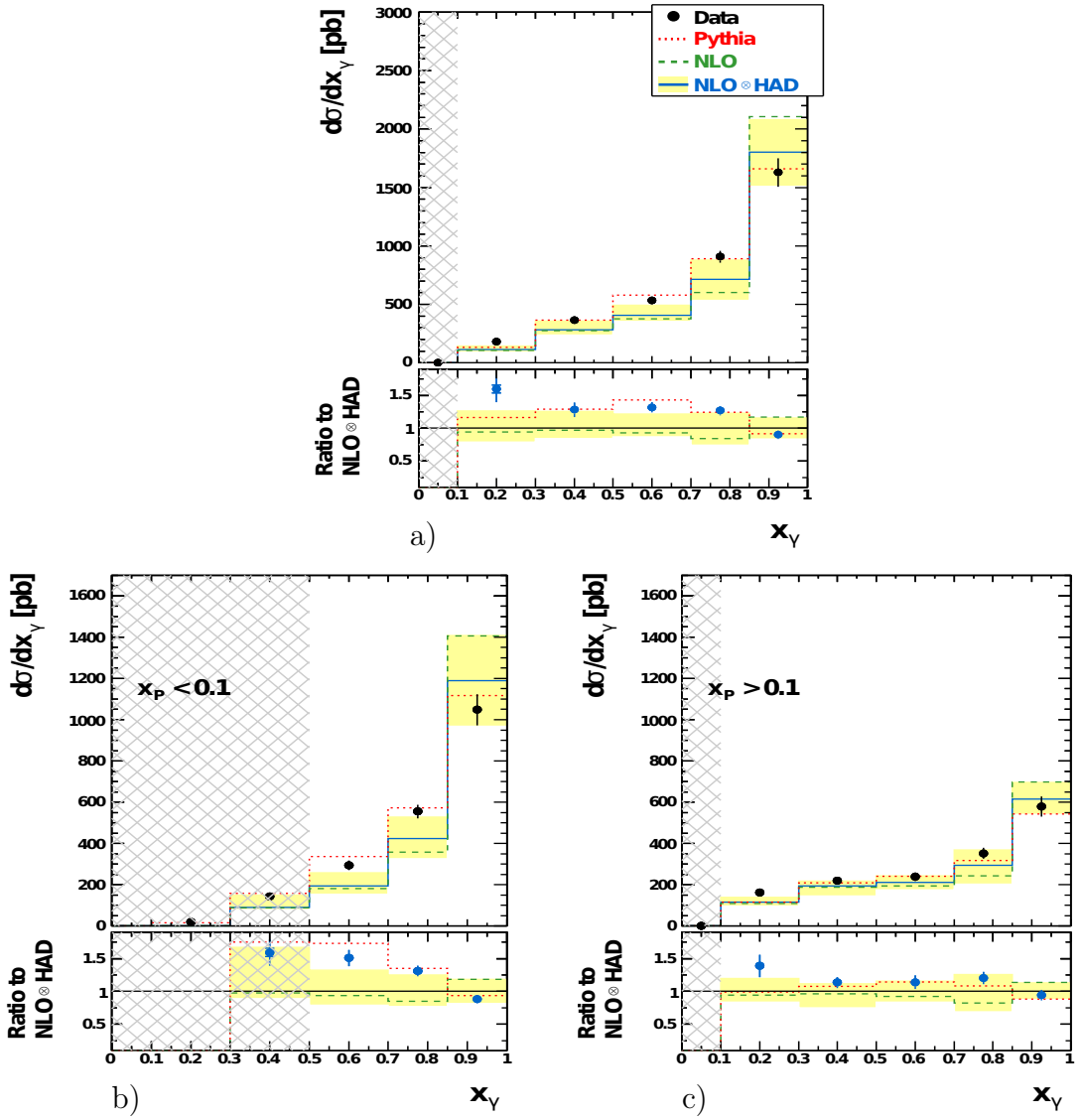

Figure 7.3: Cross sections as a function of x_γ, a) no condition on x_P, b) for $x_P < 0.1$, c) for $x_P > 0.1$. For further details, see the caption to figure 7.1.

but agrees with it within uncertainties, except for the last two bins. For $x_\gamma > 0.8$ the NLO prediction shows good agreement with the data. The region with resolved enhanced contribution is described by the Pythia prediction within $\sim 20\%$, whereas the direct enhanced photon region is very well described.

Applying an additional cut on the dijet invariant mass, which corresponds to the center-of-mass energy of the hard subprocess, $M_{12} > 65$ GeV, reduces the effect of the phase space restriction due to the requirement on the transverse momenta of the jets and changes the shape of the measured cross section towards the expectation of the QCD matrix elements.

Figure 7.2 shows the cross sections as a function of $|\cos\theta^*|$ with the $M_{12} > 65$ GeV requirement. All three cross sections show good agreement of the NLO and Pythia predictions with the data. The cross section for the $x_\gamma < 0.8$ region rises more rapidly than that for the $x_\gamma > 0.8$ region as expected due to the dominating gluon

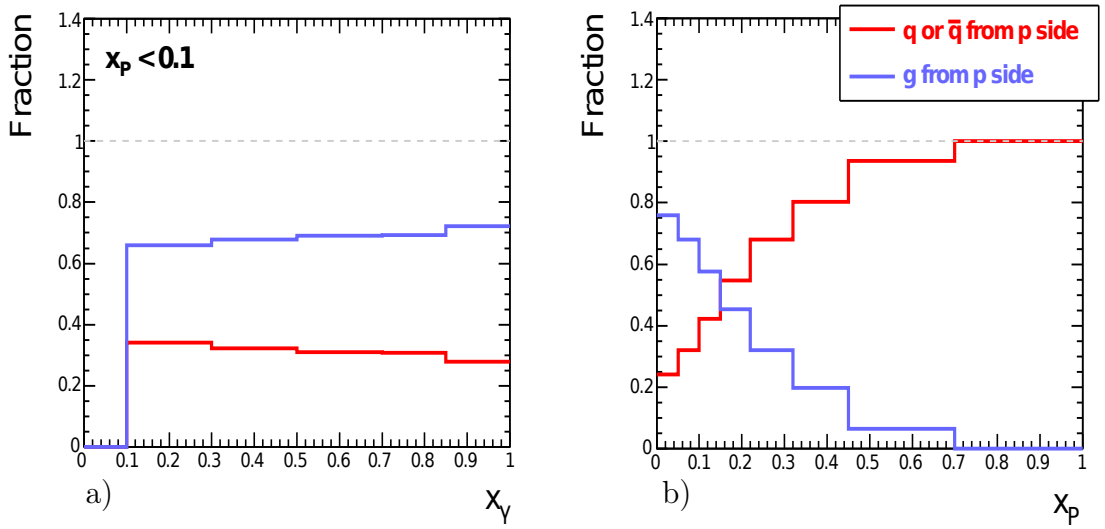

Figure 7.4: Fraction of events predicted by Pythia to be due to a gluon (g) or quark (q or $\bar{q}$) from the proton, a) as a function of x_γ and for $x_P < 0.1$, b) as a function of x_P.

propagator in resolved processes [Erd97].

7.2 Differential Cross Section w.r.t. x_γ

The dijet cross section as a function of x_γ is presented in figure 7.3. The cross section is also presented divided into $x_P < 0.1$ and $x_P > 0.1$ regions. For $x_P < 0.1$ the estimated fraction of events induced by gluons from the proton side is about 70% (see figure 7.4a) depending little on x_γ. Looking at the fractions as a function of x_P, the fraction of gluon induced events decreases to less than 20% for the highest x_P bins (figure 7.4b). Therefore, two regions can be roughly differentiated, as a gluon ($x_P < 0.1$) and a quark scattering ($x_P > 0.1$) regions.

The NLO predictions describe the data within the theory uncertainties, except for the lowest x_γ bins, but they are systematically below the data and have a different shape than the data, particularly for $x_P < 0.1$. For the highest x_γ bin the predictions are above the data but within the theory uncertainties. Pythia provides a good description of the x_γ distributions.

7.3 Differential Cross Section w.r.t. x_P

The dijet cross section as a function of x_P is presented in figure 7.5. The measurement is also presented for x_P with a division into resolved and direct enhanced regions. For $x_\gamma < 0.8$ ($x_\gamma > 0.8$) mainly quarks (photon) enter the hard subprocess from the electron side, whereas the contribution from gluons is small, figure 7.6b (7.6c). The cross sections rise at small x_P and drop by almost four orders of magnitude with increasing x_P. The NLO prediction is in good agreement with the data and the Pythia prediction is also reasonably good. For the lowest x_P bin and $x_\gamma < 0.8$, the

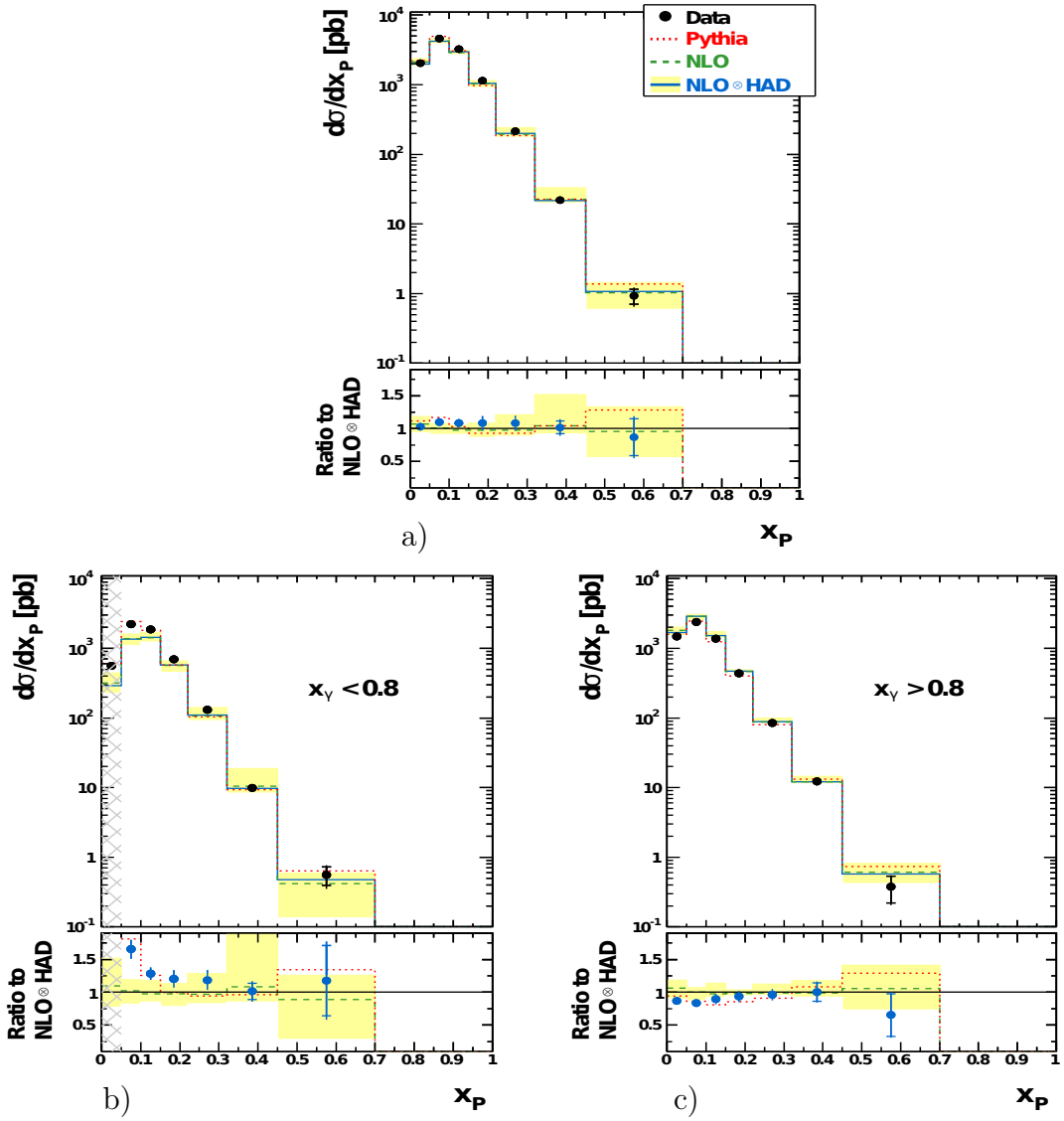

Figure 7.5: Cross sections as a function of x_P, a) no condition on x_γ, b) for $x_\gamma < 0.8$, c) for $x_\gamma > 0.8$. For further details, see the caption to figure 7.1.

NLO prediction lies below the data by more than 3σ, whereas for $x_\gamma > 0.8$ it lies above data but within the uncertainty band.

The dependance of the cross sections on the pseudorapidities of the dijets are expected to be sensitive to the densities of the interacting partons. Therefore the cross sections as a function of x_P (and shown later as a function of $\overline{P}_T$ and $P_{T,1st}$) are measured for three different topologies of the jets:

1. both jets are in the backward direction ($\eta_{i,j} < 1$); for example see figures 7.7a, b and c. Backward direction is referred to the direction, where both jets are going least forward (proton direction). In fact, one or both jets may be pointing into the backward direction.

2. one jet is in the backward ($\eta_i < 1$) and the other jet is in the forward ($\eta_j > 1$) direction; for example see figures 7.7d, e and f.

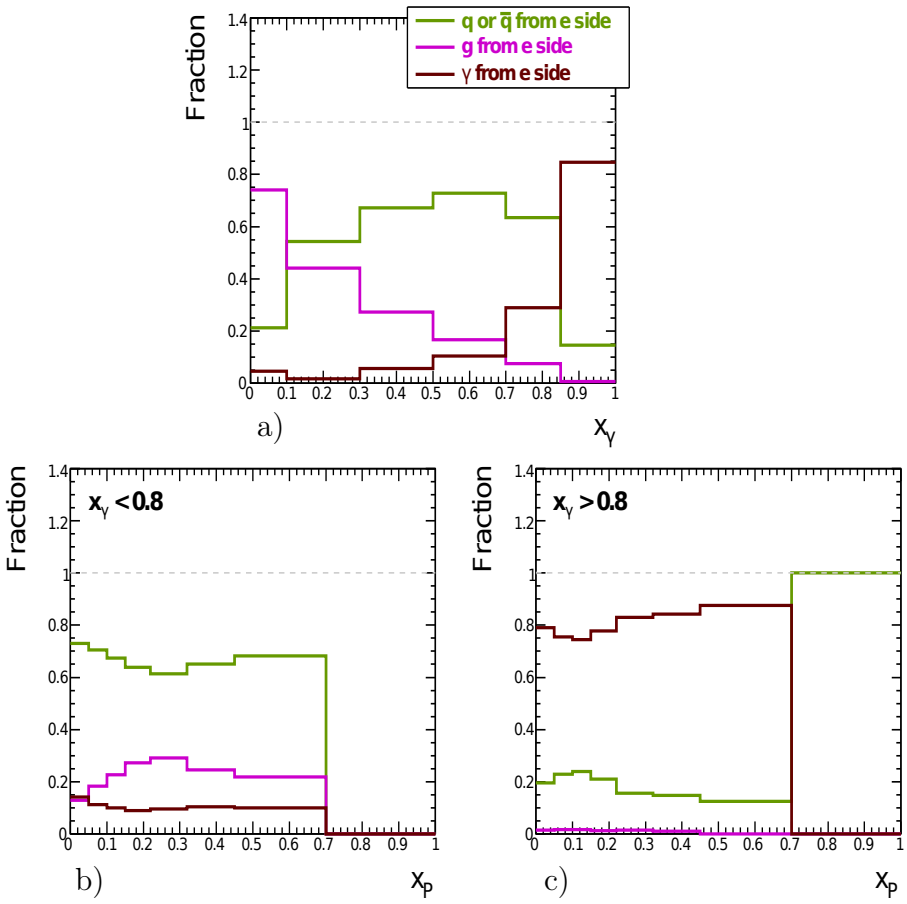

Figure 7.6: Fraction of events induced by g, q, $\bar{q}$ or γ from the electron side as predicted by Pythia, a) as a function of x_γ, b) as a function of x_P for $x_\gamma < 0.8$ and c) for $x_\gamma > 0.8$.

3. both jets are in the forward direction ($\eta_{i,j} > 1$); for example see figures 7.7g, h and i.

Figure 7.7 presents the cross sections for these different topologies as a function of x_P and for all of x_γ and for $x_\gamma < 0.8$ and $x_\gamma > 0.8$. Overall both, NLO and Pythia predictions describe the measurements with data within uncertainties. Additionally, the figure 7.8 shows the corresponding fractions of g, q, $\bar{q}$ and γ induced interactions from the proton and electron side, as obtained from Pythia predictions.

The Pythia prediction describes the data quite well for all three topologies. The NLO prediction agrees in most bins with the data within the uncertainty band. It is below the data at low x_P for $x_\gamma < 0.8$ and all topologies, but particularly for the topology $\eta_i < 1$, $\eta_j > 1$, while for $x_\gamma > 0.8$ it is slightly above the data, but mainly within the theory uncertainties. From this behavior (and the fractions of partons shown in figure 7.6) one can conclude that the deviation for $x_\gamma < 0.8$ is not due to the PDFs of the proton, but is expected to be due to deficiencies in the much less well known parton densities of the photon.

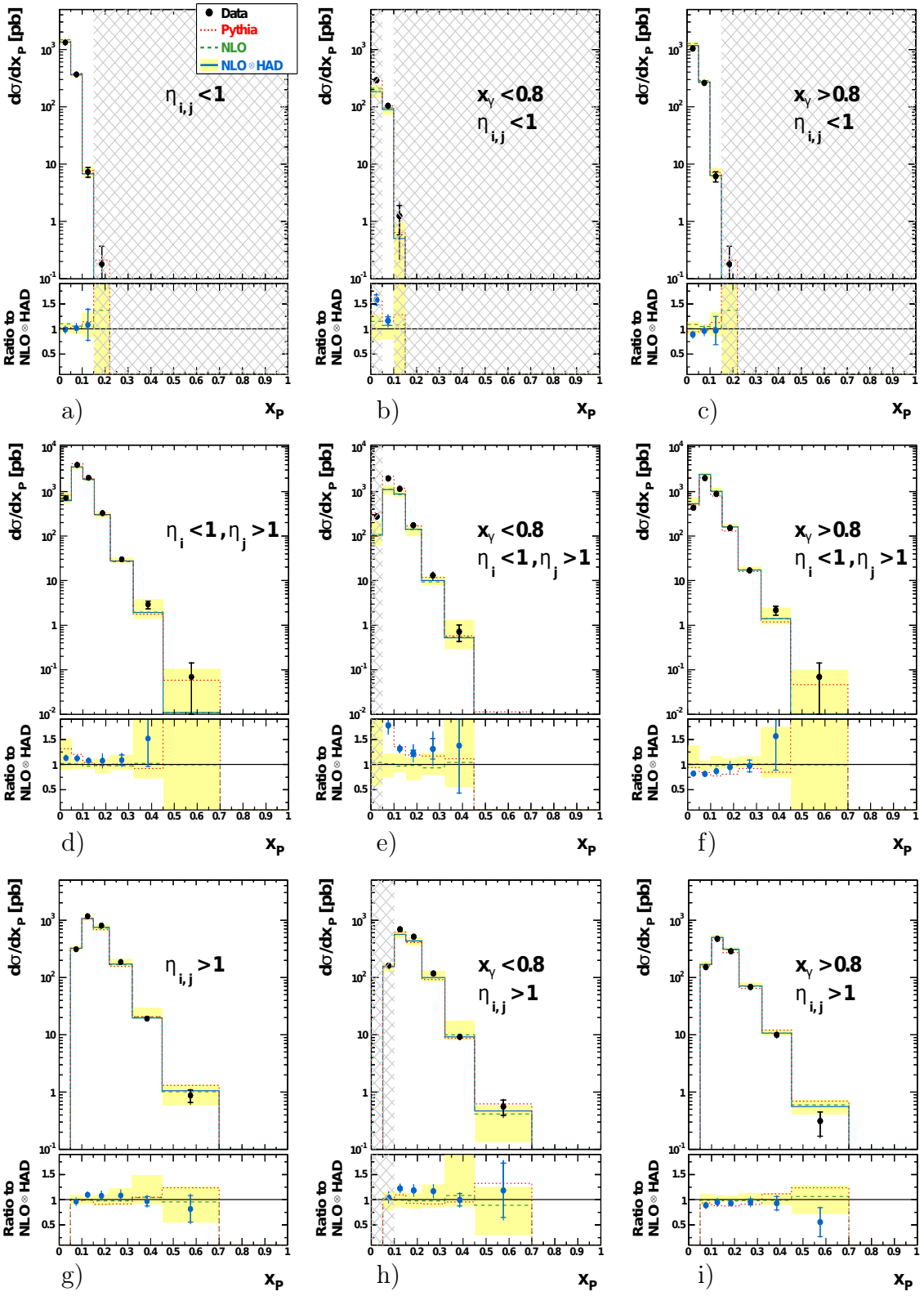

Figure 7.7: Cross sections as a function of x_P for different jet topologies in pseudorapidity $\eta_{i,j}$ and for $x_\gamma < 0.8$ and $x_\gamma > 0.8$. For further details, see the caption to figure 7.1.

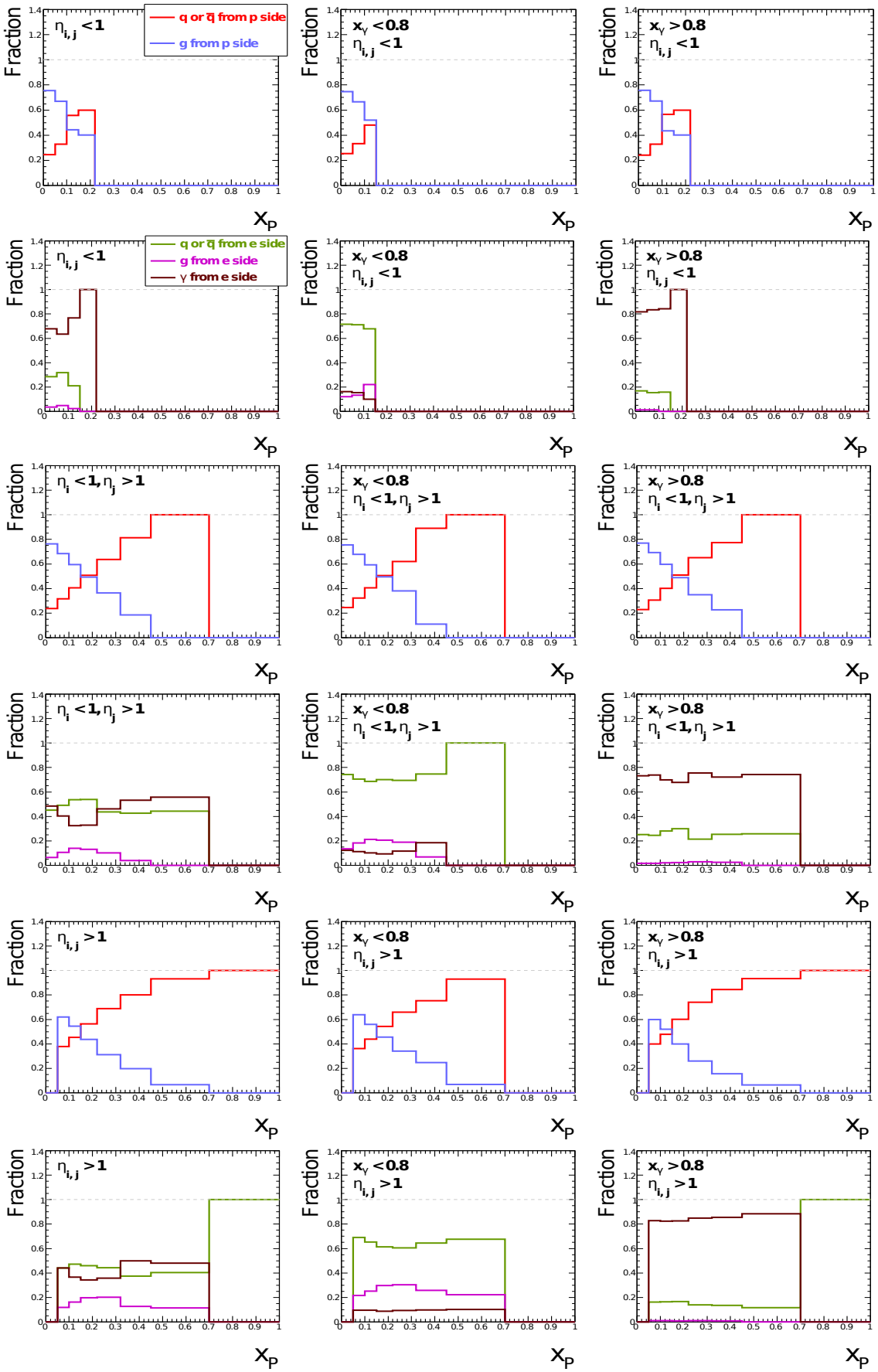

Figure 7.8: Fraction of events induced by g, q, $\bar{\mathrm{q}}$ or γ from the proton and electron sides, respectively, as predicted by Pythia. The results are presented as a function of x_P for different $\eta_{i,j}$ jet topologies. For further details, see the caption to figure 7.1.

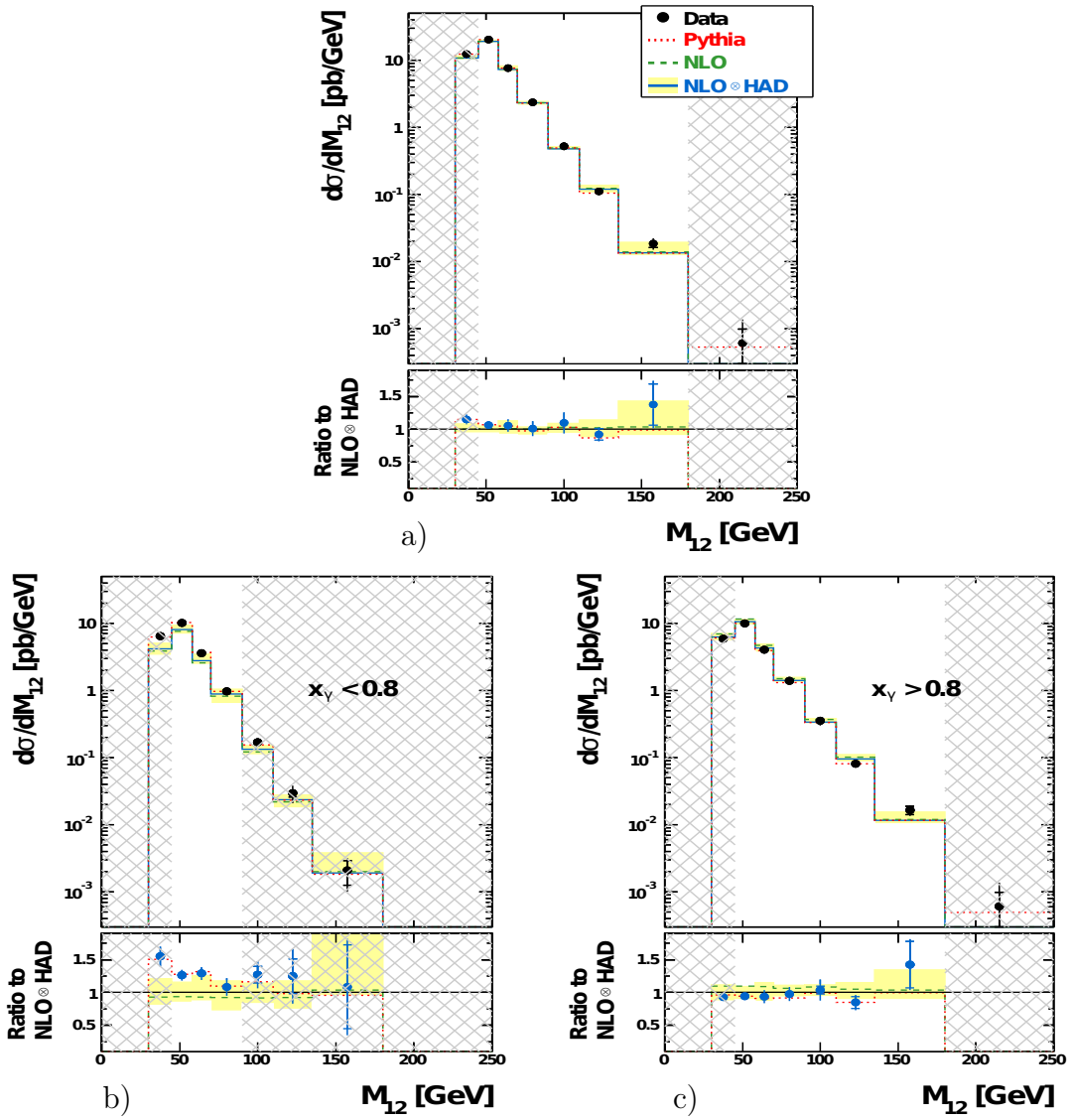

Figure 7.9: Cross section as a function of M_{12}, a) no condition on x_γ, b) for $x_\gamma < 0.8$, c) for $x_\gamma > 0.8$. For further details, see the caption to figure 7.1.

7.4 Differential Cross Section w.r.t. M_{12}

The dijet cross section as a function of the dijet invariant mass, M_{12} is presented in figure 7.9. The dashed regions are, as noted before, regions where the purity of the measurement is estimated to be $< 30\%$, excluded from the analysis (see section 7.1). The data are described by both predictions, NLO and Pythia, over almost four orders of magnitude. As expected from the observation in previous figures, the NLO prediction is below the data at small M_{12} for $x_\gamma < 0.8$, while there is a tendency for it to be above the data for $x_\gamma > 0.8$.

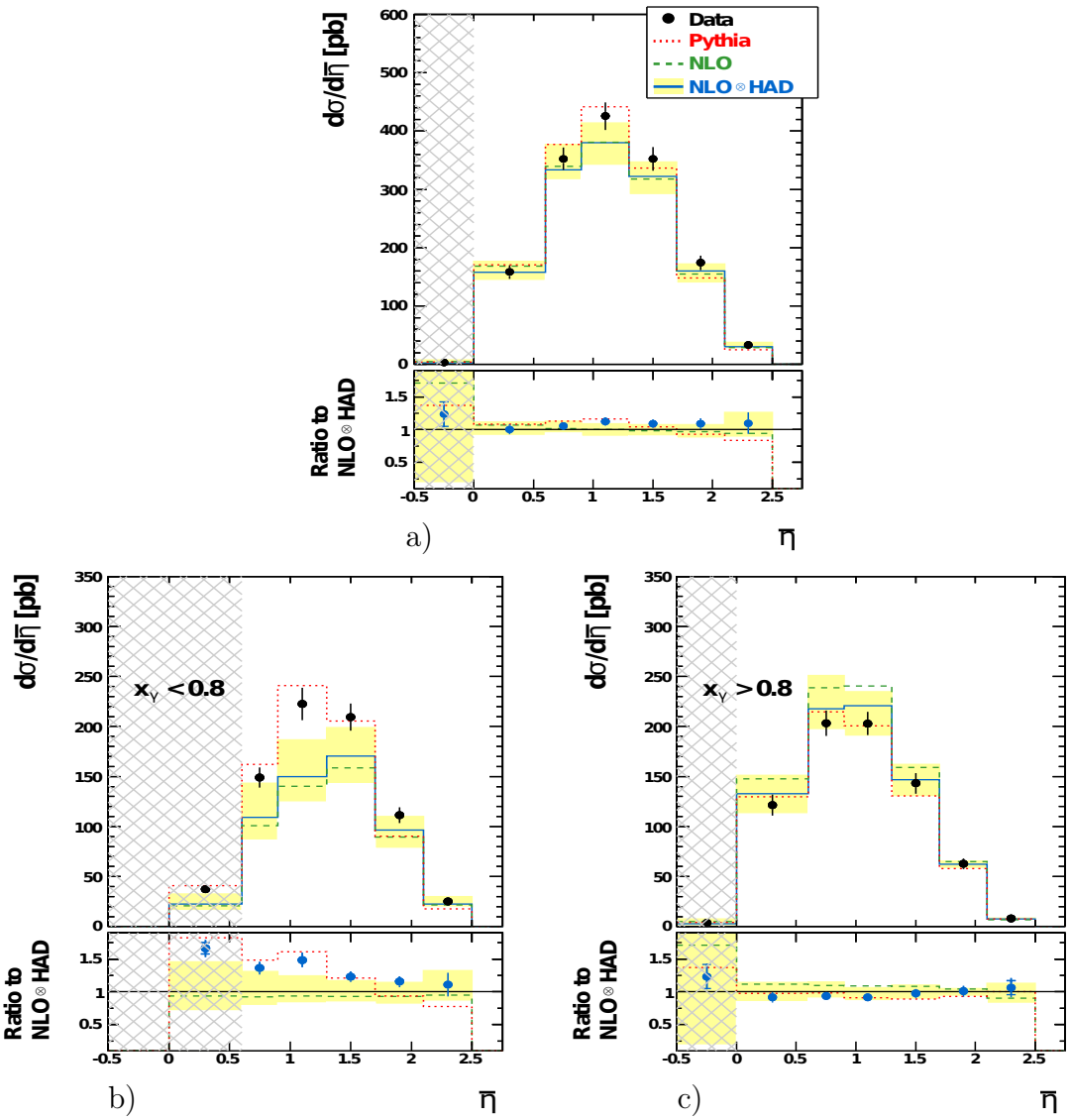

Figure 7.10: Cross section as a function of $\overline{\eta}$, a) no condition on x_γ, b) for $x_\gamma < 0.8$, c) for $x_\gamma > 0.8$. For further details, see the caption to figure 7.1.

7.5 Differential Cross Section w.r.t. $\overline{\eta}$

The dijet cross section as a function of $\overline{\eta}$ is presented in figure 7.10. The observable $\overline{\eta}$ is defined as:

$$\overline{\eta} = (\eta_{1\text{st}} + \eta_{2\text{nd}})/2.$$

Overall, the NLO and the Pythia predictions provide a good description of the data. For the regions of resolved enhanced and direct enhanced jet production similar deficiencies as in previous figures can be observed.

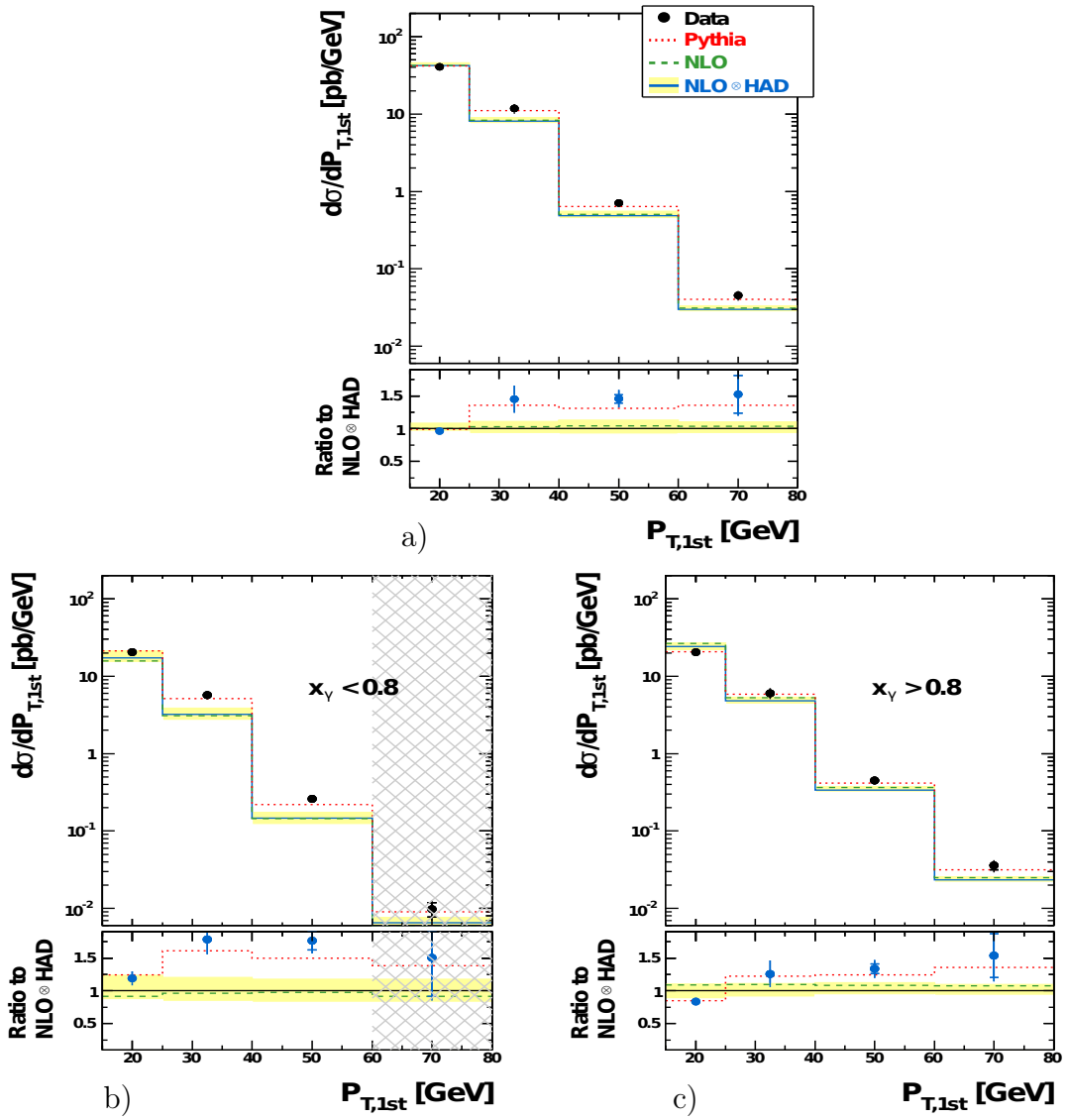

Figure 7.11: Cross section as a function of $P_{T,1st}$, a) no condition on x_γ, b) for $x_\gamma < 0.8$, c) for $x_\gamma > 0.8$. For further details, see the caption to figure 7.1.

7.6 Differential Cross Section w.r.t. $P_{T,1st}$

The dijet cross section as a function of $P_{T,1st}$ is presented in figure 7.11. The measurement for all three distributions extends in transverse energies up to 80 GeV. The $P_{T,1st}$ spectra are steeply falling, more steeply for resolved than for direct interactions, as expected. The Pythia predictions describe the data reasonably well for $x_\gamma < 0.8$ (with the maximal deviation of $\sim 20\%$ in one bin) and $x_\gamma > 0.8$. The NLO prediction fails to describe the $P_{T,1st}$ distribution, particularly in the resolved photon region; only the lowest $P_{T,1st}$ bin is described within the theory uncertainty.

The cross section of $P_{T,1st}$ divided into the different topological pseudorapidity regions (see section 7.3) is shown in figure 7.12. Figure b is completely excluded from the analysis due to the low purity (see section 7.1) in each bin. The Pythia predictions agree with the data within better than 20%, except for the second bin in

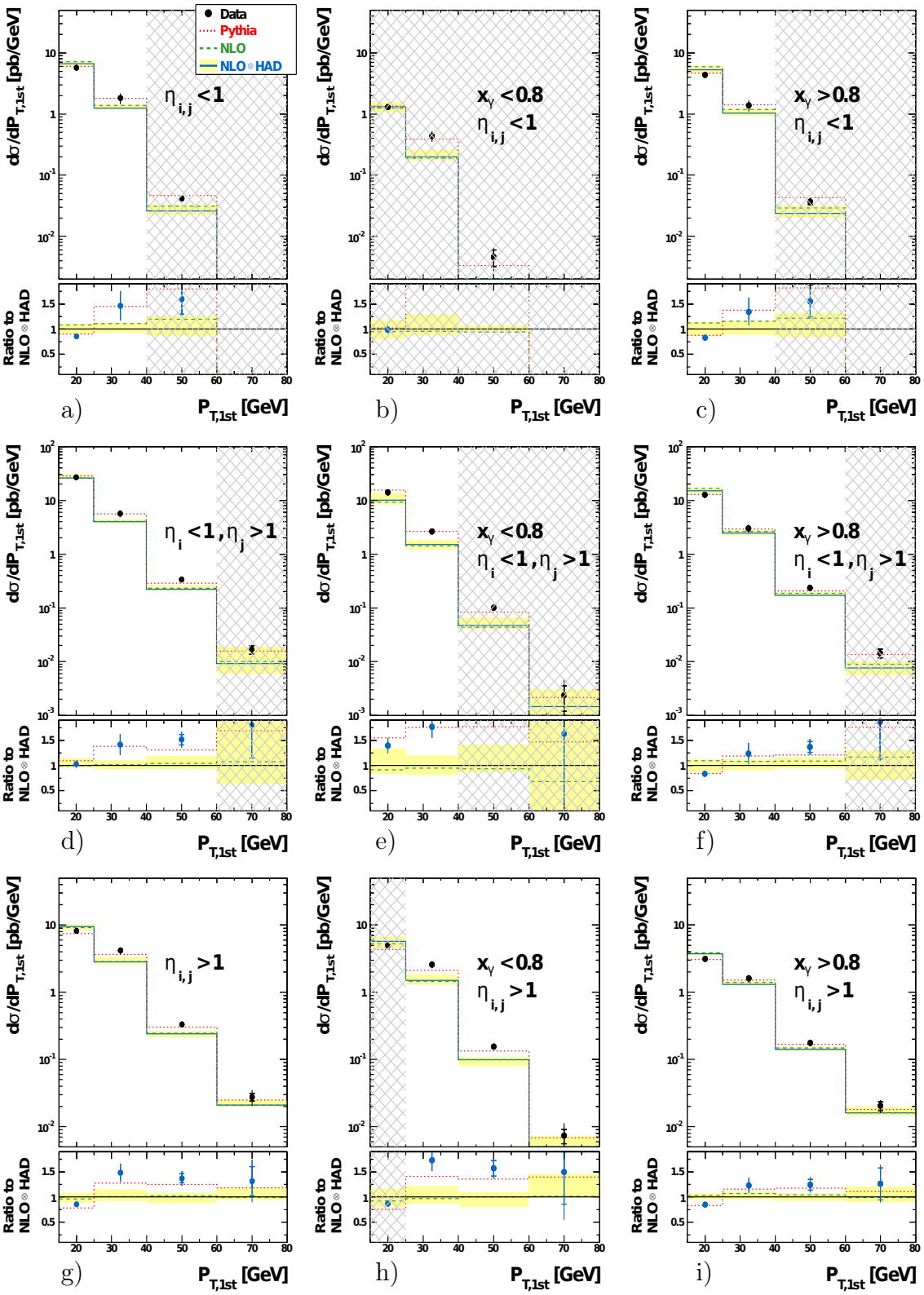

Figure 7.12: Cross sections as a function of $P_{T,1st}$ for different jet topologies in pesudorapidity $\eta_{i,j}$ and for $x_\gamma < 0.8$ and $x_\gamma > 0.8$. For further details, see the caption to figure 7.1.

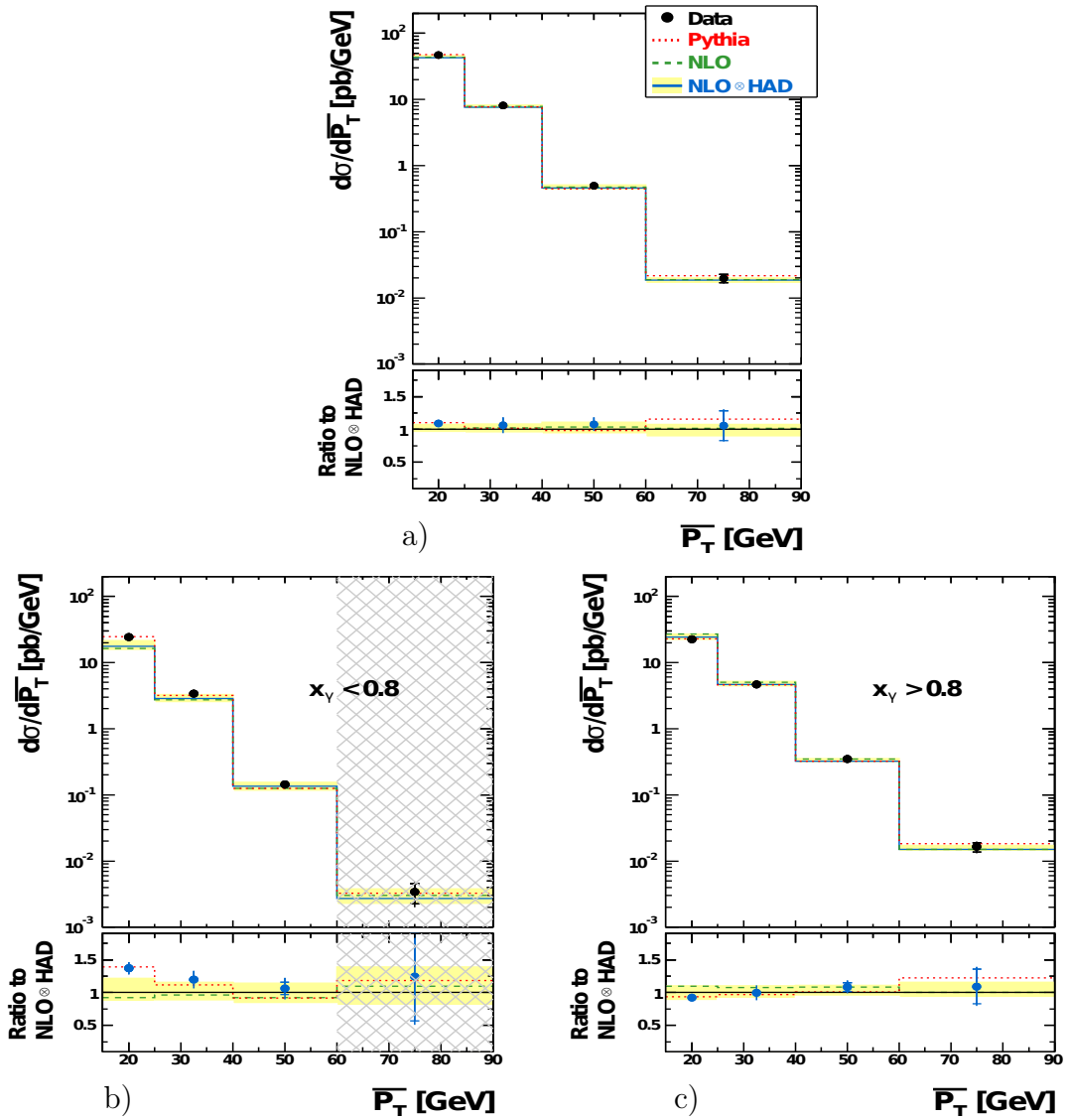

Figure 7.13: Cross section as a function of $\overline{P}_T$, a) no condition on x_γ, b) for $x_\gamma < 0.8$, c) for $x_\gamma > 0.8$. For further details, see the caption to figure 7.1.

figure h, where the maximal difference of 20% is observed. The NLO predictions show a similar failure in describing the resolved distributions in particular as was seen already before in the figure 7.11 without separation into topologies.

7.7 Differential Cross Section w.r.t. $\overline{P}_T$

The dijet cross section as a function of $\overline{P}_T$ is presented in figure 7.13. The observable $\overline{P}_T$ is defined as:

$$\overline{P}_T = (P_{T,1st} + P_{T,2nd})/2.$$

In all bins the Pythia prediction describes the data well. The data are also described by the NLO prediction within the uncertainty band, only the first bin of the resolved

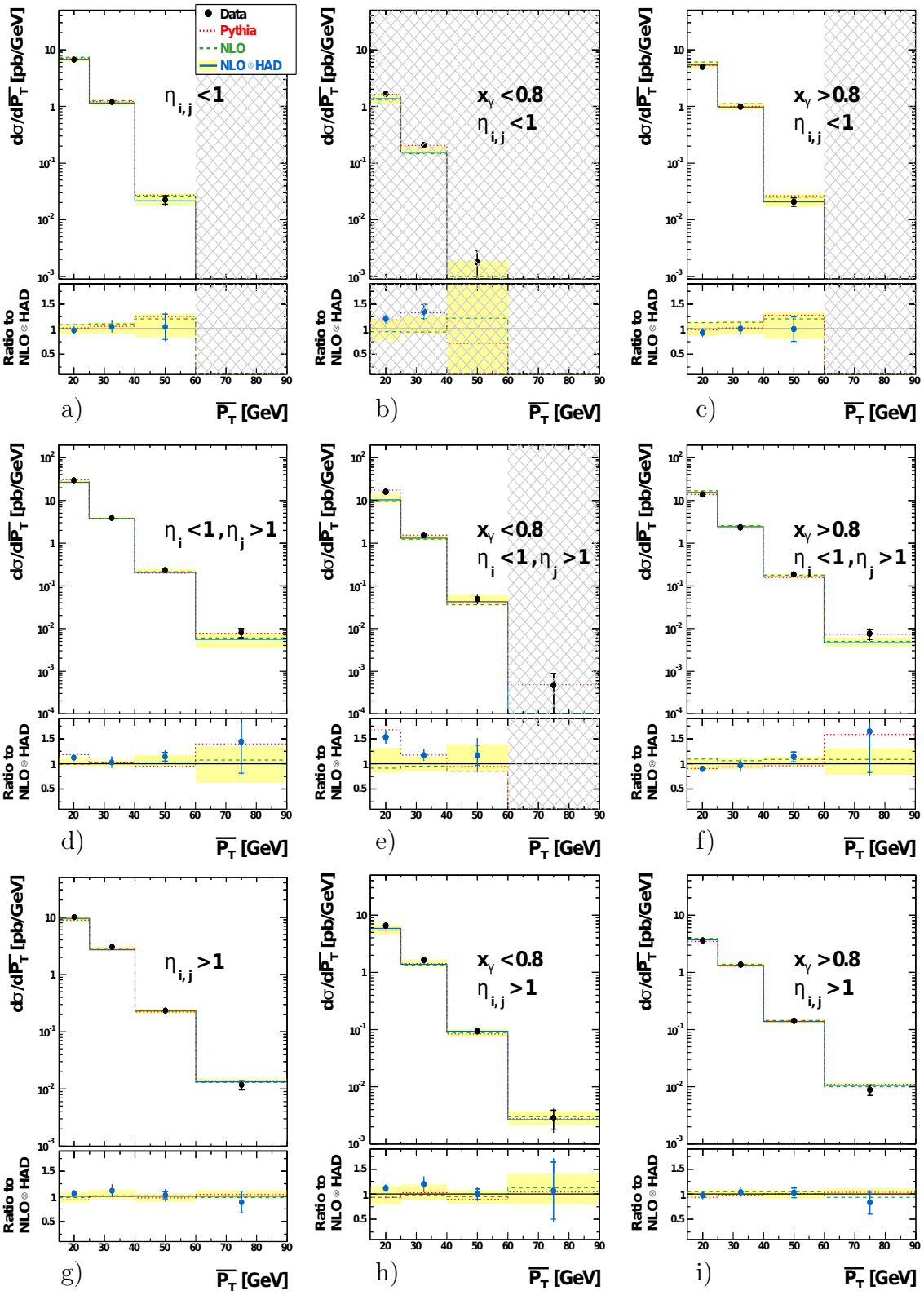

Figure 7.14: Cross sections as a function of $\overline{\mathrm{P}}_{\mathrm{T}}$ for different jet topologies in pesudorapidity $\eta_{i,j}$ and for $x_\gamma < 0.8$ and $x_\gamma > 0.8$. For further details, see the caption to figure 7.1.

photon region, $x_\gamma < 0.8$, is higher than the prediction by $\sim 40\%$.

The cross sections as a function of $\overline{P}_T$ are also presented for three different topologies (see section 7.3) in figure 7.14. In general the Pythia and NLO predictions provide a reasonable description of these detailed data. The tendency of the NLO prediction to undershoot the data in the resolved photon region is also visible here.

It is interesting to note that the NLO predictions of $\overline{P}_T$ show much batter agreement with the data than the predictions of $P_{T,1st}$.

7.8 Comparison of Different Photon and Proton PDFs

In the following we study the sensitivity of dijet photoproduction cross section predictions to the photon and proton PDFs. Figures 7.15 and 7.16 present comparisons to Pythia predictions using different PDF sets. The total cross section of each prediction is normalized to the result of the measurement (section 7) by a factor presented in the legend. In addition, the effect of multiple interactions was investigated by switching[1] it on and off.

The effect of multiple interactions has been investigated using the default Pythia prediction, generated with multiple interactions, and the prediction with the same photon and proton PDFs, but without multiple interactions. There is almost no effect from multiple interactions seen. Several predictions with the same photon PDF (SAS1D [SS95]) and different proton PDFs have also been investigated. There is a little difference in the distributions, which can also be seen in the normalization factors of the green, brown and light blue histograms. Moreover, the effect of using different photon PDFs has been studied. The green and orange histograms have the same proton PDF but different photon PDFs, while the blue one has different photon and proton PDFs. The prediction described by the orange line reflects the SAS2D photon PDF and it does not agree with the data. The difference in the SAS1D and SAS2D photon PDFs is that both treat the separation of pointlike (see section 2.3.4) and VDM (see section 2.3.2) parts by choosing an initial parameter M_0: $M_0 = 0.6$ GeV for SAS1D and $M_0 = 2$ GeV for SAS2D.

Overall the effect of multiple interactions shows almost no impact on the distributions. The prediction with changed photon PDF but with settled proton PDF (orange line) shows the largest difference to the data.

[1] In the legend of figures 7.15 and 7.16 MI means multiple interactions switched on, noMI - off.

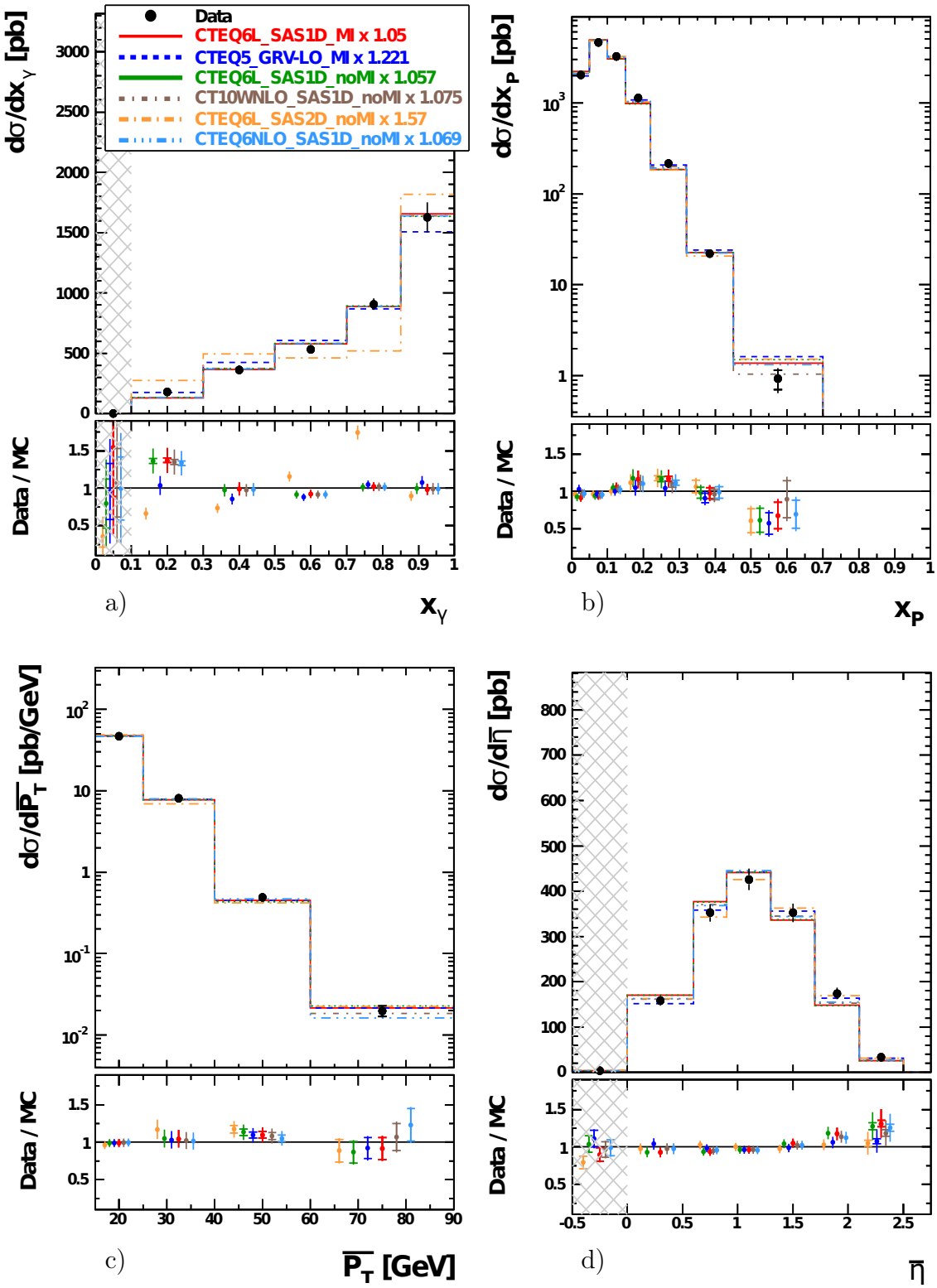

Figure 7.15: Predictions of dijet cross sections as a function of a) x_γ, b) x_P, c) $\overline{P}_T$ and d) $\overline{\eta}$ by the Pythia generator, using different photon and proton PDFs and with (MI) and without (noMI) multiple interactions, are compared to the data. Each Pythia prediction is normalized to the measured total dijet photoproduction cross section. The normalized factors are given in the legend as well the respective proton and photon PDFs. In the ration plots below the data divided by each Pythia prediction is presented in a corresponding color bullet. The inner (outer) error bar indicates the statistical (total) error of the data. The dashed regions in figure a) and d) are regions where the purity of the measurement is estimated to be $< 30\%$, and they are excluded from the analysis (see section 7.1).

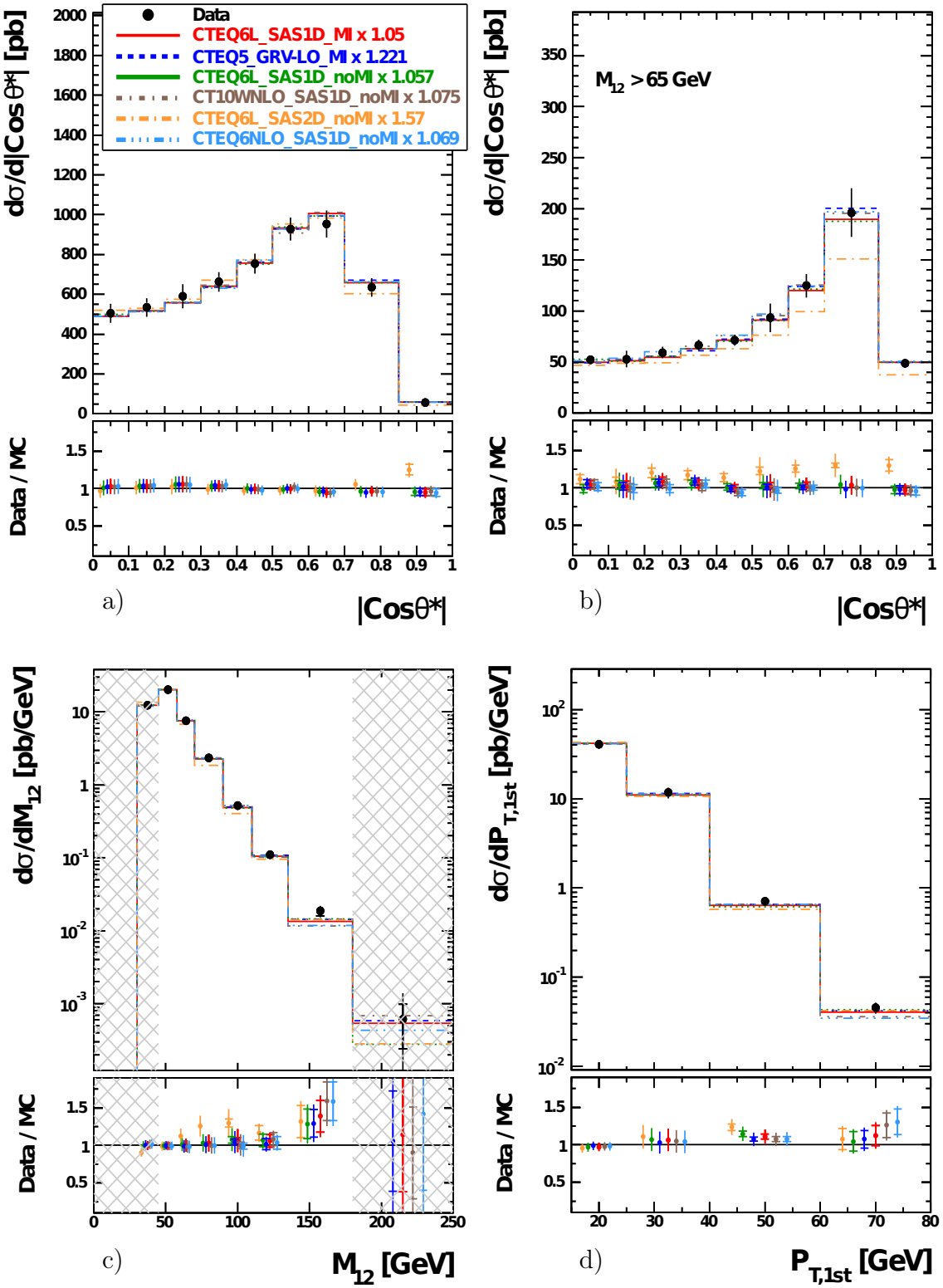

Figure 7.16: Predictions of dijet cross sections as a function of a) $|\cos\theta^*|$, b) $|\cos\theta^*|$ with $M_{12} > 65$ GeV, c) M_{12} and d) $P_{T,1st}$ by the Pythia generator, using different photon and proton PDFs and with (MI) and without (noMI) multiple interactions, are compared to the data. Each Pythia prediction is normalized to the measured total dijet photoproduction cross section. The normalized factors are given in the legend as well the respective proton and photon PDFs. In the ration plots below the data divided by each Pythia prediction is presented in a corresponding color bullet. The inner (outer) error bar indicates the statistical (total) error of the data. The dashed regions in figure c) are regions where the purity of the measurement is estimated to be $< 30\%$, and they are excluded from the analysis (see section 7.1).

CHAPTER 8

SUMMARY

Production of high P_T dijets in photoproduction at HERA in the γp center-of-mass energy $101 < W_{\gamma p} < 302$ GeV was studied. The data set used corresponds to the HERA II 2006 e^+p running period, which corresponds to a total integrated luminosity of 92.4 pb^{-1}. This has improved the statistical uncertainty of the measurement compared to previous HERA I photoproduction dijet cross section measurements. Measurements are presented for the total and single differential cross sections in the kinematic range of the squared momentum transfer $Q^2 < 4.0$ GeV^2 and inelasticity $0.1 < y < 0.9$. In addition, the jet phase space is defined by the following requirements on the two leading jets in the event: the transverse momenta $P_{T,1st,2nd} > 15.0$ GeV, the pseudorapidities $-0.5 < \eta_{1st,2nd} < 2.5$ and the invariant mass of the two jets $M_{12} > 40.0$ GeV.

The measured cross sections are presented as a functions of the following observables: $|\cos\theta^*|$, x_γ, x_P, M_{12}, $\overline{\eta}$, $\overline{P}_T$ and $P_{T,1st}$. The data are overall well described by both Pythia and NLO calculations. It was shown that for the resolved photon enhanced region, $x_\gamma < 0.8$, the cross section as a function of $|\cos\theta^*|$ rises more rapidly than that for the direct photon enhanced region, $x_\gamma > 0.8$, due to the dominating gluon propagator in resolved processes. Also the dependence of the cross sections on the pseudorapidities of the dijets has been studied. For this three topology regions of the dijets pseudorapidities are presented.

In addition, an application of different PDF sets was investigated. Pythia predictions have been shown to depend insignificantly on the presence or absence of multiple interactions and rather little on the choice of recent proton PDFs. The photon PDFs, GRV-LO and SAS1D provide a reasonable to good description of the data, while SAS2D leads to significant deficiencies.

These data provide measurements at considerably higher scales than $\gamma^*\gamma$ measurements at LEP and they are very detailed, thus one expects them to be useful in new determinations of the photon PDFs.

APPENDIX A

TABLES OF THE RESULTS

This appendix contains tables of differential dijet cross sections and their uncertainties. The phase space of these measurements is presented in table 5.2. The individual contributions to the total uncertainty δ_{tot} and their column labels are:

- δ_{stat}: statistical error of the data,
- δ_{HFS}: hadronic energy scale error,
- δ_{mod}: model uncertainty of the corrections for detector effects,
- δ_{trig}: uncertainty of the trigger efficiency,
- δ_{DIS}: uncertainty from the DIS background subtraction,
- $\mathrm{C_{had}}$: hadronization correction factor.

Global contributions from the LAr noise uncertainty (0.6%) and the luminosity measurements (2.6%) are also included into the total uncertainty. All individual contributions are added up in quadrature.

The cross sections as a function of $\mathrm{x_P}$, $\overline{\mathrm{P}}_{\mathrm{T}}$ and $\mathrm{P_{T,1st}}$ are also measured for three different topologies of the final state: the case where both jets are in the "backward" direction ($\eta_{1,2} < 1$), where both jets are in the "forward" direction ($\eta_{1,2} > 1$), and where one of the jets is in the "forward" ($\eta_i > 1$) and the other one is in the "backward" ($\eta_j < 1$) direction.

$\lvert\cos\theta^*\rvert$	$\frac{d\sigma}{d\lvert\cos\theta^*\rvert}$ [pb]	δ_{stat} [%]	δ_{tot} [%]	δ_{HFS} [%]	δ_{mod} [%]	δ_{trig} [%]	δ_{DIS} [%]	C_{had}
$x_\gamma < 0.8$								
0.00 - 0.10	230.74	2.01	10.80	4.41	8.73	2.92	0.59	1.02
0.10 - 0.20	245.56	2.03	8.82	4.64	5.99	2.90	0.29	1.04
0.20 - 0.30	266.22	1.94	11.01	4.82	8.82	2.91	0.30	1.08
0.30 - 0.40	309.13	1.80	7.26	4.47	3.67	2.86	0.09	1.04
0.40 - 0.50	366.61	1.76	6.52	4.63	1.42	2.85	0.13	1.07
0.50 - 0.60	475.00	1.62	6.11	4.27	0.96	2.78	0.24	1.08
0.60 - 0.70	493.20	1.63	8.84	4.45	6.36	2.70	0.35	1.09
0.70 - 0.85	339.86	1.70	12.08	4.82	10.26	2.45	0.76	1.10
$x_\gamma > 0.8$								
0.00 - 0.10	273.59	2.05	8.86	3.35	7.16	2.00	0.02	0.92
0.10 - 0.20	288.76	2.02	9.20	3.35	7.58	2.00	0.03	0.92
0.20 - 0.30	324.48	1.92	9.61	3.48	8.04	2.00	0.11	0.93
0.30 - 0.40	354.06	1.86	8.01	3.40	6.10	2.00	0.09	0.92
0.40 - 0.50	387.23	1.78	7.79	3.37	5.87	2.00	0.06	0.91
0.50 - 0.60	452.98	1.72	8.54	3.45	6.79	2.00	0.10	0.92
0.60 - 0.70	460.0.4	1.75	5.96	3.61	2.75	2.00	0.05	0.92
0.70 - 0.85	295.57	1.84	5.73	3.73	1.94	2.00	0.12	0.90
0.85 - 1.00	28.52	6.60	16.05	3.35	1.38	2.00	0.24	0.89
$0.0 < x_\gamma < 1.0$								
0.00 - 0.10	504.33	1.45	9.63	3.84	7.88	2.42	0.26	0.96
0.10 - 0.20	534.32	1.44	8.84	3.95	6.84	2.41	0.12	0.98
0.20 - 0.30	590.70	1.37	10.13	4.09	8.39	2.41	0.07	0.99
0.30 - 0.40	663.18	1.30	7.43	3.90	4.97	2.40	0.03	0.97
0.40 - 0.50	753.84	1.25	6.69	3.98	3.70	2.41	0.09	0.98
0.50 - 0.60	927.98	1.18	6.16	3.87	2.82	2.40	0.17	1.00
0.60 - 0.70	953.23	1.20	7.25	4.04	4.62	2.36	0.20	1.01
0.70 - 0.85	635.42	1.25	7.37	4.31	4.59	2.24	0.46	1.01
0.85 - 1.00	56.13	4.66	7.45	4.38	0.65	2.06	0.14	1.02

Table A.1: Single differential dijet cross section measured as function of $|\cos\theta^*|$.

$\lvert\cos\theta^*\rvert$	$\frac{d\sigma}{d\lvert\cos\theta^*\rvert}$ [pb]	δ_{stat} [%]	δ_{tot} [%]	δ_{HFS} [%]	δ_{mod} [%]	δ_{trig} [%]	δ_{DIS} [%]	C_{had}
$x_\gamma < 0.8$ and $M_{12} > 65.0$ GeV								
0.00 - 0.10	17.58	7.48	10.61	5.66	2.48	2.50	2.08	1.05
0.10 - 0.20	16.90	7.61	16.00	5.63	12.14	2.56	2.08	0.99
0.20 - 0.30	20.50	6.95	11.22	4.98	6.07	2.57	1.15	1.08
0.30 - 0.40	22.98	6.48	9.87	4.99	3.84	2.53	1.24	1.05
0.40 - 0.50	26.60	6.07	10.46	5.48	5.27	2.53	0.48	1.04
0.50 - 0.60	39.29	5.14	13.15	4.35	10.65	2.52	0.02	1.04
0.60 - 0.70	49.80	4.61	8.18	4.99	2.69	2.36	0.04	1.05
0.70 - 0.85	88.61	3.06	13.65	4.69	11.86	2.18	0.12	1.12
$x_\gamma > 0.8$ and $M_{12} > 65.0$ GeV								
0.00 - 0.10	34.62	5.83	8.16	3.69	2.66	2.00	0.10	0.96
0.10 - 0.20	36.01	5.87	16.11	3.54	14.16	2.00	0.06	0.94
0.20 - 0.30	38.80	5.54	10.05	3.59	6.75	2.00	0.25	0.98
0.30 - 0.40	43.33	5.30	8.69	3.74	4.65	2.00	0.07	0.96
0.40 - 0.50	44.79	5.05	7.30	3.81	1.20	2.00	0.08	0.93
0.50 - 0.60	54.11	4.55	16.94	3.67	15.52	2.00	0.19	0.93
0.60 - 0.70	75.01	3.86	11.32	3.89	9.29	2.00	0.06	0.94
0.70 - 0.85	107.73	2.72	11.18	4.04	9.45	2.00	0.20	0.91
0.85 - 1.00	25.29	6.79	20.04	3.22	18.26	2.00	0.26	0.91
$0.0 < x_\gamma < 1.0$ and $M_{12} > 65.0$ GeV								
0.00 - 0.10	52.20	4.61	7.37	4.35	0.94	2.17	0.77	0.98
0.10 - 0.20	52.90	4.68	15.35	4.22	13.52	2.18	0.71	0.95
0.20 - 0.30	59.30	4.13	9.52	4.07	6.52	2.20	0.24	1.01
0.30 - 0.40	66.31	4.11	8.15	4.17	4.37	2.22	0.38	0.99
0.40 - 0.50	71.39	3.89	7.42	4.44	2.72	2.20	0.23	0.97
0.50 - 0.60	93.40	3.41	14.89	3.96	13.47	2.22	0.10	0.97
0.60 - 0.70	124.80	2.96	9.18	4.33	6.66	2.15	0.02	0.99
0.70 - 0.85	196.33	2.03	12.11	4.34	10.54	2.08	0.66	1.00
0.85 - 1.00	48.63	4.91	8.52	3.95	4.30	2.04	1.51	1.03

Table A.2: Single differential dijet cross section measured as function of $|\cos\theta^*|$ with $M_{12} > 65.0$ GeV.

x_γ	$\frac{d\sigma}{dx_\gamma}$ [pb]	δ_{stat} [%]	δ_{tot} [%]	δ_{HFS} [%]	δ_{mod} [%]	δ_{trig} [%]	δ_{DIS} [%]	$\mathrm{C}_{\mathrm{had}}$
$x_{\mathrm{P}} < 0.1$								
0.50 - 0.70	294.37	1.48	7.93	4.19	5.51	2.01	0.94	1.07
0.70 - 0.85	555.03	1.25	5.98	4.00	2.48	2.01	0.44	1.18
0.85 - 1.00	1047.98	0.91	7.15	3.22	5.30	2.00	0.06	0.85
$x_{\mathrm{P}} > 0.1$								
0.10 - 0.30	162.00	2.07	11.81	5.57	8.82	4.00	1.57	1.06
0.30 - 0.50	220.72	1.57	7.37	4.82	2.12	4.00	0.18	1.04
0.50 - 0.70	239.27	1.50	8.98	4.45	6.82	4.00	0.26	1.08
0.70 - 0.85	352.71	1.43	7.62	4.14	5.20	2.00	0.08	1.21
0.85 - 1.00	579.89	1.25	8.48	3.70	6.69	2.00	0.04	0.88
$0.0 < x_{\mathrm{P}} < 1.0$								
0.10 - 0.30	181.50	1.97	12.17	5.57	9,31	4.00	1.54	1.06
0.30 - 0.50	364.24	1.27	8.67	4.86	5.08	4.00	0.00	1.03
0.50 - 0.70	533.64	1.06	5.66	4.31	0.02	2.00	0.64	1.07
0.70 - 0.85	907.74	0.95	5.43	4.05	0.50	2.00	0.30	1.19
0.85 - 1.00	1627.87	0.73	7.58	3.39	5.79	2.00	0.06	0.86

Table A.3: Single differential dijet cross section measured as function of x_γ.

x_{P}	$\frac{d\sigma}{dx_{\mathrm{P}}}$ [pb]	δ_{stat} [%]	δ_{tot} [%]	δ_{HFS} [%]	δ_{mod} [%]	δ_{trig} [%]	δ_{DIS} [%]	$\mathrm{C}_{\mathrm{had}}$
$x_\gamma < 0.8$								
0.05 - 0.10	2224.22	1.04	8.32	4.34	5.89	2.54	0.46	1.07
0.10 - 0.15	1850.74	1.12	7.04	4.61	3.30	2.89	0.01	1.09
0.15 - 0.22	694.57	1.47	11.05	4.89	8.86	3.08	0.35	1.07
0.22 - 0.32	130.72	2.77	12.09	4.98	9.74	3.10	1.25	1.06
0.32 - 0.45	9.86	8.61	12.43	6.72	2.94	3.03	3.06	0.93
0.45 - 0.70	0.56	29.24	36.84	7.77	8.39	2.95	18.84	1.25
$x_\gamma > 0.8$								
0.00 - 0.05	1470.53	1.39	6.90	3.22	4.84	2.00	0.12	0.89
0.05 - 0.10	2388.91	1.01	5.61	3.40	2.66	2.00	0.08	0.91
0.10 - 0.15	1365.58	1.38	8.52	3.71	6.71	2.00	0.05	0.93
0.15 - 0.22	439.49	2.03	8.73	3.80	6.77	2.00	0.02	0.95
0.22 - 0.32	84.76	3.97	18.36	3.72	5.34	2.00	0.16	0.97
0.32 - 0.45	12.21	9.72	12.35	4.71	4.90	2.00	0.14	0.99
0.45 - 0.70	0.38	41.30	45.66	8.97	16.95	2.00	0.00	0.89
$0.0 < x_\gamma < 1.0$								
0.00 - 0.05	2032.22	1.21	5.96	3.54	3.05	2.03	0.50	0.93
0.05 - 0.10	4613.13	0.73	5.53	3.86	1.46	2.27	0.26	0.99
0.10 - 0.15	3216.32	0.87	5.81	4.23	0.95	2.52	0.03	1.02
0.15 - 0.22	1134.05	1.20	10.06	4.47	8.05	2.67	0.21	1.02
0.22 - 0.32	215.47	2.29	10.24	4.48	8.00	2.67	0.70	1.02
0.32 - 0.45	22.07	6.61	10.35	5.61	4.02	2.47	1.29	0.96
0.45 - 0.70	0.93	24.12	30.51	8.25	11.84	2.57	11.25	1.04

Table A.4: Single differential dijet cross section measured as function of x_{P}.

x_{P}	$\frac{d\sigma}{dx_{\mathrm{P}}}$ [pb]	δ_{stat} [%]	δ_{tot} [%]	δ_{HFS} [%]	δ_{mod} [%]	δ_{trig} [%]	δ_{DIS} [%]	$\mathrm{C}_{\mathrm{had}}$
$x_\gamma < 0.8$ and $\eta_{1,2} < 1$								
0.05 - 0.10	104.00	4.63	9.86	3.95	6.86	2.20	0.53	1.04
$x_\gamma > 0.8$ and $\eta_{1,2} < 1$								
0.00 - 0.05	1035.95	1.63	9.31	3.27	7.83	2.00	0.14	0.87
0.05 - 0.10	262.12	2.94	10.41	3.55	48.68	2.00	0.14	0.92
0.10 - 0.15	6.12	20.52	21.35	4.75	0.29	2.00	0.53	0.94
$0.0 < x_\gamma < 1.0$ and $\eta_{1,2} < 1$								
0.00 - 0.05	1325.70	1.46	8.26	3.40	6.50	2.01	0.50	0.91
0.05 - 0.10	366.13	2.48	9.92	3.67	8.16	2.06	0.25	0.95
0.10 - 0.15	7.36	19.23	22.61	4.42	10.45	2.00	0.71	0.97

Table A.5: Single differential dijet cross section measured as function of x_{P} with $\eta_{1,2} < 1$.

x_{P}	$\frac{d\sigma}{dx_{\mathrm{P}}}$ [pb]	δ_{stat} [%]	δ_{tot} [%]	δ_{HFS} [%]	δ_{mod} [%]	δ_{trig} [%]	δ_{DIS} [%]	$\mathrm{C}_{\mathrm{had}}$
$x_\gamma < 0.8$ and $\eta_i < 1, \eta_j > 1$								
0.05 - 0.10	1957.60	1.13	10.07	4.44	8.12	2.53	0.51	1.07
0.10 - 0.15	1148.13	1.52	6.70	4.63	2.39	2.73	0.32	1.10
0.15 - 0.22	173.13	3.13	14.28	4.84	12.48	2.65	0.19	1.09
0.22 - 0.32	13.08	9.39	23.06	4.82	20.15	2.43	0.59	1.12
0.32 - 0.45	0.72	30.04	42.56	6.15	11.87	2.00	4.06	0.96
$x_\gamma > 0.8$ and $\eta_i < 1, \eta_j > 1$								
0.00 - 0.05	434.32	2.66	5.50	3.08	1.36	2.00	0.07	0.91
0.05 - 0.10	1975.53	1.13	5.28	3.39	1.80	2.00	0.08	0.91
0.10 - 0.15	884.44	1.78	8.23	3.86	6.15	2.00	0.03	0.93
0.15 - 0.22	152.12	3.49	13.33	4.15	11.68	2.00	0.10	0.92
0.22 - 0.32	16.80	8.57	11.07	4.12	4.48	2.00	0.52	0.96
0.32 - 0.45	2.18	23.19	24.05	1.39	5.06	2.00	1.15	0.98
0.45 - 0.70	0.07	104.67	111.78	35.58	16.16	2.00	0.00	0.75
$0.0 < x_\gamma < 1.0$ and $\eta_i < 1, \eta_j > 1$								
0.00 - 0.05	706.89	2.14	6.14	3.75	2.60	2.05	0.52	0.98
0.05 - 0.10	3933.13	0.80	6.24	3.92	3.14	2.27	0.29	0.99
0.10 - 0.15	2032.57	1.15	5.94	4.29	1.32	2.42	0.20	1.03
0.15 - 0.22	325.24	2.33	13.61	4.52	12.11	2.35	0.15	1.02
0.22 - 0.32	29.88	6.33	10.59	4.43	6.30	2.19	0.03	1.03
0.32 - 0.45	2.90	20.07	20.63	2.58	0.86	2.01	1.87	0.98
0.45 - 0.70	0.07	104.67	114.03	35.58	16.16	2.00	22.55	1.0

Table A.6: Single differential dijet cross section measured as function of x_{P} with $\eta_i < 1, \eta_j > 1$.

x_{P}	$\frac{d\sigma}{dx_{\mathrm{P}}}$ [pb]	δ_{stat} [%]	δ_{tot} [%]	δ_{HFS} [%]	δ_{mod} [%]	δ_{trig} [%]	δ_{DIS} [%]	$\mathrm{C}_{\mathrm{had}}$
$x_\gamma < 0.8$ and $\eta_{1,2} > 1$								
0.10 - 0.15	693.09	1.64	7.54	4.58	3.95	3.10	0.38	1.06
0.15 - 0.22	516.25	1.67	10.47	4.91	8.02	3.20	0.49	1.06
0.22 - 0.32	117.46	2.89	11.48	5.00	8.89	3.16	1.31	1.05
0.32 - 0.45	9.19	8.81	12.68	6.75	2.91	3.09	3.44	0.93
0.45 - 0.70	0.56	29.24	36.34	8.39	8.80	3.09	17.35	1.23
$x_\gamma > 0.8$ and $\eta_{1,2} > 1$								
0.05 - 0.10	151.58	3.74	7.57	3.28	4.55	2.00	0.04	0.95
0.10 - 0.15	475.55	2.19	9.38	3.44	7.71	2.00	0.07	0.94
0.15 - 0.22	287.03	2.50	6.97	3.61	4.18	2.00	0.02	0.96
0.22 - 0.32	67.99	4.48	10.24	3.60	7.74	2.00	0.06	0.97
0.32 - 0.45	10.01	10.71	14.04	5.08	6.69	2.00	0.08	0.99
0.45 - 0.70	0.31	45.18	49.21	8.96	16.99	2.00	0.00	0.91
$0.0 < x_\gamma < 1.0$ and $\eta_{1,2} > 1$								
0.05 - 0.10	312.08	2.51	8.87	3.38	6.85	2.47	0.04	0.99
0.10 - 0.15	1168.64	1.32	5.85	4.12	0.80	2.66	0.20	1.01
0.15 - 0.22	803.28	1.40	9.03	4.44	6.65	2.77	0.32	1.03
0.22 - 0.32	185.45	2.46	10.67	4.48	8.47	2.73	0.81	1.02
0.32 - 0.45	19.20	7.00	11.16	5.88	4.88	2.53	1.17	0.96
0.45 - 0.70	0.87	24.77	31.05	8.59	11.73	2.53	11.15	1.05

Table A.7: Single differential dijet cross section measured as function of x_{P} with $\eta_{1,2} > 1$.

M_{12} [GeV]	$\frac{d\sigma}{dM_{12}}$ [pb/GeV]	δ_{stat} [%]	δ_{tot} [%]	δ_{HFS} [%]	δ_{mod} [%]	δ_{trig} [%]	δ_{DIS} [%]	C_{had}
$x_\gamma < 0.8$								
45.0 - 58.0	10.17	0.97	6.07	4.51	0.29	2.78	0.09	1.07
58.0 - 70.0	3.60	1.69	7.25	4.94	3.31	2.53	0.24	1.08
70.0 - 90.0	0.96	2.52	11.93	5.19	9.77	2.37	0.47	1.08
$x_\gamma > 0.8$								
45.0 - 58.0	9.91	1.01	6.19	3.41	3.73	2.0	0.07	0.91
58.0 - 70.0	4.03	1.63	10.75	3.90	9.27	2.00	0.06	0.92
70.0 - 90.0	1.38	2.13	10.89	3.80	9.37	2.00	0.09	0.94
90.0 - 110.0	0.35	4.17	14.71	4.48	12.92	2.00	0.13	0.92
110.0 - 135.0	0.082	8.06	11.68	4.57	6.17	2.00	0.38	0.95
135.0 - 180.0	0.017	14.32	18.00	5.85	8.51	2.00	0.69	0.96
$0.0 < x_\gamma < 1.0$								
45.0 - 58.0	20.08	0.70	5.81	3.97	1.98	2.39	0.08	0.99
58.0 - 70.0	7.63	1.17	8.68	4.39	6.46	2.25	0.15	0.99
70.0 - 90.0	2.34	1.63	11.19	4.37	9.53	2.15	0.25	1.00
90.0 - 110.0	0.52	3.43	14.17	4.41	12.55	2.09	0.09	0.97
110.0 - 135.0	0.11	6.91	9.58	5.25	2.00	2.07	0.51	0.98
135.0 - 180.0	0.019	13.47	18.69	5.36	11.27	2.05	0.38	0.95

Table A.8: Single differential dijet cross section measured as function of M_{12}.

$\overline{\eta}$	$\frac{d\sigma}{d\overline{\eta}}$ [pb]	δ_{stat} [%]	δ_{tot} [%]	δ_{HFS} [%]	δ_{mod} [%]	δ_{trig} [%]	δ_{DIS} [%]	$\mathrm{C}_{\mathrm{had}}$
$x_\gamma < 0.8$								
0.6 - 0.9	148.88	1.76	6.70	4.51	2.84	2.22	0.76	1.08
0.9 - 1.3	222.64	1.15	7.27	4.53	4.06	2.58	0.36	1.07
1.3 - 1.7	209.29	1.14	6.44	4.55	1.68	2.97	0.17	1.07
1.7 - 2.1	111.41	1.49	7.03	4.74	2.48	3.22	0.57	1.08
2.1 - 2.5	25.08	3.27	16.11	5.02	14.27	3.30	1.03	1.05
$x_\gamma > 0.8$								
0.0 - 0.6	121.33	1.37	8.60	3.36	7.00	2.00	0.48	0.90
0.6 - 0.9	203.43	1.42	6.26	3.49	3.63	2.00	0.12	0.91
0.9 - 1.3	202.95	1.23	5.73	3.51	2.67	2.00	0.10	0.92
1.3 - 1.7	143.13	1.48	7.14	3.51	5.00	2.00	0.06	0.93
1.7 - 2.1	62.76	2.30	8.12	3.57	6.01	2.00	0.03	0.96
2.1 - 2.5	8.18	6.88	11.85	4.30	7.91	2.00	0.03	1.11
$0.0 < x_\gamma < 1.0$								
0.0 - 0.6	158.59	1.22	7.35	3.57	5.25	2.02	0.58	0.94
0.6 - 0.9	352.31	1.11	5.46	3.92	0.90	2.10	0.38	0.98
0.9 - 1.3	425.58	0.84	5.57	4.05	0.85	2.30	0.22	1.00
1.3 - 1.7	352.42	0.91	5.78	4.13	1.02	2.58	0.09	1.02
1.7 - 2.1	174.17	1.26	7.08	4.32	3.75	2.78	0.35	1.03
2.1 - 2.5	33.26	2.99	14.54	4.85	12.71	2.98	0.77	1.06

Table A.9: Single differential dijet cross section measured as function of $\overline{\eta}$.

$P_{T,1st}$ [GeV]	$\frac{d\sigma}{dP_{T,1st}}$ [pb/GeV]	δ_{stat} [%]	δ_{tot} [%]	δ_{HFS} [%]	δ_{mod} [%]	δ_{trig} [%]	δ_{DIS} [%]	C_{had}
$x_\gamma < 0.8$								
15.0 - 25.0	20.41	0.81	8.72	4.32	6.42	2.78	0.31	1.09
25.0 - 40.0	5.71	1.05	12.68	5.01	10.92	2.77	0.03	1.04
40.0 - 60.0	0.26	4.05	8.50	5.24	3.15	2.51	2.09	1.02
$x_\gamma > 0.8$								
15.0 - 25.0	20.30	0.88	4.94	3.18	1.27	2.00	0.08	0.91
25.0 - 40.0	6.02	1.04	16.00	3.83	15.11	2.00	0.08	0.91
40.0 - 60.0	0.45	3.31	9.22	4.37	6.56	2.00	0.10	0.92
60.0 - 80.0	0.036	11.81	17.99	4.52	12.33	2.00	0.20	0.93
$0.0 < x_\gamma < 1.0$								
15.0 - 25.0	40.71	0.60	5.89	3.75	2.58	2.39	0.19	1.00
25.0 - 40.0	11.73	0.74	14.29	4.40	13.07	2.37	0.03	0.97
40.0 - 60.0	0.71	2.57	8.36	4.69	5.31	2.19	0.71	0.96
60.0 - 80.0	0.046	10.37	14.23	4.91	7.12	2.10	2.82	0.97

Table A.10: Single differential dijet cross section measured as function of $P_{T,1st}$.

$P_{T,1st}$ [GeV]	$\frac{d\sigma}{dP_{T,1st}}$ [pb/GeV]	δ_{stat} [%]	δ_{tot} [%]	δ_{HFS} [%]	δ_{mod} [%]	δ_{trig} [%]	δ_{DIS} [%]	C_{had}
$x_\gamma > 0.8$ and $\eta_{1,2} < 1$								
15.0 - 25.0	4.40	1.97	6.96	3.03	4.84	2.00	0.09	0.89
25.0 - 40.0	1.39	2.14	20.28	3.69	19.52	2.00	0.21	0.87
$0.0 < x_\gamma < 1.0$ and $\eta_{1,2} < 1$								
15.0 - 25.0	5.70	1.73	5.76	3.22	2.77	2.34	0.38	0.93
25.0 - 40.0	1.83	1.90	19.91	3.75	19.14	2.04	0.21	0.90

Table A.11: Single differential dijet cross section measured as function of $P_{T,1st}$ with $\eta_{1,2} < 1$.

$P_{T,1st}$ [GeV]	$\frac{d\sigma}{dP_{T,1st}}$ [pb/GeV]	δ_{stat} [%]	δ_{tot} [%]	δ_{HFS} [%]	δ_{mod} [%]	δ_{trig} [%]	δ_{DIS} [%]	C_{had}
$x_\gamma < 0.8$ and $\eta_i < 1, \eta_j > 1$								
15.0 - 25.0	14.05	1.00	10.70	4.46	8.87	2.39	0.48	1.09
25.0 - 40.0	2.66	1.57	12.24	4.77	10.50	2.50	0.51	1.05
$x_\gamma > 0.8$ and $\eta_i < 1, \eta_j > 1$								
15.0 - 25.0	12.73	1.11	4.98	3.25	1.06	2.00	0.08	0.91
25.0 - 40.0	3.03	1.46	17.06	3.91	16.18	2.00	0.04	0.93
40.0 - 60.0	0.23	4.51	10.06	4.56	6.94	2.00	0.27	0.92
$0.0 < x_\gamma < 1.0$ and $\eta_i < 1, \eta_j > 1$								
15.0 - 25.0	26.78	0.74	7.46	3.88	5.16	2.04	0.29	1.01
25.0 - 40.0	5.68	1.07	14.68	4.31	13.53	2.31	0.26	0.99
40.0 - 60.0	0.34	3.72	8.65	4.92	4.97	2.25	0.17	0.96

Table A.12: Single differential dijet cross section measured as function of $P_{T,1st}$ with $\eta_i < 1$ and $\eta_j > 1$.

$P_{T,1st}$ [GeV]	$\frac{d\sigma}{dP_{T,1st}}$ [pb/GeV]	δ_{stat} [%]	δ_{tot} [%]	δ_{HFS} [%]	δ_{mod} [%]	δ_{trig} [%]	δ_{DIS} [%]	C_{had}
$x_\gamma < 0.8$ and $\eta_{1,2} > 1$								
25.0 - 40.0	2.59	1.52	12.25	5.38	10.05	3.18	0.72	1.03
40.0 - 60.0	0.15	5.21	10.22	4.91	5.48	3.16	2.82	1.00
60.0 - 80.0	0.007	23.88	52.23	7.59	14.00	3.06	15.38	0.98
$x_\gamma > 0.8$ and $\eta_{1,2} > 1$								
15.0 - 25.0	3.16	2.11	6.69	3.11	4.33	2.00	0.04	0.96
25.0 - 40.0	1.62	2.07	11.94	3.82	10.57	2.00	0.02	0.94
40.0 - 60.0	0.18	5.47	10.11	4.14	6.57	2.00	0.08	0.96
60.0 - 80.0	0.020	15.64	22.20	6.33	14.00	2.00	0.02	1.01
$0.0 < x_\gamma < 1.0$ and $\eta_{1,2} > 1$								
15.0 - 25.0	8.13	1.21	5.56	3.69	0.77	2.33	0.12	1.04
25.0 - 40.0	4.21	1.23	12.03	4.78	10.25	2.74	0.43	0.99
40.0 - 60.0	0.33	3.80	9.31	4.50	6.06	2.75	1.36	0.98
60.0 - 80.0	0.028	13.13	26.76	6.66	15.29	2.64	4.06	1.00

Table A.13: Single differential dijet cross section measured as function of $P_{T,1st}$ with $\eta_{1,2} > 1$.

$\overline{\mathrm{P}}_{\mathrm{T}}$ [GeV]	$\frac{d\sigma}{d\overline{\mathrm{P}}_{\mathrm{T}}}$ [pb/GeV]	δ_{stat} [%]	δ_{tot} [%]	δ_{HFS} [%]	δ_{mod} [%]	δ_{trig} [%]	δ_{DIS} [%]	$\mathrm{C}_{\mathrm{had}}$
$x_\gamma < 0.8$								
15.0 - 25.0	24.16	0.71	6.86	4.47	3.29	2.79	0.27	1.08
25.0 - 40.0	3.40	1.38	11.14	4.96	9.08	2.68	0.36	1.04
40.0 - 60.0	0.14	6.04	13.97	5.07	10.72	2.42	2.08	1.09
$x_\gamma > 0.8$								
15.0 - 25.0	22.49	0.78	5.83	3.33	3.24	2.00	0.07	0.91
25.0 - 40.0	4.68	1.27	11.27	3.88	9.93	2.00	0.10	0.93
40.0 - 60.0	0.35	4.18	7.78	3.82	4.09	2.00	0.01	0.92
60.0 - 90.0	0.016	16.22	20.58	4.96	11.12	2.00	0.75	1.00
$0.0 < x_\gamma < 1.0$								
15.0 - 25.0	46.65	0.52	5.41	3.92	0.14	2.41	0.18	1.00
25.0 - 40.0	8.08	0.94	11.15	4.34	9.57	2.29	0.09	0.97
40.0 - 60.0	0.49	3.44	8.86	4.18	6.03	2.13	0.60	0.97
60.0 - 90.0	0.020	14.63	17.13	4.43	6.46	2.07	2.40	0.98

Table A.14: Single differential dijet cross section measured as function of $\overline{\mathrm{P}}_{\mathrm{T}}$.

$\overline{\mathrm{P}}_{\mathrm{T}}$ [GeV]	$\frac{d\sigma}{d\overline{\mathrm{P}}_{\mathrm{T}}}$ [pb/GeV]	δ_{stat} [%]	δ_{tot} [%]	δ_{HFS} [%]	δ_{mod} [%]	δ_{trig} [%]	δ_{DIS} [%]	$\mathrm{C}_{\mathrm{had}}$
$x_\gamma > 0.8$ and $\eta_{1,2} < 1$								
15.0 - 25.0	5.00	1.67	9.07	3.32	7.53	2.00	0.11	0.88
25.0 - 40.0	0.98	2.80	11.67	3.41	10.23	2.00	0.22	0.88
40.0 - 60.0	0.021	17.15	20.35	3.17	9.89	2.00	0.02	0.83
$0.0 < x_\gamma < 1.0$ and $\eta_{1,2} < 1$								
15.0 - 25.0	6.66	1.45	8.00	3.47	6.13	2.04	0.43	0.92
25.0 - 40.0	1.19	2.56	10.94	3.47	9.43	2.03	0.42	0.91
40.0 - 60.0	0.023	16.57	20.32	3.94	10.54	2.01	0.02	0.83

Table A.15: Single differential dijet cross section measured as function of $\overline{\mathrm{P}}_{\mathrm{T}}$ with $\eta_{1,2} < 1$.

$\overline{\mathrm{P}}_{\mathrm{T}}$ [GeV]	$\frac{d\sigma}{d\overline{\mathrm{P}}_{\mathrm{T}}}$ [pb/GeV]	δ_{stat} [%]	δ_{tot} [%]	δ_{HFS} [%]	δ_{mod} [%]	δ_{trig} [%]	δ_{DIS} [%]	$\mathrm{C}_{\mathrm{had}}$
$x_\gamma < 0.8$ and $\eta_i < 1, \eta_j > 1$								
15.0 - 25.0	15.85	0.91	8.36	4.49	5.83	2.63	0.50	1.09
25.0 - 40.0	1.53	2.13	9.43	4.97	6.80	2.36	0.30	1.05
40.0 - 60.0	0.049	10.91	26.00	4.36	22.92	2.12	0.63	1.17
$x_\gamma > 0.8$ and $\eta_i < 1, \eta_j > 1$								
15.0 - 25.0	13.86	1.00	4.98	3.32	0.96	2.00	0.07	0.91
25.0 - 40.0	2.33	1.78	12.59	4.17	11.23	2.00	0.10	0.94
40.0 - 60.0	0.19	5.73	7.79	3.62	1.68	2.00	0.09	0.92
60.0 - 90.0	0.008	25.79	33.12	2.73	20.27	2.00	1.30	0.92
$0.0 < x_\gamma < 1.0$ and $\eta_i < 1, \eta_j > 1$								
15.0 - 25.0	29.71	0.67	6.04	3.94	2.66	2.34	0.30	1.01
25.0 - 40.0	3.86	1.36	11.14	4.49	9.47	2.14	0.17	0.98
40.0 - 60.0	0.23	5.07	9.47	3.78	6.14	2.03	0.06	0.96
60.0 - 90.0	0.008	24.81	28.54	3.01	13.26	2.05	1.42	0.93

Table A.16: Single differential dijet cross section measured as function of $\overline{\mathrm{P}}_{\mathrm{T}}$ with $\eta_i < 1$ and $\eta_j > 1$.

$\overline{\mathrm{P}}_{\mathrm{T}}$ [GeV]	$\frac{d\sigma}{d\overline{\mathrm{P}}_{\mathrm{T}}}$ [pb/GeV]	δ_{stat} [%]	δ_{tot} [%]	δ_{HFS} [%]	δ_{mod} [%]	δ_{trig} [%]	δ_{DIS} [%]	$\mathrm{C}_{\mathrm{had}}$
$x_\gamma < 0.8$ and $\eta_{1,2} > 1$								
15.0 - 25.0	6.52	1.23	6.38	4.53	0.69	3.19	0.31	1.07
25.0 - 40.0	1.65	1.90	12.98	5.08	11.01	3.00	1.05	1.02
40.0 - 60.0	0.093	7.29	11.27	5.31	4.84	2.57	2.78	1.05
60.0 - 90.0	0.003	36.02	45.07	1.92	15.91	2.26	21.54	1.08
$x_\gamma > 0.8$ and $\eta_{1,2} > 1$								
15.0 - 25.0	3.61	1.83	7.48	3.36	5.44	2.00	0.02	0.95
25.0 - 40.0	1.37	2.40	9.21	3.72	7.31	2.00	0.03	0.95
40.0 - 60.0	0.14	6.54	12.55	4.14	9.25	2.00	0.09	0.95
60.0 - 90.0	0.009	21.08	22.88	6.22	5.33	2.00	0.35	1.07
$0.0 < x_\gamma < 1.0$ and $\eta_{1,2} > 1$								
15.0 - 25.0	10.13	1.02	6.26	4.12	2.38	2.77	0.19	1.03
25.0 - 40.0	3.02	1.50	11.13	4.46	9.33	2.55	0.56	0.99
40.0 - 60.0	0.23	4.89	10.75	4.61	7.50	2.23	1.16	0.99
60.0 - 90.0	0.012	18.20	19.88	5.19	0.18	2.07	4.97	1.02

Table A.17: Single differential dijet cross section measured as function of $\overline{\mathrm{P}}_{\mathrm{T}}$ with $\eta_{1,2} > 1$.

APPENDIX B

LIST OF USED ACRONYMS

BDC Backward Drift Chamber
BGF Boson-Gluon Fusion
BPC Backward Proportional Chamber
BST Backward Silicon Tracker
CC Charged Current
CDM Color Dipole Model
CERN Conseil Européen pour la Recherche Nucléaire
CIP Central Inner Proportional Chamber
CIZ Central Inner z-Chamber
CJC Central Jet Chamber
COP Central Outer Proportional Chamber
COZ Central Outer z-Chamber
CST Central Silicon Tracker
CTD Central Track Detector
CTL Central Trigger Logic
DESY Deutsches Elektronen-Synchrotron
DGLAP Dokshitzer-Gribov-Lipatov-Altarelli-Parisi
DIS Deep-Inelastic Scattering
DST Data Summary Tape
EPA Equivalent Photon Approximation
ET Electron Tagger
FSR Final State Radiation
FTD Forward Track Detector
FTT Fast Track Trigger
HADROO2 Hadronic Reconstruction in H1OO 2
HAT H1 Analysis Tag
HFS Hadronic Final State
HERA Hadron-Elektron-Ring-Anlage
ISR Initial State Radiation
LAr Liquid Argon
LHC Large Hadron Collider
LO Leading Order

MC Monte Carlo
MODS Micro Object Data Store
NC Neutral Current
NLO Next-to-Leading Order
ODS Object Data Store
PETRA Positron-Elektron-Ring-Anlage
PD Photon Detector
PDF Parton Density Function
PMT Photomultiplier Tube
POT Production Output Tape
QED Quantum Electrodynamics
QCD Quantum Chromodynamics
QCDC QCD Compton
QEDC QED Compton
QPM Quark Parton Model
SM Standard Model
SpaCal "Spaghetti" Calorimeter
SLAC Stanford Linear Accelerator Center
TC Tail Catcher
TE Trigger Element
ToF Time-of-Flight
VDM Vector Meson Dominance Model
WWA Weizsäcker-Williams Approximation

REFERENCES

[A+79] B. Andersson et al., *Parton Fragmentation and String Dynamics*, Z. Phys. **C1**, 105 (1979).

[A+96] R. Appuhn et al., *Hadronic Response and e/π Separation with the H1 Lead / Scintillating Fiber Calorimeter*, Nucl. Instr. and Meth. **A382**, 395 (1996), www.sciencedirect.com/science/article/pii/S0168900296007693.

[A+97a] I. Abt et al., *The H1 Detector at HERA*, Nucl. Instr. and Meth. **A386**, 310–347 (1997), http://www.sciencedirect.com/science/article/pii/S0168900296008935.

[A+97b] I. Abt et al., *The Tracking, Calorimeter and Muon Detectors of the H1 Experiment at HERA*, Nucl. Instr. and Meth. **A386**, 348–396 (1997), http://www.sciencedirect.com/science/article/pii/S0168900296008947.

[AP77] G. Altarelli and G. Parisi, *Asymptotic Freedom in Parton Language*, Nucl. Phys. **B126**, 298 (1977).

[B+69a] E. D. Bloom et al., *High-Energy Inelastic e p Scattering at 6-Degrees and 10-Degrees*, Phys. Rev. Lett. **23**, 930–934 (1969).

[B+69b] M. Breidenbach et al., *Observed Behavior of Highly Inelastic Electron-Proton Scattering*, Phys. Rev. Lett. **23**, 935–939 (1969).

[Bö7] M. O. Bönig, *Messung des D* Meson Produktionsquerschnitts in Tiefinelastischer Streuung mit dem H1 Experiment*, PhD thesis, Universität Dortmund, 2007, www-h1.desy.de/psfiles/theses/h1th-457.pdf.

[Bat99] P. Bate, *High Transverse Momentum 2-jet and 3-jet Cross Section Measurements in Photoproduction*, PhD thesis, The University of Manchester, 1999.

[Ber92] E. L. Berger, *Research Directions for the Decade. Proceedings*, 1990 *Summer Study on High Energy Physics, Snowmass, USA, June 25 - July 13, 1990*, Singapore, Singapore: World Scientific , 808 (1992).

[BGMS75] V. Budnev, I. Ginzburg, G. Meledin and V. Serbo, *The Two Photon Particle Production Mechanism, Physical Problems, Application, Equivalent Photon Approximation*, Phys. Rept. **15**, 181–281 (1975).

[BH34] W. Bethe and W. Heitler, *On the Stopping of Fast Particles and on the Creation of Positive Electrons*, Proceedings of the Royal Society **A146**, 83–112 (1934), rspa.royalsocietypublishing.org/content/146/856/83.

[BHHL78] R. Brun, R. Hagelberg, M. Hansroul and J. Lassalle, *GEANT: Simulation Program for Particle Physics Experiments. User Guide and Reference Manual*, CERN-DD-78-2-REV, CERN-DD-78-2 (1978).

[BJ79] A. Blondel and F. Jacquet, *Proceedings of the Study of an ep Facility for Europe, ed. U. Amaldi*, DESY **391** (1979).

[Bjo69] J. Bjorken, *Asymptotic Sum Rules at Infinite Momentum*, Phys. Rev. **179**, 1547–1553 (1969).

[BOO89] H. Baer, J. Ohnemus and J. Owens, *A Next-To-Leading Logarithm Calculation of Jet Photoproduction*, Phys. Rev. **D40**, 2844 (1989).

[Bou95] A. Bouniatian, *Studies of Hard Scattering in Photoproduction at the ep Storage Ring HERA with the H1 Detector*, PhD thesis, Universität Hamburg, 1995.

[BSYP78] T. Bauer, R. Spital, D. Yennie and F. Pipkin, *The Hadronic Properties of the Photon in High-Energy Interactions*, Rev. Mod. Phys. **50**, 261 (1978).

[Car02] S. Caron, *Jets in Photoprduction at HERA*, PhD thesis, RWTH Aachen, 2002, www-h1.desy.de/psfiles/theses/h1th-294.ps.

[CDSW93] S. Catani, Y. L. Dokshitzer, M. Seymour and B. Webber, *Longitudinally Invariant k_T Clustering Algorithms for Hadron Hadron Collisions*, Nucl. Phys. **B406**, 187–224 (1993).

[CKM+01] G. Corcella, I. Knowles, G. Marchesini, S. Moretti, K. Odagiri et al., *HERWIG 6: An Event Generator for Hadron Emission Reactions with Interfering Gluons Iincluding Supersymmetric Processes*, JHEP **101**, 10 (2001).

[CSS94] K. Charchula, G. Schuler and H. Spiesberger, *Combined QED and QCD Radiative Effects in Deep Inelastic Lepton-Proton Scattering: The Monte Carlo Generator DJANGO6*, Comput. Phys. Commun. **81**, 381–402 (1994).

[DCS04] R. Devenish and A. Cooper-Sarkar, *Deep Inelastic Scattering*, Oxford U., Theor. Phys., 2004.

[Dok72] Y. L. Dokshitzer, *e^+e^- Pair Annihilation and Deep Inelastic ep Scattering in Perturbation Theory*, Sov. J. Nucl. Phys. **15**, 675–684 (1972).

[Dok77] Y. L. Dokshitzer, *Calculation of the Structure Functions for Deep Inelastic Scattering and e^+ e^- Annihilation by Perturbation Theory in Quantum Chromodynamics*, Sov. Phys. JETP **46**, 641–653 (1977).

[Erd97] M. Erdmann, *The Partonic Structure of the Photon*, Springer Tracts Mod. Phys. **138**, 1–114 (1997).

[ES93] S. D. Ellis and D. E. Soper, *Successive Combination Jet Algorithm for Hadron Collisions*, Phys. Rev. **D48**, 3160–3166 (1993), hep-ph/9305266.

[Fey69] R. Feynman, *The Behavior of Hadron Collisions at Extreme Energies*, Conf. Proc. **C690905**, 237–258 (1969).

[Fey72] R. Feynman, *Photon-hadron interactions*, Reading, Frontier in Physics (1972).

[Fey88] R. Feynman, *The Reason for Antiparticles*, The 1986 Dirac Memorial Lectures. Cambridge U. Press (1988).

[Fin06] L. Finke, *Measurement of Charm and Beauty Dijet Cross Sections in Photoproduction*, PhD thesis, Universität Hamburg, 2006.

[FK72] J. I. Friedman and H. W. Kendall, *Deep Inelastic Electron Scattering*, Ann. Rev. Nucl. Part. Sci. **22**, 203–254 (1972), http://wilsona.web.cern.ch/wilsona/Physics/Phys625BjorkenScalingAndParton.

[FMNR93] S. Frixione, M. L. Mangano, P. Nason and G. Ridolfi, *Improving the Weizsacker-Williams Approximation in Electron-Proton Collisions*, Phys. Lett. **B319**, 339–345 (1993), hep-ph/9310350.

[FP92] M. Fontannaz and E. Pilon, *Reexamination of the Photon Structure Function Beyond the Leading Logarithm*, Phys. Rev. **D45**, 382–384 (1992).

[FR97] S. Frixione and G. Ridolfi, *Jet Photoproduction at HERA*, Nucl. Phys. **B507**, 315–333 (1997), hep-ph/9707345.

[GAP83] G. Gustafson, B. Andersson and C. Peterson, *A Semiclassical Model for Quark Jet Fragmentation*, Phys. Rep. **97**, 31 (1983).

[GKS84] F. Gutbrod, G. Kramer and G. Schierholz, *Higher Order QCD Corrections to the Three Jet Cross-Sections: Bare Versus Dressed Jets*, Z. Phys. **C21**, 235 (1984).

[GL72] V. Gribov and L. . Lipatov, *Deep Inelastic e p Scattering in Perturbation Theory*, Sov. J. Nucl. Phys. **15**, 438–450 (1972).

[Gla61] S. L. Glashow, *Partial Symmetries of Weak Interactions*, Nucl. Phys. **22**, 579–588 (1961).

[GMZ61] M. Gell-Mann and F. Zachariasen, *Form-Factors and Vector Mesons*, Phys. Rev. **124**, 953–964 (1961).

[Group08] C. Amsler et al. (Particle Data Group), *Review of Particle Physics*, Phys. Lett. **B667**, 1–1340 (2008).

[GRV92] M. Glueck, E. Reya and A. Vogt, *Photonic Parton Distributions*, Phys. Rev. **D46**, 1973–1979 (1992).

[GS08] C. Grupen and A. Shwartz, *Particle Detectors*, volume 26, Cambridge Monographs on Particle Physics, Nuclear Physics and Cosmology, 2008.

[GTLM10] C. Glasman, J. Terron, D. Lontkovskyi and I. Makarenko, *Dijet Cross Sections in Photoproduction at HERA*, ZEUS-prel-10-014 , 20 (2010).

[H188] V. Blobel (H1), *The BOS System - Dynamic Memory Management*, Internal Report (1988).

[H189] J. Meyer (H1), *Guide for the H1 Simulation Program H1SIM*, Note **11** (1989).

[H191] V. Blobel (H1), *FPACK - a General Standalone Package for Machine Independent Data Input/Output*, Internal Report (1991).

[H192] T. Ahmed et al. (H1), *Hard Scattering in γp Interactions*, Phys. Lett. **B297**, 205–213 (1992).

[H193] B. Andrieu et al. (H1), *Results from Pion Calibration Runs for the H1 Liquid Argon Calorimeter and Comparisons with Simulations*, Nucl. Instr. and Meth. **A336**, 499 (1993).

[H194a] B. Andrieu et al. (H1), *Beam Tests and Calibration of the H1 Liquid Argon Calorimeter with Electrons*, Nucl. Instr. and Meth. **A350**, 57 (1994).

[H194b] H. Kuester (H1), *On the Treatment of Calorimeter Cells and Clusters in H1REC and PHAN Physics Analysis*, Interanl Note **45-03** (1994).

[H195a] S. Aid et al. (H1), *Measurement of the Total γp Cross-Section and its Decomposition at 200-GeV Center-of-Mass Energy*, Z. Phys. **C69**, 27–38 (1995), hep-ex/9509001.

[H195b] S. Levonian and A. Panitch (H1), *Treatment of the Proton Satellite Bunches in 1994 Data*, Internal Note **454** (1995).

[H196] S. Aid et al. (H1), *Jets and Energy Flow in Photon-Proton Collisions at HERA*, Z. Phys. **C70**, 17–30 (1996), hep-ex/9511012.

[H197] J. K. Koehne et al. (H1), *Realization of a Second Level Neural Network Trigger for the H1 Experiment at HERA*, Nucl. Instrum. Meth. **A 389**, 128–133 (1997).

[H198a] C. Adloff et al. (H1), *Measurement of the Inclusive Dijet Cross Section in Photoproduction and Determination of an Effective Parton Distribution in the Photon*, Eur. Phys. J. **C1**, 97–107 (1998), hep-ex/9709004.

[H198b] C. Beigbeder et al. (H1), *Level 2 Topological Trigger (L2TT) Hardware*, Internal Note **547** (1998).

[H199a] M. Jacquet et al. (H1), *Absolute Hadronic Jet Calibration of the H1 Liquid Argon Calorimeter*, Internal Note **571** (1999).

[H199b] S. Lueders (H1), *CST/CIP_{2000} Stand-Alone Tracking and Vertexing*, Internal Note **570** (1999).

[H100] L. West (H1), *How to use the Heavy Flavour Working Group Track, Muon and Electron Selection Code H1PHAN Version $\geq$ 3.00/00*, (2000).

[H101] A. Baird et al. (H1), *A Fast Track Trigger for the H1 Collaboration*, Nucl. Instrum. Meth. **A461**, 461–464 (2001).

[H102] C. Veelken (H1), *H1NonepBgFinder - Rejection of Cosmic Muon and Beam-halo Events in the H1OO Framework*, Internal Note **603** (2002).

[H105] M. Peez et al. (H1), *An Energy Flow Algorithm for Hadronic Reconstruction in OO: Hadroo2*, Internal Note **616** (2005).

[H106] A. Aktas et al. (H1), *Photoproduction of Dijets with High Transverse Momenta at HERA*, Phys. Lett. **B639**, 21–31 (2006), hep-ex/0603014.

[H107a] H1OO (H1), *The H1OO Physics Analysis Project*, Internal Report (last update 2007).

[H107b] J. Katzy (H1), *H1OO - an Analysis Framework for H1*, Internal Report (2007).

[H108] H1Rec (H1), *H1REC docu page*, Internal Report (last update 2008).

[H109] H1OO (H1), *H1HatEvent*, Internal Report (last update 2009).

[H111] R. Kogler (H1), *Jets at High Q^2*, Internal Report , 1–45 (2011).

[H112] F. Aaron et al. (H1), *Determination of the Integrated Luminosity at HERA using Elastic QED Compton Events*, Eur. Phys. J. **C72**, 2163 (2012), hep-ex/1205.2448.

[H113] H1OO (H1), *Class Index*, (last update 2013).

[Hig64] P. W. Higgs, *Broken Symmetry and the Mass of Gauge Vector Meson*, Phys. Rev. Lett. **13**, 508–509 (1964).

[HZ10] F. Aaron et al. (H1 and ZEUS), *Combined Measurement and QCD Analysis of the Inclusive $e^{\pm}p$ Scattering Cross Sections at HERA*, JHEP **1001**, 109 (2010), hep-ex/0911.0884.

[Jun95] H. Jung, *Hard Diffractive Scattering in High Energy ep Collisions and the Monte Carlo Generator RAPGAP*, Comput. Phys. Commun. **86**, 147–161 (1995).

[KK97] M. Klasen and G. Kramer, *Inclusive Two Jet Production at HERA: Direct and Resolved Cross-Sections in Next-to-Leading Order QCD*, Z. Phys. **C76**, 67–74 (1997), hep-ph/9611450.

[KKK98] M. Klasen, T. Kleinwort and G. Kramer, *Inclusive Jet Production in γp and $\gamma\gamma$ Processes: Direct and Resolved Photon Cross-Sections in Next-to-Leading Order QCD*, Eur. Phys. J. direct **C1**, 1 (1998), hep-ph/9712256.

[Kog10] R. Kogler, *Measurement of Jet Production in Deep-Inelastic ep Scattering at HERA*, PhD thesis, Universität Hamburg, 2010, www-h1.desy.de/psfiles/theses/h1th-590.pdf.

[Loe92] L. Loennblad, *Ariadne version 4: A Program for Simulation of QDC Cascades Implementing the Colour Dipole Model*, Comput. Phys. Commun. **71**, 15–31 (1992).

[MM08] L. Marti Magro, *Multiple Parton Interactions in Photoproduction at HERA/H1*, PhD thesis, Universität Hamburg, 2008.

[N+96] T. Nicholls et al., *Performance of an Electromagnetic Lead / Scintillating Fiber Calorimeter for the H1 Detector*, Nucl. Instr. and Meth. **A374**, 149 (1996).

[Nik07] A. Nikiforov, *Measurement of the Neutral Current $e^{\pm}p$ Cross Sections Using Longitudinally Polarised Lepton Beams at HERA II*, PhD thesis, Ludwig-Maximilians-Universität München, 2007, www-h1.desy.de/psfiles/theses/h1th-469.pdf.

[PSH+02] J. Pumplin, D. Stump, J. Huston, H. Lai et al., *New Generation of Parton Distributions with Uncertainties from Global QCD Analysis*, JHEP **207**, 12 (2002), hep-ph/0201195.

[Rau02] J. Rauschenberger, *Prozesse des geladenen Stromes in Tiefunelastischer Positron-Proton Streuung bei HERA*, PhD thesis, Universität Hamburg, 2002.

[Roo13] RooT, *Class Index*, Internal Report (last update 2013).

[S+03] D. Stump et al., *Inclusive Jet Production, Parton Distributions, and the Search for New Physics*, JHEP **310**, 46 (2003), hep-ph/0303013.

[Sak60] J. Sakurai, *Theory of Strong Interactions*, Annals Phys. **11**, 1–48 (1960).

[Sal68] A. Salam, *Weak and Electromagnetic Interactions*, Conf. Proc. **C680519**, 367–377 (1968).

[Sey95] M. Seymour, *Presented at 10^{th} Topological Workshop on Proton-Antiproton Collider Physics*, Batavia, IL (1995).

[Shu11] S. Shushkevich, *Measurement of the Neutral Current Reaction at high Q^2 in the H1 Experiment at HERA II*, PhD thesis, Ludwig-Maximilians Universität München, 2011.

[Sjo94] T. Sjoestrand, *High−Energy Physics Event Generation with PYTHIA 5.7 and JET−SET 7.4*, Comput. Phys. Commun. **82**, 74 (1994).

[SMS06] T. Sjoestrand, S. Mrenna and P. Z. Skands, *PYTHIA 6.4 Physics and Manual*, JHEP **0605**, 026 (2006), hep-ph/0603175.

[SS95] G. A. Schuler and T. Sjoestrand, *Low and High Mass Components of the Photon Distribution Functions*, Z. Phys. **C68**, 607–624 (1995), hep-ph/9503384.

[SS96] G. A. Schuler and T. Sjoestrand, *Parton Distributions of the Virtual Photon*, Phys. Lett. **B376**, 193–200 (1996), hep-ph/9601282.

[Str04] I. Strauch, *Jets with high Transverse Momenta in Photoprduction at HERA*, PhD thesis, Universität Hamburg, 2004, www-h1.desy.de/psfiles/theses/h1th-369.ps.

[Ter] J. Terron, gratefully acknowledge obtaining a version of the Klasen and Kramer program for the NLO predictions shown here.

[vW34] C. von Weizsaecker, *Radiation Emitted in Collisions of Very Fast Electrons*, Z. Phys. **88**, 612–625 (1934).

[W+81] B. H. Wiik et al., *HERA, A Proposal for a Large Electron Proton Colliding Beam Facility at DESY*, DESY-HERA **81/10** (1981).

[Wei67] S. Weinberg, *A Model of Leptons*, Phys. Rev. Lett. **19**, 1264–1266 (1967).

[Wil35] E. Williams, Kgl. Danske Vidensk. Selskab. Mat.-Fiz. Medd. **N4**, 13 (1935).

[Wit77] E. Witten, *Anomalous Cross Section for Photon-Photon Scattering in Gauge Theories*, Nucl. Phys. **B120**, 189–202 (1977).

Acknowledgements

This thesis would not have been possible without the valuable contribution and help of many people.
First of all I would like to thank my supervisor Dr. Guenter Grindhammer. His in-depth physics knowledge, interest, support, guidance and suggestions were crucial in carrying out this analysis.
I would also like to thank my colleagues, Daniel, Stas, Julia, Nastja, Armen, Kenan, Timon and many others for fruitful discussions on physics, cosmology, philosophy and other countless interesting topics. Thanks to Roman for the help with my analysis, in particular, proving that our independent programs give the same results. My gratitude goes to Prof. Juan Terron for providing me with the NLO code.
I would like to thank the participants of the HaQ group and all H1 members for interesting questions, which pointed to many issues of this analysis and pushed this research further on.
I owe sincere and earnest thankfulness to the members of the Max-Planck-Institut for Physics in Munich for support and possibility to make this research.
Xeniya, Olena, Rinat, Felix, I am so happy I have you all as my friends. Thank you that you are always there for me.
A very special thank goes to my family in Kazakhstan for all their love, encouragement, support and understanding.
Zum Schluß würde ich gerne meinem Schatz für die Liebe und den dauerhaften Glauben an mich danken. Deine Unterstützung, dein Optimismus und deine Begeisterung haben mir geholfen die Schwierigkeiten zu überwinden und meine Ziele zu erreichen.